Department of
Mechanical
Engineering

An innovative approach to tibiofemoral joint modelling

By Giuliano Lamberto

Supervisor: Dr Claudia Mazzà
Co-Supervisor: Dr Saulo Martelli (Flinders University, South Australia)

DDP supervisor: Dr Xinshan Li

May 2017

A thesis submitted in partial fulfilment of the requirements for the degree of Doctor of Philosophy

Abstract

Musculoskeletal models allow non-invasive predictions of non-directly measurable forces exchanged within the human body in motion. Despite this information has plenty of potential applications, actual adoption of current models is impeded by limitations related to the insufficient number of validation studies or the drastic modelling assumptions often made. This thesis aims to address these limitations developing an innovative approach to the mechanical modelling of the tibiofemoral joint. To achieve this, three main sections are presented:

Effects of the soft tissue artefact on current musculoskeletal models – this study used a statistical approach to develop a realistic distribution of soft tissue artefact, which was used to assess the sensitivity of the estimates of three publicly-available musculoskeletal models. Results showed joint-dependent variations, decreasing from hip to ankle, providing awareness for the research community on the investigated models and indications to better interpret simulation outcomes.

Modelling the mechanical behaviour of the tibiofemoral joint using compliance matrices – this part of the thesis proposed a method to characterise the tibiofemoral joint mechanical behaviour using a discrete set of compliance matrices. Model calibration and validation was performed using data from *ex vivo* testing. Accurate results were found in close proximity to where the model was calibrated, opening the way to a more biofidelic joint representations. The developed model was included in the calculation pipeline to estimate joint kinematics using penalty-based method. For this inclusion, validation using *in vivo* data for these estimates was promising, providing remarkable alternatives to traditional methods.

A force-based approach to personalised tibiofemoral models – this section attested on an *ex vivo* dataset that the model based on compliance matrices can be personalised using data from clinical tests. Since the latter are usually performed *in vivo*, this opens the way to future exciting applications.

Acknowledgments

I would like to express my gratitude and my esteem to my supervisors Dr. Claudia Mazzà and Dr. Saulo Martelli for their guidance during this great academic experience. I would like to acknowledge them for encouraging my research by helping me through it with guidelines and for letting me grow as a researcher. I appreciated all the contributions and ideas brought on the projects. I am grateful also to Professor Aurelio Cappozzo for the excellent example he provided as a successful field leader. His maximal attention to details in every aspect of the research was inspiring.

A great thanks goes to the INSIGNEO team that supported me every day. We laughed and worked hard together; I will never forget this experience. A special thanks to Eugene and Freddie for their help in proof reading.

An essential thank you also goes to my family and friends for their support.

The greatest acknowledgement goes to Fede who supported me since the first day. Thanks for being there for me all the times.

For the work of Chapter 4, the author wish to thank Li-De Chang, Tchung Whao, Mei-Ying Kuo, Elena Bergamini, and Valerio Rossi for providing technical and logistical support during and after the experimental tests described in the chapter.

For the work of Chapter 5, the author is grateful for the help received during the experimental acquisitions to the Orthopaedic testing laboratory at Flinders University. Special thanks go to Dhara Amin, Bogdan Solomon, Boyin Ding, Richard Stanley, John Costi and Karen Reynolds. An acknowledge goes to the Flinders team in general, which contributed to make my Australian journey easier and unforgettable. The author wishes to thank the following students of the University of Sheffield for their help: Nuruljannah B Mohd Shaffie, David Agban and Scott Robinson. Final acknowledgment goes to Genliang Chen (Department of Robotics, Shanghai Jiao Tong University, China) for providing assistance and adapted MATLAB codes for the Principal Axes Decomposition method.

Publications and conference abstracts of this thesis

Full papers in scientific journals:

Lamberto, G., Martelli, S., Cappozzo, A., Mazzà, C., (2016). "To what extent is joint and muscle mechanics predicted by MSMs sensitive to soft tissue artefacts?" *J. Biomech.* , 1–9. doi:10.1016/j.jbiomech.2016.07.042.

Lamberto, G., Richard, V., Dumas, R., Valentini, P.P., Pennestrì, E., Lu, T.-W., Camomilla, V., Cappozzo, A., (2016). "Modeling the Human Tibiofemoral Joint Using *Ex Vivo* Determined Compliance Matrices.", *J. Biomech. Eng*. 138, 61010. doi:10.1115/1.4033480.

Richard, V., Lamberto, G., Lu, T.-W., Cappozzo, A., Dumas, R., (2016). "Knee Kinematics Estimation Using Multi-Body Optimisation Embedding a Knee Joint Stiffness Matrix: A Feasibility Study." *PLoS One*, 11, e0157010. doi:10.1371/journal.pone.0157010

Conference abstracts:

Lamberto, G, Martelli, S, Amin, D, Solomon, B, Reynolds, K and Mazzà, C. "Development of a personalised linear elastic model of the knee joint from *ex vivo* six degrees of freedom stiffness measurements", *accepted as oral presentation for* the XXVI Congress of the International Society of Biomechanics, Brisbane, AUS, July 2017

Lamberto, G, Martelli, S, Cappozzo, A, Mazzà, C. "A probabilistic analysis of the effects of soft tissue artefacts on the estimate of muscle and joint forces", 22nd conference of the European Society of Biomechanics (ESB), Lyon, France, July 2016. *Oral presentation.*

Lamberto, G, Martelli, S, Cappozzo, A, Mazzà, C, "Musculoskeletal model sensitivity to stereophotogrammetry skin artefacts", 21st conference of the Australian

& New Zealand Orthopaedic Research Society (ANZORS), Auckland, NZ, October 2015. *Poster presentation.*

Richard, V, Lamberto, G, Lu, TW, Camomilla, V, Cappozzo, A, Dumas, R. "Multi-body optimisation with knee joint constraints based on the stiffness matrix", XXV Congress of the International Society of Biomechanics, Glasgow, UK, July 2015. *Oral presentation.*

Nomenclature

MSM: Musculoskeletal model

MBO: Multibody kinematics optimisation

STA: Soft tissue artefact

DoF: Degree of freedom

MRI: Magnetic resonance imaging

sEMG: Surface electromyography

GRFs: Ground reaction forces

BW: Body weight

Table of Contents

CHAPTER 1

Introduction

1.1. Background

Musculoskeletal models (MSMs) and simulations have become increasingly effective tools to gain insight into human movement, with the ability to predict forces that cannot be directly measured, such as muscle forces and forces transmitted inside a joint (e.g. bone to bone contact). This powerful capability has the potential to tackle musculoskeletal disorders (e.g. ligament injury or osteoarthritis) in an objective way, by allowing quantitative monitoring of disease progression and providing indications to select the best treatment for a disorder.

Since the earliest contributions nearly five decades ago (Morrison, 1970; Panjabi, 1973; Seireg and Arvikar, 1973), the number of studies modelling the musculoskeletal system has risen rapidly in conjunction with increased computational power, reaching over 2000 papers in 2013 (Hicks et al., 2015). Despite this clear growth, applying MSMs and simulations consistently in clinical practice remains a complex challenge, which requires many different variables and uncertainties to be taken into account. So far, this challenge has not yet been addressed, mainly due to the insufficient number of available sensitivity and validation studies, but also as a limitation resulting from the drastic modelling assumptions and simplifications that sometimes have to be made. Appropriate verification and validation techniques need to be implemented to increase the trust from non-modellers and foster their understanding of the utility of the simulation results, in order to facilitate translation into clinical applications.

Among the possible clinical fields, orthopaedics could certainly benefit from the introduction of MSMs into practice. Within this field, non-invasive estimates of muscle and joint forces during motion might be used as a quantitative indicator of a patient's health condition in relation to various pathologies of the musculoskeletal

system. This information could be extremely useful for clinicians and orthopaedic surgeons, especially when the diagnosis or monitoring from more traditional methods (i.e. physical examination and imaging techniques) are insufficient. An example of this is in treatment of the rupture of the anterior cruciate ligament (ACL) in the tibiofemoral joint. The ACL rupture, totalling 150,000 US cases per annum on average (Gage et al., 2012), requires a reconstruction surgery to restore an active lifestyle for most patients. Despite different surgical alternatives and techniques exist (Kaseta et al., 2008), the typical process for this surgery involves the re-establishment of the mechanical knee function using an autologous tendon graft (i.e. a portion of a tendon from the same patient), which is fixed to the bone using screws. The implanted portion of tendon undergoes a series of biological events named "ligamentization", which remodel it into a ligament-like structure (Claes et al., 2011). The most-common timeframe to return to high impact activities such as sports after surgery is six months, although accelerated recovery are possible when no other knee lesions (e.g. collateral ligament damages or meniscal tears) occur (Roi et al., 2006). Short and long-term complications ACL-reconstruction related typically lead to higher costs for the healthcare system. For instance, the long-term development of osteoarthritis related to ACL reconstructions has been estimated to an annual cost of $2.78 billion in the US only (Mather et al., 2013). Nowadays, however, the choice of the preferred surgical approach to repair ACL ruptures still relies on a surgeon's subjective evaluation, and the question of which is the best surgical procedure is still debated.

In this scenario, MSMs can represent a non-invasive alternative to reduce ACL surgery failures and associated costs by objectively determining the best strategy for the reconstructive intervention, before its occurrence. Indeed, ACL failure requiring revision, occurring in 10-15% of operated patients (Samitier et al., 2015), was found to be due mostly to malpositioning of the new ligament in a study conducted over 12 years (Trojani et al., 2011).

For example, a surgeon could simulate different interventions to evaluate how much these would affect the loading of the joint. Additionally, the estimates of muscle forces could help determine whether a patient requires strengthening a set of muscles

to further stabilise the joint after the intervention (i.e. indications for a specific rehabilitation protocol).

The accuracy of muscle and joint force predictions relies on the MSMs' ability to exactly simulate skeletal motion of the human body, i.e. the so-called body segment kinematics, by quantifying the instantaneous pose of each bone in the 3D space and the relative movement between adjacent segments. Within this framework, each articulation of interest in the body is modelled with a corresponding mechanical equivalent (e.g. the tibiofemoral joint is often represented as a hinge joint, allowing a single rotation between tibia and femur). Accurate and non-invasive *in vivo* tracking of the bone poses is extremely difficult. Skin surface measurement data is usually obtained from stereophotogrammetric systems, which record the 3D position in space of markers attached to a subject's body. A major issue related to driving models with this technique is that the skin moves with respect to the underlying bone, producing an error called soft tissue artefact (STA) (Leardini et al., 2005). By its nature, this error cannot be attenuated or eliminated by means of simple filtering techniques and this prevents accurate non-invasive tracking of the skeletal movement necessary for the model input. To deal with this input inaccuracy, multibody optimisation (MBO) methods (Lu and O'Connor, 1999) have been introduced, aiming to minimise the difference between experimental surface data and bone model information.

However, two aspects still need to be fully addressed in relation to MBO when used as part of a musculoskeletal modelling process. First, MBO has been introduced aiming to limit the joint dislocation in model kinematics and to reduce the STA effects. It is not clear, however, to what extent this artefact reduction happens in different MSMs or how the residual STA affects the estimates of muscle and joint forces. Second, MBO traditionally implies an underlying mechanical joint model for each articulation of the human body. As a result, most of these joint models represent the reality in a very simplified way (Cereatti et al., 2006; Lenhart et al., 2015; Xu et al., 2014). This is evident for the tibiofemoral joint and its complex function aiming at simultaneously ensuring stability and motion. In fact, inappropriate mechanical equivalents that neglect the six degrees of freedom motion of the tibiofemoral joint are frequently used. Furthermore, the implicit assumptions

of these models (such as a single rotational degree of freedom) often limit their clinical usability, meaning that complex pathological motions (e.g. ACL-injured knee) cannot be identified or simulated by the models (Martelli et al., 2015; Mishra et al., 2011; Shelburne and Pandy, 1997).

Another important feature in the definition of MSMs is their amount of personalisation (i.e. the ability to better represent a particular subject/patient), which is typically introduced to improve their precision (Prinold et al., 2016; Scheys et al., 2011) and their accuracy (Gerus et al., 2013) when used within clinical applications. When building these models, hard and soft tissue geometries can be either obtained from an anatomic atlas or extracted from medical images, with generic material properties often coming from public datasets (Arnold et al., 2000; Klein Horsman et al., 2007). As a result, the biofidelity of the model increases and the physical quantities of interest are better estimated (Arnold et al., 2000, 2010; Scheys et al., 2011). Nevertheless, the focus of the personalization is usually on the geometry of such models and not on individual material properties (Prinold et al., 2016). Also, building image-based subject-specific MSMs is a time-consuming and costly process when compared with simply scaling generic MSMs to patient's anthropometry (Martelli et al., 2014). An intriguing alternative to model personalisation based on medical imaging is the possibility to use force data combined with the relative motion of the joints to calibrate a personalised MSM. This data can be recorded during the *in vivo* execution of some clinical tests, which are normally performed in orthopaedics to assess the joint function.

1.2. Aims and objectives

The aim of this thesis is to develop an innovative approach to the mechanical modelling of the tibiofemoral joint and of its surrounding tissues. This model will fill a gap in biomechanical knowledge and may be incorporated within surgery procedures to drive interventions, predicting the effects of different procedures for an effective clinical pre-operative evaluation. The model is meant to be used as part of a whole-body MSM, driven by stereophotogrammetry. It will be suitable for use in dynamic simulations in clinical applications, with the potential ability to be personalised using *in vivo* experiments performed on a specific patient.

The development of a model of such kind includes a number of steps aiming to first maximise its reliability and accuracy (including a sensitivity analysis, validation using *ex vivo* and *in vivo* input datasets) and then to achieve patient personalisation. This will be accomplished by pursuing four main objectives, associated to the fundamental modelling workflow:

1. determining the effects of the experimental errors associated with the use of stereophotogrammetric data to drive the most commonly-used MSMs in the literature under *in vivo* conditions;
2. investigating the *ex vivo* behaviour of the human tibiofemoral joint both for calibration and validation of the model;
3. embedding the joint model in the MSM pipeline for estimating relevant kinematics, and validating results using *in vivo* input data from two patients;
4. defining and evaluating ad hoc model personalisation features.

This thesis is organised in six chapters, which describe the research done to accomplish these objectives.

Chapter 2 includes a brief overview of the knee structures and the injury of interest (ACL rupture), with the clinical tests and the reconstruction techniques associated to it. In addition, the chapter will provide a description and definition of the MSMs, including the inputs, the outputs, and the mathematical formulation. Finally, the state of the art concerning the STA and the MBO will be presented.

Chapter 3 includes the quantification of the effects of STA to the estimates of three publicly available and widely adopted MSMs. A statistical approach has been selected to build a realistic distribution (i.e. compared with multiple independent studies) of a location-dependent STA and assess its impact on kinematic and dynamic model predictions.

Chapter 4 presents the development of the tibiofemoral joint model using data from robotic mechanical testing of cadaveric joints. In particular, a new methodology to be used for a model calibration and validation will be described. The second part of this chapter will show how to embed the relevant model results into an alternative multibody optimisation pipeline to allow for the estimate of joint kinematics, starting from stereophotogrammetric skin data. The performance of this

alternative approach will be compared against more traditional methods as well as with a gold standard.

Chapter 5 presents a method for the personalisation of the force-displacement coupling of such models using newly-acquired *ex vivo* data and easily detectable measures combined with the execution of standard clinical tests. The latter are usually performed *in vivo* in orthopaedics to assess the stability and the mechanical function of a joint, and will be used as a proof of concept of the potential to transfer this idea to an *in vivo* scenario.

Chapter 6 concludes the thesis, summarising the achieved aims, stating the open challenges and offering some ideas for further studies.

References

Arnold, a S., Salinas, S., Asakawa, D.J., Delp, S.L., 2000. Accuracy of muscle moment arms estimated from MRI-based musculoskeletal models of the lower extremity. Comput. Aided Surg. 5, 108–19. doi:10.1002/1097-0150(2000)5:2<108::AID-IGS5>3.0.CO;2-2

Arnold, E.M., Ward, S.R., Lieber, R.L., Delp, S.L., 2010. A model of the lower limb for analysis of human movement. Ann. Biomed. Eng. 38, 269–79. doi:10.1007/s10439-009-9852-5

Cereatti, A., Della Croce, U., Cappozzo, A., 2006. Reconstruction of skeletal movement using skin markers: comparative assessment of bone pose estimators. J. Neuroeng. Rehabil. 3, 7. doi:10.1186/1743-0003-3-7

Claes, S., Verdonk, P., Forsyth, R., Bellemans, J., 2011. The "Ligamentization" Process in Anterior Cruciate Ligament Reconstruction. Am. J. Sports Med. 39, 2476–2483. doi:10.1177/0363546511402662

Gage, B.E., McIlvain, N.M., Collins, C.L., Fields, S.K., Comstock, R.D., 2012. Epidemiology of 6.6 million knee injuries presenting to United States emergency departments from 1999 through 2008. Acad. Emerg. Med. 19, 378–85. doi:10.1111/j.1553-2712.2012.01315.x

Gerus, P., Sartori, M., Besier, T.F., Fregly, B.J., Delp, S.L., Banks, S. a, Pandy, M.G., D'Lima, D.D., Lloyd, D.G., 2013. Subject-specific knee joint geometry improves predictions of medial tibiofemoral contact forces. J. Biomech. 46, 2778–86. doi:10.1016/j.jbiomech.2013.09.005

Hicks, J.L., Uchida, T.K., Seth, A., Rajagopal, A., Delp, S., 2015. Is my model good enough? Best practices for verification and validation of musculoskeletal models and simulations of human movement. J. Biomech. Eng. 137. doi:10.1115/1.4029304

Kaseta, M.K., DeFrate, L.E., Charnock, B.L., Sullivan, R.T., Garrett, W.E., 2008. Reconstruction technique affects femoral tunnel placement in ACL reconstruction. Clin. Orthop. Relat. Res. 466, 1467–1474. doi:10.1007/s11999-008-0238-z

Klein Horsman, M.D., Koopman, H.F.J.M., van der Helm, F.C.T., Prosé, L.P., Veeger, H.E.J., 2007. Morphological muscle and joint parameters for musculoskeletal modelling of the lower extremity. Clin. Biomech. (Bristol, Avon) 22, 239–47. doi:10.1016/j.clinbiomech.2006.10.003

Leardini, A., Chiari, L., Della Croce, U., Cappozzo, A., 2005. Human movement analysis using stereophotogrammetry. Part 3. Soft tissue artifact assessment and compensation. Gait Posture 21, 212–25. doi:10.1016/j.gaitpost.2004.05.002

Lenhart, R.L., Kaiser, J., Smith, C.R., Thelen, D.G., 2015. Prediction and Validation of Load-Dependent Behavior of the Tibiofemoral and Patellofemoral Joints During Movement. Ann. Biomed. Eng. doi:10.1007/s10439-015-1326-3

Lu, T.-W., O'Connor, J.J., 1999. Bone position estimation from skin marker co-ordinates using global optimisation with joint constraints. J. Biomech. 32, 129–

134. doi:10.1016/S0021-9290(98)00158-4

Martelli, S., Calvetti, D., Somersalo, E., Viceconti, M., 2015. Stochastic modelling of muscle recruitment during activity. Interface Focus 5, 20140094–20140094. doi:10.1098/rsfs.2014.0094

Martelli, S., Kersh, M.E., Pandy, M., 2014. Sensitivity of femoral strain calculations to anatomical scaling errors in musculoskeletal models of movement. J. Biomech. 48, 3606–3615. doi:10.1016/j.jbiomech.2015.08.001

Mather, R.C. 3rd, Koenig, L., Kocher, M.S., Dall, T.M., Gallo, P., Scott, D.J., Bach, B.R.J., Spindler, K.P., 2013. Societal and economic impact of anterior cruciate ligament tears. J. Bone Joint Surg. Am. 95, 1751–1759. doi:10.2106/JBJS.L.01705

Mishra, M., Derakhshani, R., Paiva, G.C., Guess, T.M., 2011. Nonlinear surrogate modeling of tibio-femoral joint interactions. Biomed. Signal Process. Control 6, 164–174. doi:10.1016/j.bspc.2010.08.005

Moissenet, F., Chèze, L., Dumas, R., 2014. A 3D lower limb musculoskeletal model for simultaneous estimation of musculo-tendon, joint contact, ligament and bone forces during gait. J. Biomech. 47, 50–8. doi:10.1016/j.jbiomech.2013.10.015

Morrison, J.B., 1970. The mechanics of the knee joint in relation to normal walking. J. Biomech. 3, 51–61.

Panjabi, M., 1973. Three-dimensional mathematical model of the human spine structure. J. Biomech. 6.

Prinold, J. a. I., Mazzà, C., Di Marco, R., Hannah, I., Malattia, C., Magni-Manzoni, S., Petrarca, M., Ronchetti, A.B., Tanturri de Horatio, L., van Dijkhuizen, E.H.P., Wesarg, S., Viceconti, M., 2016. A Patient-Specific Foot Model for the Estimate of Ankle Joint Forces in Patients with Juvenile Idiopathic Arthritis. Ann. Biomed. Eng. 44, 247–257. doi:10.1007/s10439-015-1451-z

Roi, G.S., Nanni, G., Tencone, F., 2006. Time to return to professional soccer matches after ACL reconstruction. Sport Sci. Health 1, 142–145. doi:10.1007/s11332-006-0025-8

Samitier, G., Marcano, A.I., Alentorn-Geli, E., Cugat, R., Farmer, K.W., Moser, M.W., 2015. Failure of Anterior Cruciate Ligament Reconstruction. Arch Bone Jt Surg. 3, 220–240. doi:10.1016/j.csm.2012.08.015

Scheys, L., Desloovere, K., Spaepen, A., Suetens, P., Jonkers, I., 2011. Calculating gait kinematics using MR-based kinematic models. Gait Posture 33, 158–64. doi:10.1016/j.gaitpost.2010.11.003

Seireg, A., Arvikar, R.J., 1973. A mathematical model for evaluation of forces in lower extremeties of the musculo-skeletal system. J. Biomech. 6. doi:10.1016/0021-9290(73)90053-5

Shelburne, K.B., Pandy, M.G., 1997. A musculoskeletal model of the knee for evaluating ligament forces during isometric contractions. J. Biomech. 30, 163–76.

Trojani, C., Sbihi, A., Djian, P., Potel, J.F., Hulet, C., Jouve, F., Bussi??re, C.,

Ehkirch, F.P., Burdin, G., Dubrana, F., Beaufils, P., Franceschi, J.P., Chassaing, V., Colombet, P., Neyret, P., 2011. Causes for failure of ACL reconstruction and influence of meniscectomies after revision. Knee Surgery, Sport. Traumatol. Arthrosc. 19, 196–201. doi:10.1007/s00167-010-1201-6

Xu, H., Bloswick, D., Merryweather, A., 2014. An improved OpenSim gait model with multiple degrees of freedom knee joint and knee ligaments. Comput. Methods Biomech. Biomed. Engin. 18, 1217–1224. doi:10.1080/10255842.2014.889689

CHAPTER 2

Modelling the tibiofemoral joint: anatomical, computational and experimental aspects

This chapter aims at providing the background knowledge needed to understand different elements that will be dealt with in this thesis. Basic definitions and general overviews are combined with more specific and detailed information, which relates to the fundamental aspects of the research.

2.1. Anatomical planes, directions and axes

When describing the structure and motion of the knee joint, a standardised medical terminology is used. The same terminology, in general, is also used to describe the anatomy of the human body (Whittle, 2007). Considering the human body standing upright with the face and palms facing forward, three anatomical orthogonal planes can be identified: the frontal (or coronal) plane, the sagittal plane and the transverse (or horizontal) plane (Figure 2.1). The frontal plane divides the body vertically into anterior and posterior parts. The sagittal plane is a vertical symmetry plane, which divides the body into left and right sides. The transverse plane is horizontal and splits the body into superior and inferior parts. The intersection of these planes generates three directions: the medio-lateral axis, the longitudinal axis and the anterior-posterior axis (Figure 2.1). When referring to a single segment or bone of the human body, medial means closer to the longitudinal axis and lateral means away from the same axis. In addition, the terms “proximal” and “distal” are used. Proximal means near the main mass of the body (the trunk), whereas distal points away from it (Hyman and Wake, 1992). These terms are usually adopted for the long

bones of the body (e.g. the tibiofemoral joint connects the proximal tibia with the distal femur).

A dedicated terminology is also used to describe specific rotational movements of adjacent body segments. Flexion and extension rotations are those occurring in the sagittal plane. Flexion is the movement that brings the two segments closer to each other, extension represents the opposite one. Internal and external rotations are motions in the transverse plane, around the longitudinal axis of each segment. Moving a limb inward to the body centre is called internal and the opposite motion characterises the external rotation. Abduction and adduction rotations take place in the frontal plane. Moving away or closer to the longitudinal axis represents abduction and adduction, respectively.

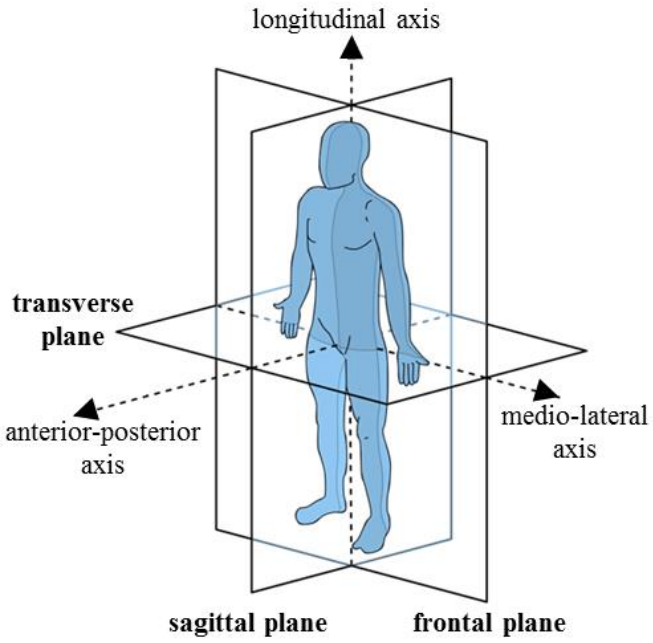

Figure 2.1 – Anatomical planes and axes of the human body. Adapted from https://commons.wikimedia.org/wiki/File:Anatomical_Planes.svg.

2.2. Functional anatomy of the knee joint

When looking at the skeletal system with a focus on the lower limb, the main regions of pelvis, thighs, the shanks and the feet can be identified. These regions are connected together through the hip joint, the knee joint and the ankle joint, respectively. The main feature of each of these joints is the ability to support high compressive loads while simultaneously allowing motion. A joint able to provide these features is called diarthroses or synovial joint (Stevens, 2006) and it is composed by the synovial membrane, the joint cavity containing the synovial fluid, and the articular cartilage on the bone surfaces. The articular capsule of fibrous connective tissue attaches onto the bones and creates an isolated chamber, hosting the synovial membrane. This membrane secretes the synovial fluid, needed not only to lubricate the internal structure during motion, but also to provide nutrition to the articular cartilage not perfused by blood vessels. The articular cartilage, a thin hyaline cartilage layer, acts as a protector of the bones, enabling a smooth relative movement and the prevention of surface bone damage (Mader, 2004).

The knee joint is the largest synovial joint of the human body, articulating four bones: the femur, the tibia, the patella and the fibula. This joint includes the tibiofemoral joint, the tibiofibular joint and the patellofemoral joint (Figure 2.2). When considering stability and likelihood of knee injuries (Gage et al., 2012), the tibiofemoral joint plays a major role with respect to other two joints. For this reason, despite the tibiofibular and patellofemoral joints being important to stabilise the joint and transferring the quadriceps forces efficiently to the tibia, this thesis is focused on the tibiofemoral joint. For the sake of simplicity, hereinafter, the tibiofemoral joint will also be referred to as the knee joint.

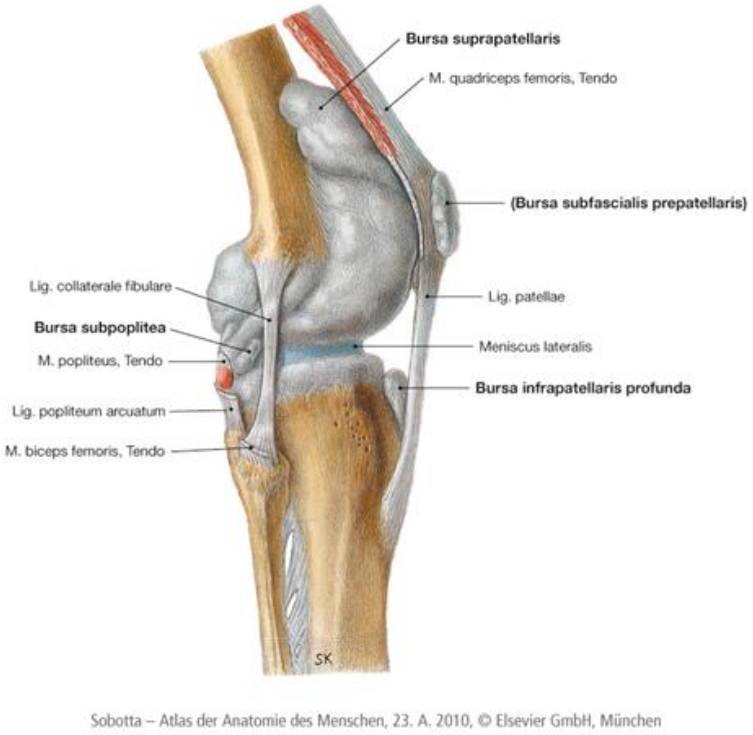

Figure 2.2 – Knee joint anatomy (lateral view in the sagittal plane). Reprinted from Paulsen, Waschke, "Sobotta Atlas of Human Anatomy", 15th Edition 2011©Elsevier GmbH, Urban & Fischer, Munich with permission from Elsevier.

The tibiofemoral joint has a complex structure interconnecting the bones with cartilage, ligaments, menisci and muscles (Figure 2.2,Figure 2.3 and Figure 2.4). This joint articulates the proximal tibia to the distal femur. The latter is composed by the medial and lateral condyles, two similar convex surfaces which couple with the tibial plateaus. These structures, differing from medial to lateral sides, show a slight concave and a convex surface, respectively. The surface of the articulating femoral condyles and tibial plateaus are covered by hyaline cartilage, whereas two c-shaped, fibrous cartilage protect the end of the bones. These c-shaped structures are called menisci and contribute to the shock absorption by lowering the pressure on the articular cartilage in the joint. In terms of mechanical properties, both menisci and cartilage exhibit nonhomogeneous and anisotropic behaviour (Tissakht and Ahmed, 1995).

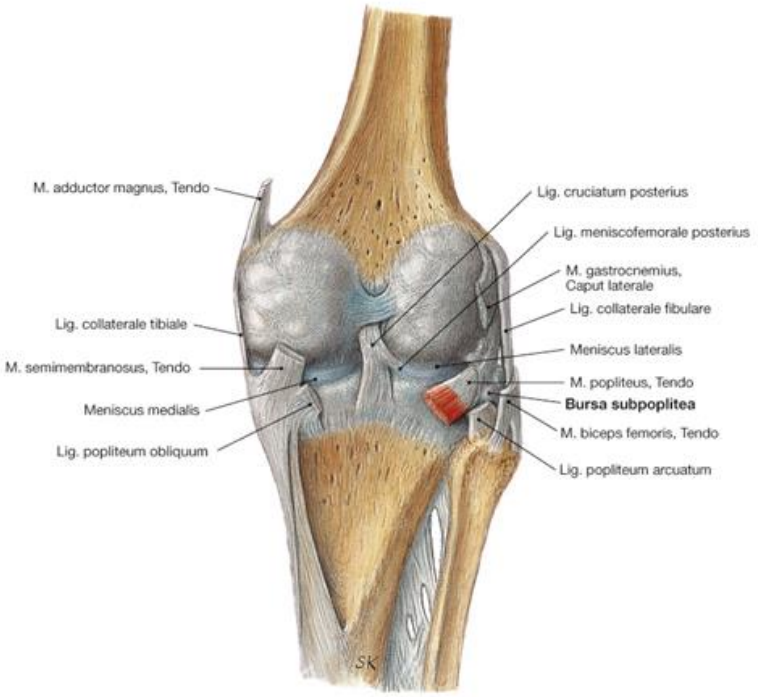

Figure 2.3 – Knee anatomy (back view in the frontal plane). Reprinted from Paulsen, Waschke, "Sobotta Atlas of Human Anatomy", 15th Edition 2011©Elsevier GmbH, Urban & Fischer, Munich with permission from Elsevier.

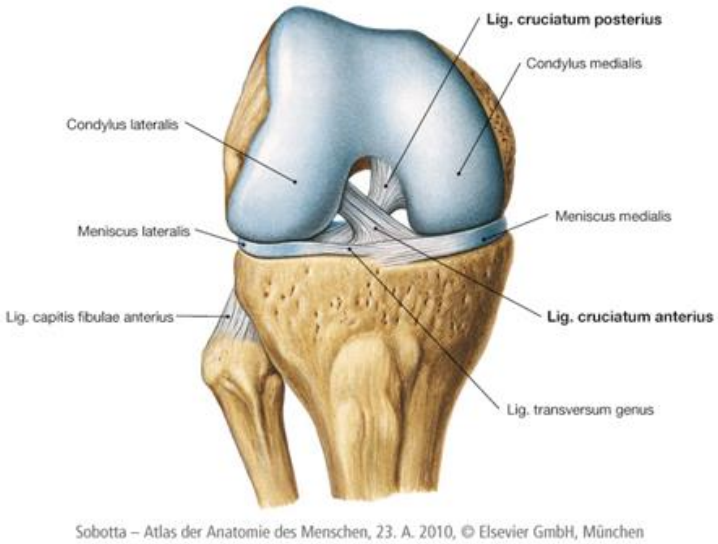

Figure 2.4 – Knee anatomy (front view in the frontal plane with no patella and joint flexed). Reprinted from Paulsen, Waschke, "Sobotta Atlas of Human Anatomy", 15th Edition 2011©Elsevier GmbH, Urban & Fischer, Munich with permission from Elsevier.

2.3. The tibiofemoral joint ligaments

Four main ligaments connect and constrain the femur to the tibia: anterior and posterior cruciate ligaments in the centre of the joint, and medial and lateral collateral ligaments on the sides (Figure 2.4). The ligaments are characterised by a strong tensile resistance so to provide guidance for natural movements and preventing simultaneously excessive motions. They are mainly composed by dense-compacted connective tissues named parallel-fibred type I collagen.

The cruciate ligaments cross each other in the middle of the knee inside the joint capsule. Their names anterior and posterior originate by their attachment positon on the tibia. The anterior cruciate ligament (ACL), composed of anteromedial and posteromedial bundles (Yagi et al., 2002), originates from the medial-posterior part of the lateral condyle, and inserts in the depression next the intercondylar eminence of the tibia, in connection with the anterior extremity of the lateral meniscus. The posterior cruciate ligament (PCL) originates from the lateral-frontal part of the medial condyle of the femur, and inserts in the posterior intercondylar fossa of the tibia. The collateral ligaments, composed of three bundles each (Park et al., 2006), keep the knee together from the medial and lateral sides. The medial collateral ligament (MCL) originates from below the adductor tubercle of the femur, and inserts in the medial condyle and medial surface of the tibia. The lateral collateral ligament (LCL) originates from the back of the lateral condyle of the femur, and inserts in the lateral side of the head of the fibula (Mader, 2004).

The mechanical function of the ligaments is to transfer load along the longitudinal direction. Their mechanical behaviour is anisotropic, non-linear, time-dependent and viscoelastic, as identified through *ex vivo* mechanical tensile testing. Performing the experiments needed to extract the parameters that describe ligament behaviour (e.g. Young's modulus, ultimate stress, and ultimate strain) is non-trivial. In fact, the cross-sectional area is not always constant along the ligament, different bundles needs to be taken into account, and ligament rupture during testing frequently occurs at the connection with the bone (Woo et al., 2006). Many different approaches have been used to quantify ligament mechanical behaviour, including strain gages (Bach and Hull, 1998), optical techniques (Woo et al., 1983), or rigid clamps (Liggins et

al., 1992; Sharkey et al., 1995). The latter remains challenging due to the common occurrence of the ligament specimens to slip from the testing machine. Liquid nitrogen or dry ice was used to address this challenge to freeze the tissue in contact with the clamp for an improved adhesion (Sharkey et al., 1995).

When a ligament or, more often, a bone-ligament-bone specimen is tested, a constant-rate force is applied, which provides the typical load-elongation relationship illustrated in Figure 2.5. From the load-elongation curve, four regions can be visually identified. The first region (Reg. 1), exhibiting a non-linear response, is usually called "toe region". At the beginning, the different collagen fibres (previously mentioned as parallel-fibred type I collagen) are assumed to be in a relaxed configuration where each of them is in a "slack" state. When the force increases, each fibre stretches in a characteristic way due to its unique configuration. This progressive recruitment of different fibres allows the whole ligament to stretch without significant damage. This condition is also described in the literature as the "crimp" (Frank, 2004). Once all the fibres are recruited, the curve becomes linear (Reg. 2). In the third region (Reg. 3), some of the fibres begin to be damaged until, as the load increases, the complete ligament rupture occurs (Reg. 4).

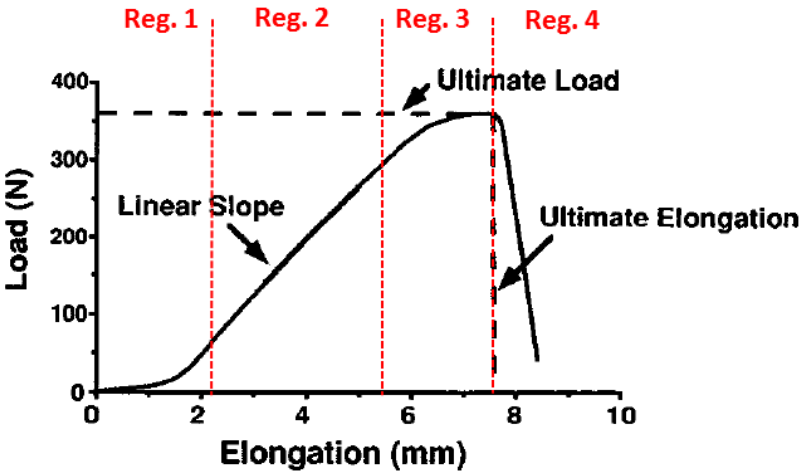

Figure 2.5 – Force-elongation curve observed for a bone-ligament-bone specimen. Four main regions can be observed in red. Reprinted with minimal adaptation from Fu et al., (1994) with permission from Elsevier.

2.3.1. ACL rupture

Due to its role in bearing a considerable part of the body weight during motion, the knee joint is quite vulnerable to different types of injuries. In the long run, degenerative diseases such as osteoarthritis tend to be predominant. This condition is characterised by the progressive erosion of the joint cartilage, requiring most likely joint replacement to alleviate the strong joint pain. Traumatic injuries are also quite common in younger populations, affecting menisci and/or ligaments. These are caused by a multidirectional combination of loads acting on the joint, which the internal structures are not able to resist.

The most common among the traumatic injuries is the ACL rupture, with an incidence ranging between 100,000 and 200,000 per year in the US (Kim et al., 2013). The injury mechanism is specifically due to an excessive extension of the joint combined with internal rotation, or flexion in conjunction with external rotation and adduction (Boden et al., 2000). The injury usually occurs during sudden and quick stops or changes in direction, which are common practice of many sports such as football, basketball, skiing and volleyball.

Once a traumatic knee injury occurs, it is important to identify its exact type, in order to decide the right treatment. The clinician in charge for the diagnosis usually asks the patients about their medical history, the symptoms at the time of the injury as well as how the injury took place. After that, a physical examination of the joint is performed, looking at swelling, pain, range of movement, strength and stability.

When looking for an ACL rupture, clinical tests are commonly used to assess the stability and laxity of the injured knee in relation with the contralateral healthy one. These tests are manually performed by the doctor and include the Lachman test and the pivot shift test (Figure 2.6). The Lachman test was originally introduced about 30 years ago (Gurtler R.A. et al., 1987), and consists of pulling the tibia forward while keeping the patient supine with a knee flexed at 20-30°. An intact ACL should be able to resist this motion, while excessive motion with a wobbling end-point suggests ligament rupture (van Eck et al., 2013). The pivot shift test, firstly described by McIntosh (1972), provides information on the ACL and menisci under

rotational stability conditions. With the patient lying in a supine and relaxed position having the hip flexed at 30° and knee fully extended, the doctor holds simultaneously the proximal tibia and the foot. The movement requires a combination of internal and adduction rotations, while slowly flexing the knee. In the range of 30-40° of knee flexion, a partial dislocation of the lateral tibial plateau is an indication of ACL rupture (Anderson et al., 2000). The ACL rupture non-invasive diagnosis can also be carried out analysing the medical imaging of the injured knee. Since the ligament of interest is located inside the joint capsule, MR images are used to look at the soft tissues and assess their status. However, despite the images seeming to represent an objective assessment tool, the patient's physical examination, conducted performing clinical tests, proved to be more accurate (82% VS 95%) (Kostov et al., 2014).

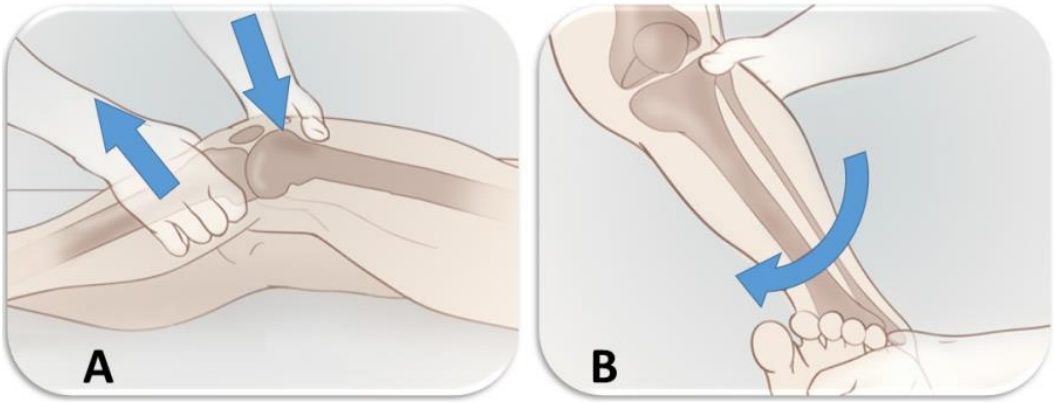

Figure 2.6 - Graphical representation of the clinical tests to assess the knee stability *in vivo*. A: Lachman test; B: pivot shift test. Adapted from http://www.clinicaladvisor.com/tests-to-assess-acl-rupture/slideshow/394/.

Following an ACL rupture, it is very difficult to trigger an healing mechanism can be triggered to restore the original mechanical stability of the joint (Schreck et al., 1995). As a consequence, an ACL reconstruction is commonly performed to allow the patient to re-gain an active lifestyle. Some patients may still decide not to perform the surgery, being aware that their joint will have rotational instability, with an increased risk for further joint damage. The surgical intervention of ACL reconstruction aims to restore the mechanical joint stability and function before the injury (Kim et al., 2013). To achieve this aim, the basic procedure involves a new ligament, which has been put in place through arthroscopy since the 1980s (Dandy

and F, 1982). This new ligament is commonly an autologous graft, meaning a part of tendon from the same patient. The usual graft options are the hamstring or the patellar tendon, positioned in place with permanently installed screws or staples (Kim et al., 2013). Even simply considering the basic procedure, several aspects can affect the outcome of the surgery. For example, the origin of the graft, the placement location, the size of the graft, the initial tension of the graft or the use of single or multiple grafts. In this scenario, there is no consensus on the best reconstructive technique (Mohtadi et al., 2011; Zantop et al., 2007), with existing short and long-term complications (Nadarajah et al., 2017). It has been shown that osteoarthritis has an increased prevalence in individuals with a previous ACL injury (up to 13%). This trend can reach up to 48% for subjects with other knee injuries (meniscus or another ligament) (Øiestad et al., 2009). Furthermore, normal or native knee kinematics and laxity is altered by the ACL reconstruction in an unknown way (Brandsson et al., 2002). Given the current situation, non-invasive methods such as computer simulations can play an important role in this field by helping the clinicians to investigate different strategies before surgery.

2.4. Elements and features of the musculoskeletal models

When investigating the joint biomechanics, the musculoskeletal system is usually modelled as a multi-element kinematic chain, in which the bones are the infinitely rigid elements of the chain, the articulations are the joints, and the muscles are the linear actuators that accelerate its elements. Once the model is fully defined, input data coming from systems able to track the motion of the human body are used.

2.4.1. Joints

Cadaveric dissections and imaging technologies have been essential to better investigate the lower limb joints' geometry and function (Delp et al., 1990; Pandy, 2001). A considerable number of *ex vivo* studies focused on bone size and orientation, joint motion, ligament and muscle attachment locations (Klein Horsman

et al., 2007; Ward et al., 2009; Yamaguchi and Zajac, 1989). Multiple challenges are faced in this category such as the age and conditions of the donors. In fact, cadaveric studies are usually based on specimens from an elderly population with different levels of muscle atrophy, weakening the ability to draw meaningful conclusions in younger and healthier populations. Recent development in imaging technologies has led to a proliferation of studies quantifying musculoskeletal anatomic features in healthy and pathological subjects (Arnold et al., 2000; Dyck et al., 2012), providing important data to inform the models.

When including the information coming from *ex vivo* studies into a model, simplifications are often needed to represent the complex geometry of bones, joints and muscles. For the bones, this refers to specific shapes used to fit specific bone portions such as a sphere for the femoral head or an ellipsoid for each of the femoral condyles. Typically, this fitting is necessary to define an underlying kinematic model of the system of bones connected by articulations (Harrington et al., 2007). Defining this coupling might be very complex in the context of MSMs, since the motion of each segment of the model is constrained to translate/rotate in a specific and pre-assigned way. The most common mechanical representations of each joint will also be presented.

2.4.1.1. The hip

The hip joint comprehends the concave pelvis acetabulum and the convex femoral head. This joint mainly orientates the thigh in three directions of space, with absolute values of average motion angle limits reaching 20° in internal-external rotation, 45° in abduction, 30° in adduction, 10° in extension and 120° in flexion. Due to the anatomical configuration of the hip joint (ball-and-socket), the spherical joint is typically used to model the mechanical behaviour of this joint (Figure 2.7). This mechanical representation enables three rotations about the anatomical axes, allowing for a physiological definition of the motion limits. This representation proved to be accurate by measuring the relative motion of the bones in cadavers using stereophotogrammetry (Cereatti et al., 2010).

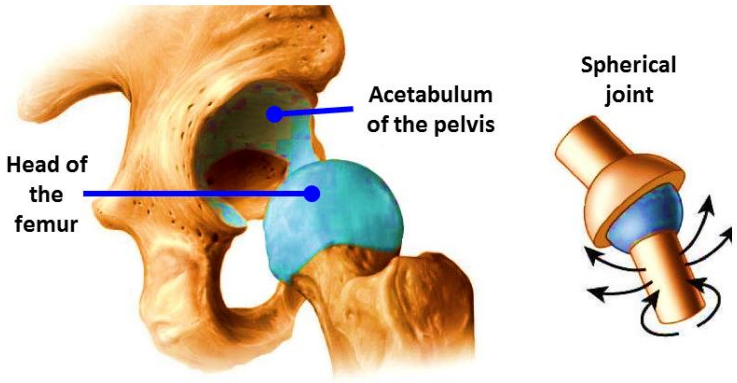

Figure 2.7 – The hip joint and its common mechanical representation. Adapted from http://www.bodywellnessprogram.com/hip-ball-and-socket-joint/hip-ball-and-socket-joint-hip-ball-and-socket-joint1-best-gym-in-brooklyn-diagrams/.

2.4.1.2. The Knee

The relative movement between the tibia and femur is best described by a combination of rolling and gliding, especially evident in the sagittal plane (Figure 2.8) but with three components of translation and three components of rotation. For an average subject, the range of motion is very complex to define because it differs reasonably when the flexion-extension angle changes (Grood, 1988) and when loads are applied (passive motion VS weight-bearing motion). Flexion can reach up to 160°, maximal extension goes from 5° to 10°. Internal-external rotation reaches values in the range of 6°-36° (Moglo and Shirazi-Adl, 2005), and it has evident coordinate coupling with the flexion-extension angle (e.g. screw-home mechanism: combined internal tibial rotation as the femur flexes and external tibial rotation as it extends). Abduction-adduction rotation is limited to a range varying between 5° and 10° (Ramsey and Wretenberg, 1999). For translations, quantitative analysis during walking assessed an anterior (posterior) displacement up to 1.3 mm (3.6 mm), a medial (lateral) displacement reaching 2.3 mm (1.5 mm), and a proximal (distal) maximal displacement of 3.2 mm (0.2 mm) (Lafortune et al., 1992).

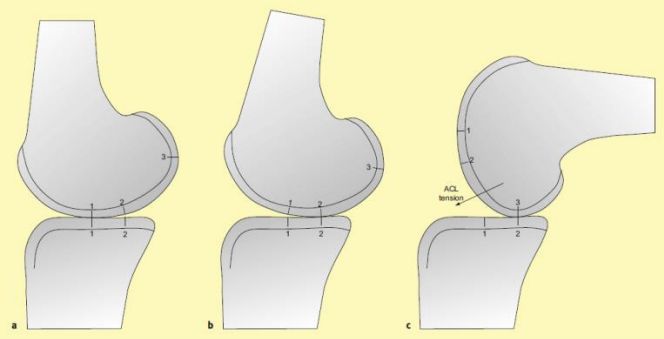

Figure 2.8 – Different phases of knee flexion. The contact point moves posteriorly starting from standing (a), and going to early (b) until deep flexion (c). Reprinted from Masouros et al., (2010) with permission from Elsevier.

For modelling purposes, the scientific community has not reached an agreement in representing the joint through an equivalent mechanism. Among the several approaches proposed so far, the one most used has been the hinge joint, allowing for a single rotation around the medio-lateral axis and resulting in only flexion-extension (Andersen et al., 2009). This one DoF mechanism neglects motion in the other rotational and translational coordinates and proved to be inadequate in representing the reported three-dimensional motion (Lu et al., 2008). The spherical joint has also been suggested (Lu and O'Connor, 1999), providing the model to freely rotate around the three coordinate axes and resulting in a three DoFs mechanism.

Single DoF alternatives have been proposed to better replicate the experimentally measured motion. The first one was based on the work carried out by Walker et al., (1988), where the flexion-extension rotation was mathematically coupled with the other coordinates, by using non-linear fitting curves. A second alternative is represented by the use of mechanical linkages to represent the tibiofemoral motion (Figure 2.9). Indeed, as shown by Wilson et al., (1998), the ACL and PCL tend to be isometric during the passive flexion of the knee. This allowed the development of several mechanical equivalents of the joint, associated with the resisting roles of anatomical structures such as ligaments (Di Gregorio and Parenti-Castelli, 2003; Gasparutto et al., 2015; Ottoboni A, Parenti-Castelli V, Sancisi N, Belvedere C, 2010).

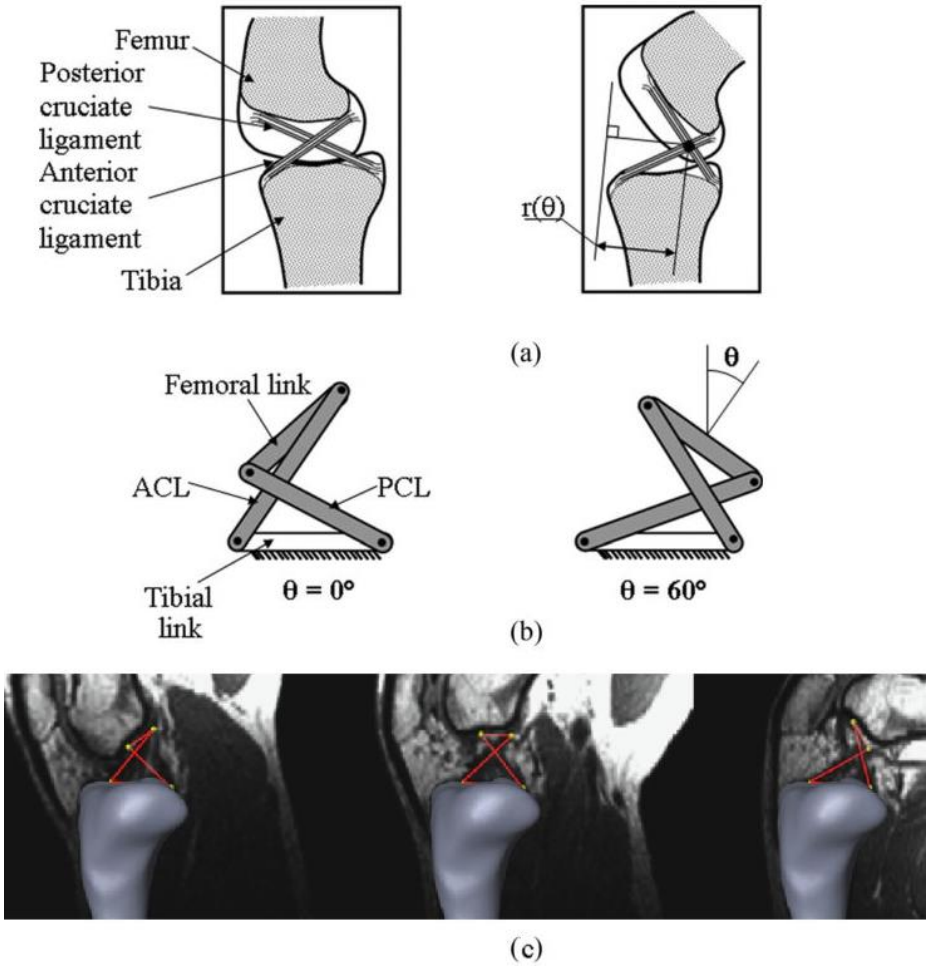

Figure 2.9 - The four-bar mechanism of the tibiofemoral joint. (a) Schematic drawing of the joint; (b) equivalent mechanism; θ: flexion angle. Obtained from Etoundi et al., (2013) with ASME permission. (c) Four-bar mechanism overlaid on the MR images acquired *in vivo* at 0°, 30° and 90° from left to right, respectively. Obtained from Heller et al., (2007) with Elsevier permission.

2.4.1.3. The Ankle

The ankle joint comprises the talocrural joint, the subtalar joint and the inferior tibiofibular joint. The ankle complex is responsible for the plantar-dorsiflexion and the inversion-eversion of the foot. Average motion limits have been reported to be around 20° for the dorsiflexion, 50° for the plantarflexion, 35° for the inversion and 15° for the eversion (Cynthia C. Norkin PT and D. Joyce White PT, 2009). In low impact activities such as walking, the ankle is commonly represented as a universal joint, allowing for the two described rotations (Delp et al., 1990; Reinbolt et al., 2005). The spherical joint (Lu and O'Connor, 1999) and the parallel mechanism have also been proposed (Franci et al., 2009).

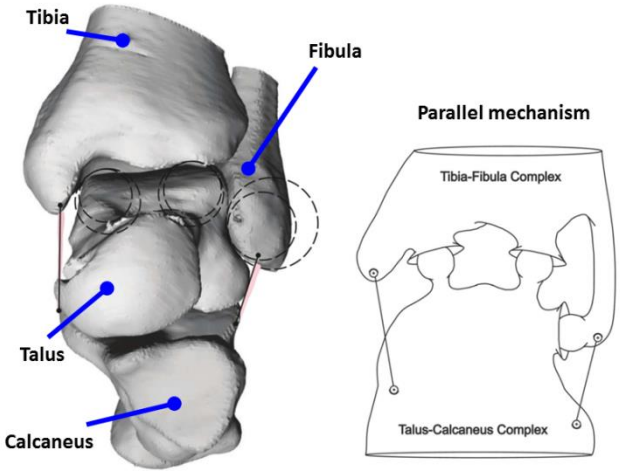

Figure 2.10 - Frontal view of the ankle joint (left) and an example of mechanical representation (right). Adapted from (Forlani et al., 2015) with ASME permission.

2.4.2. Muscles

The mechanical representation of the muscles in multi-body MSMs is usually also rather simplified. They are usually represented with multiple line actuators acting on discrete origin and attachment points on bones, whereas in reality the connection with the bone is spread over a larger area. In addition, the path of contraction of each muscle within models does not depend on the interaction among other muscles and bones. In the human body the muscles pull against each other and wrap around bones. This behaviour is also subject to variation depending on the relative limb position. To partially account for their complex muscle mechanical function, each line actuator can be defined via points, which can alter the contraction path when the relative limb position or orientation changes (see Figure 2.11 for more details and a practical example). This path alteration can be derived from medical images and is aimed at preserving a more physiological contraction mechanism in the model (Suderman and Vasavada, 2012). The way in which the muscle geometry impacts on the output of the MSMs is highly significant (Delp et al., 1990). Ultimately, some muscles span more than one articulation (i.e. rectus femoris acting on hip and knee). This prevents a study designed on one single joint, which could potentially be more detailed in terms of the description of the anatomical structure while keeping the same computational time.

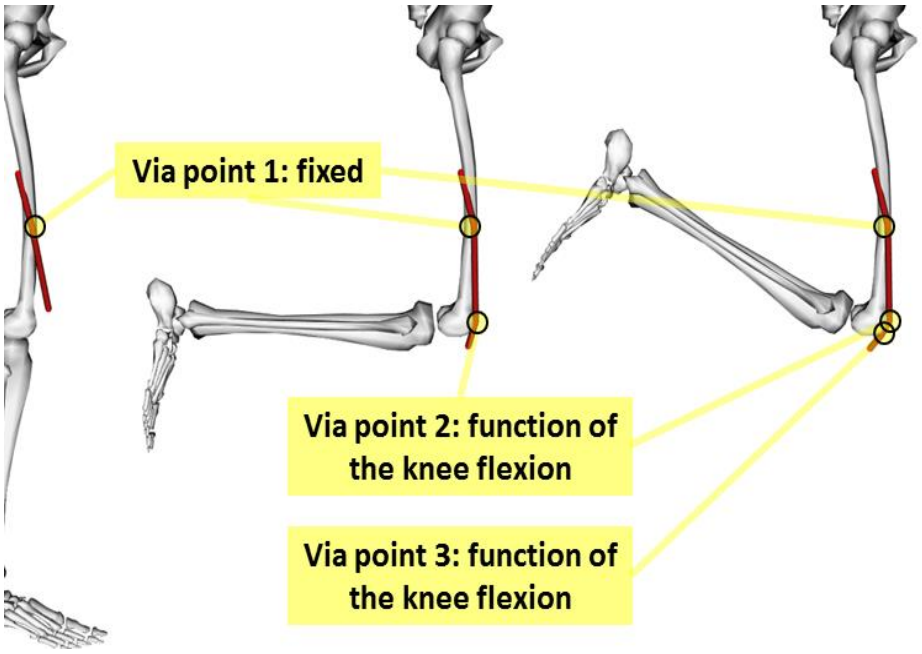

Figure 2.11 - Example of different types of muscle via points for the vastus lateralis on a lower limb MSM. These via points attempts to account for the fact that in reality the muscle is not a straight line that connect origin to insertion. They constrain the muscle to pass through specific points during the contraction path. These points can either be fixed or moving. The fixed ones have a rigid position with respect to the bone, whereas the position of the moving ones changes as a function of the joint kinematics (i.e. knee flexion in the figure).

Material properties are a critical mechanical feature to account for in a MSM. Given the assumption of rigid bodies for the bones, the attention on tissue deformation is focused on the muscles and all the parameters required to capture their complex contraction dynamics. The typical representation used in this context is the Hill-type model (Zajac, 1988). Very briefly, this model includes three components: the contractile element, the series elastic element and the parallel elastic element. The first is responsible for the active behaviour of the muscle (actin/myosin complex), providing a contraction when the muscle is activated by the neural system. The second and the third components represent the passive elasticity of the myofilaments and the connective tissue around the active muscle element, respectively (Pandy, 2001).

2.4.3. Personalization

Generic MSMs are usually developed based on dataset specific subjects (Arnold et al., 2013, 2010; Klein Horsman et al., 2007; Modenese et al., 2011). Then, scaling algorithms have been used to generate MSMs scaled to individual subjects by considering a limited number of anthropometric parameters (Delp et al., 2007). These parameters usually include segment lengths from skin-marker positions recorded in static poses and body mass, often sub-divided per segment according to literature (De Leva, 1996). To investigate overall patterns of human motions, scaled-generic models have been successful (Delp et al., 1990; Kainz et al., 2017), but the prediction of individual muscle and joint forces can be influenced by unavoidable anthropometric errors (Lenaerts et al., 2009).

The use of magnetic-resonance (MR) and computed-tomography (CT) images can enhance the level of detail in the anthropometric data necessary for MSMs in more demanding applications. Details on muscle and bone geometry can be fed in a process of defining a subject-specific MSM, allowing setting inertial properties of the bones, joint centre positions, segment axes orientations, muscle attachment sites and contraction paths (Martelli et al., 2014; Scheys et al., 2011; Valente et al., 2015). It has been shown that subject-specific models are able to provide more accurate results when compared to scaled-generic models (Correa et al., 2012), however challenges related to model generation and validation still prevent for an extensive use of these models in practice (Hicks et al., 2015; Valente et al., 2015).

2.5. Inverse dynamics pipeline

The utility of defining a model of the musculoskeletal system is associated with its ability to provide non-invasive, reliable predictions of different physical quantities of interest. For instance, estimating the position, velocity and acceleration of the different body segments can help to quantitatively describe a motor task. Besides, joint angles can inform on the relative position between adjacent body segments. Eventually, the loads involved during movement (i.e. joint moments, muscle forces or joint contact forces) can help to better understand the biomechanics of the movement and make informed clinical decisions. In particular, to predict muscle

behaviour and joint contact forces, either an inverse or a forward dynamics approach can be used. Both methods have advantages and disadvantages to take into account (Erdemir et al., 2007).

In this thesis, the adopted choice has been to focus the work on the inverse dynamics approach, since it allows including the knee joint model developed and it is less computationally demanding when compared with the forward dynamics approach. The mathematical formulation of the inverse dynamics approach will be described in the following section. In addition, Figure 2.12 provides a schematic representation of the different steps involved to clearly understand the connections.

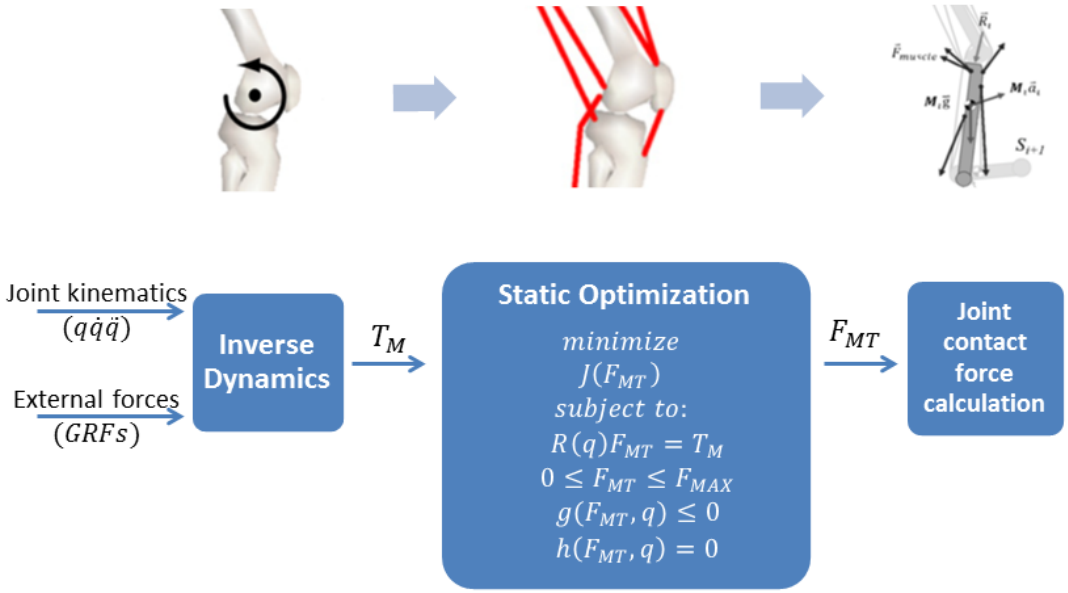

Figure 2.12 – Schematic representation of the inverse dynamics pipeline.

2.5.1. Input data

2.5.1.1. Ground reaction forces

Following an inverse dynamics approach requires the input measurements of the instantaneous bone position and orientation in the three-dimensional space (i.e. bone pose) and of the ground reaction forces (GRFs). GRFs exchanged between the body and the ground are typically measured using force platforms, which are known to have a high level of accuracy (Hatze, 2002) whereas different methods, with their advantages and disadvantages, might be used to record the bone pose.

2.5.1.2. Body segments kinematics

Optoelectronic stereophotogrammetry (Figure 2.13) refers to a range of techniques used to reconstruct the position of 3D objects from the combination of multiple 2D images (Chiari et al., 2005). Infra-red cameras permit individually recording a 2D image of the scene as a discrete set of target points. These targets are usually retro-reflective passive markers, which are detected because they reflect back the light emitted by each camera. The 3D position of the markers in the space is reconstructed by a workstation, processing the information coming from the 2D images from multiple perspectives.

The ability to capture the human motion is associated with reliable identification of specific locations on the human body skeleton. These locations are defined as anatomical landmarks (Cappozzo et al., 1995). In order to identify these landmarks, the skin is palpated in specific points looking for bone prominences associated with each landmark. Once the landmark is identified, the corresponding target marker is placed on the skin (i.e. marker placement). This procedure is subject to errors (i.e. marker misplacement) which can impact on the joint kinematics (Della Croce et al., 2005). To reduce these errors, multiple techniques have been developed and compared each other's (della Croce et al., 1999; Stagni et al., 2006).

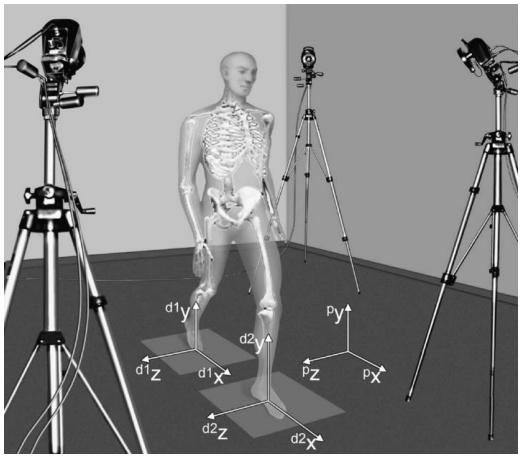

Figure 2.13 - Gait laboratory equipped with optoelectronic stereophotogrammetric system. Reprinted from Cappozzo et al., (2005) with permission from Elsevier.

Despite being an accurate technology, optoelectronic stereophotogrammetry suffers from a major drawback when used for describing human motion (Chiari et al., 2005).

During the measurement of a movement, instantaneous positions of reflective markers located on the skin surface of the subjects are tracked, aiming at capturing the underlying skeleton pose. However, the markers cannot be considered rigid with the underlying bone due to skin deformation and displacement, and a consequent non-negligible source of error must be carefully taken into account. This error is known in literature as STA (Leardini et al., 2005). Unfortunately, despite a large body of literature available on the topic thanks to the effort of the human movement research community (Aurelio Cappozzo et al., 1996; Leardini et al., 2005; Lu and O'Connor, 1999; Lucchetti et al., 1998), this error appears less discussed by the modelling community. This situation can lead to unrealistic estimates of the MSMs.

The STA is generated by three main phenomena, ranked from the most to the least important: the skin sliding during motion, soft tissue deformation in response to muscle contraction, and inertial effects combined with gravity (Bonci et al., 2014). The most important features of STA are that it is subject-, location- and motor task-specific. This means that it is strongly correlated to the anatomy of the particular subject (Benoit et al., 2006), the location of the markers attached on the skin (Stagni et al., 2005), the investigated movement coupled with the range of motion it covers (Camomilla et al., 2009).

Both filtering and smoothing techniques have been explored to eliminate or mitigate the effects of STA, but the outcomes resulted in the loss of pertinent data or the introduction of further noise (Fuller et al., 1997). For these reasons, it is still very difficult to compensate the source of error coming from STA.

Several studies have been conducted aiming at quantifying the STA with the aim of modelling and compensating it. To accomplish this, a "gold standard" is needed to directly measure the relative pose between adjacent bones. Two main strategies have been proposed in the past. One strategy consists of the invasive fixation of references directly in bones such as intracortical pins (A Cappozzo et al., 1996; Fuller et al., 1997). The second strategy is non-invasive and use mono- or bi-plane fluoroscopy systems to track the bone motion (Banks and Hodge, 1996; Tsai et al., 2009). Both strategies have been successfully implemented. In particular during gait, Fuller et al. (1997) measured a STA up to 20 mm near the femoral condyle, a common

attachment site for skin-mounted markers. Cappozzo et al. (1996) showed a STA range between 10 and 30 mm for skin markers on both tibial and femoral anatomical landmarks. Tsai et al. (2009) investigated the STA during different tasks and showed that in the stance phase of gait, the maximal peak error on femoral and tibial skin markers was 23.2 mm and 9.7mm respectively.

In recent years, STA models have started to be developed and implemented (Andersen et al., 2012; Bonci et al., 2014; Dumas et al., 2014). The idea is that by modelling the STA behaviour, it could be possible to specifically identify and possibly remove the STA contribution when measuring the skin marker positon using stereophotogrammetry. For example, these models can be embedded into MBO algorithms to better reconstruct the skeletal motion (Richard et al., 2012).

The consequence of this input error in estimating the joint kinematics is quite dramatic, in the sense that only the large amplitude movements (e.g. knee flexion-extension during gait) can generate trusted predictions when using stereophotogrammetric surface marker data. Despite many studies in this field, there are no conclusive ways to deal with the STA, and it still represents an open issue to address.

To cope with the STA, different techniques have been introduced, which are known as MBO methods. These methods allow estimations of the skeletal pose for each segment and the consequent relative motion at each joint (i.e. named joint kinematics or joint angles), starting from stereophotogrammetric skin-marker data.

MBO (Cereatti et al., 2017), original proposed as a global optimisation method (Lu and O'Connor, 1999), is defined as a "*Method based on the global minimisation of the overall measurement errors with joint constraints for the simultaneous determination of the spatial pose of all segments of a multi-link model of the locomotor musculoskeletal system*". The aim of this method is to optimally estimate the skeletal pose of the system, preventing joint dislocation in the models (i.e. the abnormal separation of two adjacent bones in a joint) and limiting STA propagation (Andersen et al., 2009; Lu and O'Connor, 1999; Reinbolt et al., 2005; Scheys et al., 2011; Stagni et al., 2009).

This method is based on the concepts of "experimental" and "virtual" markers. Experimental markers are the surface markers placed on the skin of a subject in a gait laboratory. Their three-dimensional position is measured using stereophotogrammetry during motion, without implying any mathematical relations among markers. On the contrary, virtual markers are placed directly on the MSM, ideally in the corresponding location to the experimental ones. The virtual markers are rigidly attached to each bony segment, and their motion is directly related to the motion of the model, specified by the joints (see section number 2.4.1.).

In terms of the mathematical problem, this method entails the minimisation of the least squares of the distance between experimental markers on the subject and virtual markers on the model. The following equation shows the formulation of the problem:

$$\min_{q} \sum_{i=1}^{k} w_i \left\| x_i^{exp} - x_i(q) \right\|^2 \qquad 2.1$$

Where q represents the joint angles to be determined; x_i^{exp} are the positions of the experimental markers; $x_i(q)$ are the positions of the virtual markers, which, as previously explained, are expressed as a function of the joint angles; i and k are the current and total number of markers, respectively; and w_i are weight factors varying between 0 and 1, which are assigned according to the level of trust for each marker (1: total trust; 0=no trust).

As detailed in 2.4.1. , different mechanical representations can be used for each joint. Associated to each of these, a joint constrained is defined to strictly specify the relative motion between adjacent segments, indirectly affecting the allowed position of the virtual markers in space (Equation 2.1). This strict definition of the relative joint motion assumes that the mechanical equivalent represents the actual joint motion. This assumption has been introduced with the name of "hard" constraints, characterised by a joint motion prescribed without any flexibility. As an alternative, the so-called "soft" constraints have been proposed, which allow the joint to flexibly adapt to different conditions, while following certain rules. These rules might include, for example, allowing the ligaments to deform (while the "hard" constraints

are associated with ligament of constant length during motion) by defining a penalty-based method which minimises the ligament length variations (Gasparutto et al., 2013).

Alternatively, the knee joint can be mechanically characterised by its elastic energy derived from a 6DoFs stiffness matrix. In this case, minimising the deformation energy provides a flexible way to estimate joint kinematics (Richard et al., 2016). These "soft" constraints open new ways to better represent the joints in MSMs, but they require re-implementing MBO algorithms differing from its classical definition (Equation 2.1), which only allows for "hard" constraints. The second part of Chapter 4 will describe in detail the development of this new approach and the mathematical foundations on which it sits.

2.5.2. Equations of motion

Once the joint kinematics has been estimated, the musculoskeletal dynamics starts to play a role in the inverse dynamics pipeline (Figure 2.12). Consider a musculoskeletal system where *n* is the total number of joint DoFs and q represents the joint angles, the equations of motion involved in this problem are shown in matrix form by the Equation 2.2:

$$M(q)\ddot{q} + C(q,\dot{q}) + G(q) + T_M + F_{EXT} = 0 \qquad 2.2$$

Where $M(q)$ represents the system mass matrix (*n x n*); $C(q,\dot{q})$ is the centrifugal and Coriolis force (*n x 1*); $G(q)$ is the gravitational force (*n x 1*); T_M is the muscular joint torque (*n x 1*) and F_{EXT} is the external force (*n x 1*). To initially solve the equation to find T_M (typically called joint moments), an inverse dynamic problem is faced by inputting the joint kinematics and the GRFs. This is performed recursively solving Equation 2.3 at each segment, starting from the foot and moving proximally (Erdemir et al., 2007).

$$T_M = M(q)\ddot{q} + C(q,\dot{q}) + G(q) + F_{EXT} \qquad 2.3$$

2.5.3. Estimate of muscle forces

The joint moments predicted by the inverse dynamics are used for estimating muscle activations and forces. This step requires an optimisation procedure because there are usually more muscles than equations of motion to solve. In fact, each of the n lines of the matrix form of Equation 2.2 corresponds to a specific DoFs in the MSM. As a result, the so-called myoskeletal indeterminacy problem needs to be solved (Viceconti et al., 2006). This concept can be clarified by expanding the term T_M in Equation 2.2. In particular (see Equation 2.4), the joint moments are equal to the product between $R(q)$, the muscular moment arm (n x m) and F_{MT}, the individual muscle forces (m x 1, m: number of muscles).

$$T_M = R(q)F_{MT} \tag{2.4}$$

Since usually $m > n$, the resultant system is redundant and admits infinite solutions. The choice of the optimisation function is crucial to select one among the possible solutions, i.e. the muscle activation pattern among those that comply with muscle physiology as well as respecting the constraints of the model (Anderson and Pandy, 2001; Erdemir et al., 2007).

The general formulation of the optimisation problem is called static optimisation (described by Equation 2.5). This problem, originally introduced by (Hardt, 1978), is computationally efficient and easy to implement because multiple integrations are not required (Erdemir et al., 2007).

$$minimize \quad J(F_{MT}); \quad subject\ to \quad \begin{matrix} R(q)F_{MT} = T_M \\ 0 \le F_{MT} \le F_{MAX} \\ g(F_{MT}, q) \le 0 \\ h(F_{MT}, q) = 0 \end{matrix} \tag{2.5}$$

In order to compute the unknown muscular forces, an objective function $J(F_{MT})$ has to be minimised. Multiple objective functions have been proposed so far, with the resulting outcome compared in different studies (Collins, 1995; Wesseling et al., 2015). The most commonly used is the sum of the total squared of muscle activations (Equation 2.6), because of the good agreement shown against the surface

electromyographic signal (sEMG) as well as the ability to accurately estimate the hip contact force (Modenese et al., 2011).

$$J(F_{MT}) = \sum_{i=1}^{m} \left(\frac{F_i}{F_{i,max}} \right)^2 \quad 2.6$$

Where F_i is the force magnitude of each muscle and $F_{i,max}$ is its corresponding maximal value that the same muscle can produce. The usual constraint to the optimisation is that the estimated muscle forces multiplied by the moment arm of each muscle have to balance the joint moments outputted by the inverse dynamics. Additional constraints are related to muscle physiology (i.e. limit on the maximal force generated by each muscle), muscle contraction dynamics (i.e. force-length-velocity relationship) or can be related to the specific joint under investigation (constraints on the direction or the maximal magnitude of the contact force).

2.5.4. Estimate of joint contact forces

Once the muscle forces are estimated, the joint contact forces can be calculated in the last step of the pipeline (Figure 2.12). They account for the loads transmitted between two adjacent bodies, which are not considered in the model simplification (i.e. internal loads carried by the joint structure such as meniscus, ligaments or bone-to-bone contact). These forces can be computed from the equilibrium equations of each body using the free body diagram (Equation 2.7), where everything else is known from the previous steps (Steele et al., 2012).

$$JCF + \sum_{i=1}^{m} F_{MT}^{i} + \sum_{k=1}^{m} F_{EXT}^{i} + G = M\ddot{q} \quad 2.7$$

References

Andersen, M.S., Damsgaard, M., Rasmussen, J., 2009. Kinematic analysis of over-determinate biomechanical systems. Comput. Methods Biomech. Biomed. Engin. 12, 371–384. doi:10.1080/10255840802459412

Andersen, M.S., Damsgaard, M., Rasmussen, J., Ramsey, D.K., Benoit, D.L., 2012. A linear soft tissue artefact model for human movement analysis: Proof of concept using in vivo data. Gait Posture 35, 606–611. doi:10.1016/j.gaitpost.2011.11.032

Anderson, A.F., Rennirt, G.W., Standeffer Jr., W.C., 2000. Clinical analysis of the pivot shift tests: description of the pivot drawer test. Am. J. Knee Surg. 13, 19–24. doi:10.1556/AAlim.2015.0002

Anderson, F.C., Pandy, M.G., 2001. Static and dynamic optimization solutions for gait are practically equivalent. J. Biomech. 34, 153–161. doi:10.1016/S0021-9290(00)00155-X

Arnold, a S., Salinas, S., Asakawa, D.J., Delp, S.L., 2000. Accuracy of muscle moment arms estimated from MRI-based musculoskeletal models of the lower extremity. Comput. Aided Surg. 5, 108–19. doi:10.1002/1097-0150(2000)5:2<108::AID-IGS5>3.0.CO;2-2

Arnold, E.M., Hamner, S.R., Seth, A., Millard, M., Delp, S.L., 2013. How muscle fiber lengths and velocities affect muscle force generation as humans walk and run at different speeds. J. Exp. Biol. 216, 2150–2160. doi:10.1242/jeb.075697

Arnold, E.M., Ward, S.R., Lieber, R.L., Delp, S.L., 2010. A model of the lower limb for analysis of human movement. Ann. Biomed. Eng. 38, 269–79. doi:10.1007/s10439-009-9852-5

Bach, J.M., Hull, M.L., 1998. Strain inhomogeneity in the anterior cruciate ligament under application of external and muscular loads. J. Biomech. Eng. 120, 497–503.

Banks, S., Hodge, W., 1996. Accurate measurement of three dimensional knee replacement kinematics using single-plane flouroscopy. IEEE Trans. Biomed. Eng. 46, 638–649.

Benoit, D.L., Ramsey, D.K., Lamontagne, M., Xu, L., Wretenberg, P., Renström, P., 2006. Effect of skin movement artifact on knee kinematics during gait and cutting motions measured in vivo. Gait Posture 24, 152–164. doi:10.1016/j.gaitpost.2005.04.012

Boden, B.P., Dean, G.S., Feagin, J.A., Garrett, W.E., 2000. Mechanisms of anterior cruciate ligament injury. Orthopedics 23, 573–578. doi:10.1016/j.ptsp.2008.01.002

Bonci, T., Camomilla, V., Dumas, R., Chèze, L., Cappozzo, A., 2014. A soft tissue artefact model driven by proximal and distal joint kinematics. J. Biomech. 47, 2354–61. doi:10.1016/j.jbiomech.2014.04.029

Brandsson, S., Karlsson, J., Swärd, L., Kartus, J., Eriksson, B.I., Kärrholm, J., 2002.

Kinematics and laxity of the knee joint after anterior cruciate ligament reconstruction: pre- and postoperative radiostereometric studies. Am. J. Sports Med. 30, 361–367.

Camomilla, V., Donati, M., Stagni, R., Cappozzo, A., 2009. Non-invasive assessment of superficial soft tissue local displacements during movement: a feasibility study. J. Biomech. 42, 931–7. doi:10.1016/j.jbiomech.2009.01.008

Cappozzo, A., Catani, F., Della Croce, U., Leardini, A., 1995. Position and orientation in space of bones during movement: Anatomical frame definition and determination. Clin. Biomech. 10, 171–178. doi:10.1016/0268-0033(95)91394-T

Cappozzo, A., Catani, F., Leardini, A., 1996. Position and orientation in space of bones during movement: experimental artefacts. Clin. Biomech.

Cappozzo, A., Catani, F., Leardini, A., Benedetti, M.G., Della Croce, U., 1996. Position and orientation in space of bones during movement: Experimental artefacts. Clin. Biomech. 11, 90–100. doi:10.1016/0268-0033(95)00046-1

Cappozzo, A., Della Croce, U., Leardini, A., Chiari, L., 2005. Human movement analysis using stereophotogrammetry. Part 1: theoretical background. Gait Posture 21, 186–196. doi:10.1016/j.gaitpost.2004.01.010

Cereatti, A., Bonci, T., Akbarshahi, M., Aminian, K., Barré, A., Begon, M., Benoit, D.L., Charbonnier, C., Maso, F.D., Fantozzi, S., Lin, C.-C., Lu, T.-W., Pandy, M.G., Stagni, R., van den Bogert, A.J., Camomilla, V., 2017. Standardization proposal of soft tissue artefact description for data sharing in human motion measurements. J. Biomech. doi:10.1016/j.jbiomech.2017.02.004

Cereatti, A., Margheritini, F., Donati, M., Cappozzo, A., 2010. Is the human acetabulofemoral joint spherical? J. Bone Joint Surg. Br. 92, 311–314. doi:10.1302/0301-620X.92B2.22625

Chiari, L., Della Croce, U., Leardini, A., Cappozzo, A., 2005. Human movement analysis using stereophotogrammetry. Part 2: Instrumental errors. Gait Posture 21, 197–211. doi:10.1016/j.gaitpost.2004.04.004

Collins, J., 1995. The redundant nature of locomotor optimization laws. J. Biomech. 28.

Correa, T.A., Schache, A.G., Graham, H.K., Baker, R., Thomason, P., Pandy, M.G., 2012. Potential of lower-limb muscles to accelerate the body during cerebral palsy gait. Gait Posture 36, 194–200. doi:10.1016/j.gaitpost.2012.02.014

Cynthia C. Norkin PT, E., D. Joyce White PT, D.S., 2009. Measurement of Joint Motion A Guide to Goniometry, 4th ed., Journal of Chemical Information and Modeling. doi:10.2310/6640.2004.00031

Dandy, D.J., F, O.P., 1982. Arthroscopic surgery of the knee. Br. Med. J. 285, 1256–58. doi:10.1136/bmj.285.6350.1256

De Leva, P., 1996. Adjustments to zatsiorsky-seluyanov's segment inertia parameters. J. Biomech. 29, 1223–1230. doi:10.1016/0021-9290(95)00178-6

della Croce, U., Cappozzo, a, Kerrigan, D.C., 1999. Pelvis and lower limb anatomical landmark calibration precision and its propagation to bone geometry

and joint angles. Med. Biol. Eng. Comput. 37, 155–161. doi:10.1007/BF02513282

Della Croce, U., Leardini, A., Chiari, L., Cappozzo, A., 2005. Human movement analysis using stereophotogrammetry Part 4: Assessment of anatomical landmark misplacement and its effects on joint kinematics. Gait Posture 21, 226–237. doi:10.1016/j.gaitpost.2004.05.003

Delp, S.L., Anderson, F.C., Arnold, A.S., Loan, P., Habib, A., John, C.T., Guendelman, E., Thelen, D.G., 2007. OpenSim: Open-Source Software to Create and Analyze Dynamic Simulations of Movement. IEEE Trans. Biomed. Eng. 54, 1940–1950. doi:10.1109/TBME.2007.901024

Delp, S.L., Loan, J.P., Hoy, M.G., Zajac, F.E., Topp, E.L., Rosen, J.M., 1990. An interactive graphics-based model of the lower extremity to study orthopaedic surgical procedures. IEEE Trans. Biomed. Eng. 37, 757–67. doi:10.1109/10.102791

Di Gregorio, R., Parenti-Castelli, V., 2003. A Spatial Mechanism With Higher Pairs for Modelling the Human Knee Joint. J. Biomech. Eng. 125, 232–7. doi:10.1115/1.1559895

Dumas, R., Camomilla, V., Bonci, T., Cheze, L., Cappozzo, a., 2014. Generalized mathematical representation of the soft tissue artefact. J. Biomech. 47, 476–481. doi:10.1016/j.jbiomech.2013.10.034

Dyck, P., Smet, E., Veryser, J., Lambrecht, V., Gielen, J.L., Vanhoenacker, F.M., Dossche, L., Parizel, P.M., 2012. Partial tear of the anterior cruciate ligament of the knee: injury patterns on MR imaging. Knee Surgery, Sport. Traumatol. Arthrosc. 20, 256–261. doi:10.1007/s00167-011-1617-7

Erdemir, A., McLean, S., Herzog, W., van den Bogert, A.J., 2007. Model-based estimation of muscle forces exerted during movements. Clin. Biomech. (Bristol, Avon) 22, 131–54. doi:10.1016/j.clinbiomech.2006.09.005

Etoundi, A.C., Burgess, S.C., Vaidyanathan, R., 2013. A Bio-Inspired Condylar Hinge for Robotic Limbs. J. Mech. Robot. 5, 31011. doi:10.1115/1.4024471

Forlani, M., Sancisi, N., Parenti-Castelli, V., 2015. A Three-Dimensional Ankle Kinetostatic Model to Simulate Loaded and Unloaded Joint Motion. J. Biomech. Eng. 137, 61005. doi:10.1115/1.4029978

Franci, R., Parenti-Castelli, V., Belvedere, C., Leardini, A., 2009. A new one-DOF fully parallel mechanism for modelling passive motion at the human tibiotalar joint. J. Biomech. 42, 1403–1408. doi:10.1016/j.jbiomech.2009.04.024

Frank, C.B., 2004. Ligament structure, physiology and function. J. Musculoskelet. Neuronal Interact. 4, 199–201.

Fu, F.H., Woo, S.L., Ph, D., 1994. Biomechanical Function of the Human Anterior Cruciate Ligament. Arthroscopy 10, 140–147. doi:10.1016/S0749-8063(05)80081-7

Fuller, J., Liu, L.-J., Murphy, M.C., Mann, R.W., 1997. A comparison of lower-extremity skeletal kinematics measured using skin- and pin-mounted markers. Hum. Mov. Sci. 16, 219–242. doi:10.1016/S0167-9457(96)00053-X

Gage, B.E., McIlvain, N.M., Collins, C.L., Fields, S.K., Comstock, R.D., 2012. Epidemiology of 6.6 million knee injuries presenting to United States emergency departments from 1999 through 2008. Acad. Emerg. Med. 19, 378–85. doi:10.1111/j.1553-2712.2012.01315.x

Galway, R., Beaupre, A., MacIntosh, D., 1972. Pivot shift: a clinical sign of symptomatic anterior cruciate insufficiency. J Bone Jt. Surg [Br] 54, 763–4.

Gasparutto, X., Dumas, R., Jacquelin, E., 2013. Multi-body optimisation with deformable ligament constraints: influence of ligament geometry. Comput. Methods Biomech. Biomed. Engin. 15, 191–193. doi:10.1080/10255842.2012.744189

Gasparutto, X., Sancisi, N., Jacquelin, E., Parenti-Castelli, V., Dumas, R., 2015. Validation of a multi-body optimization with knee kinematic models including ligament constraints. J. Biomech. 48, 1141–1146. doi:10.1016/j.jbiomech.2015.01.010

Grood, E., 1988. Limits of movement in the human knee. Effect of sectioning the posterior cruciate ligament and posterolateral structures. J Bone Jt. Surg Am 88–97.

Hardt, D.E., 1978. Determining muscle forces in the leg during normal human walking - An application and evaluation of optimization methods. J. Biomech. Eng. doi:10.1115/1.3426195

Harrington, M.E., Zavatsky, a. B., Lawson, S.E.M., Yuan, Z., Theologis, T.N., 2007. Prediction of the hip joint centre in adults, children, and patients with cerebral palsy based on magnetic resonance imaging. J. Biomech. 40, 595–602. doi:10.1016/j.jbiomech.2006.02.003

Hatze, H., 2002. The fundamental problem of myoskeletal inverse dynamics and its implications. J. Biomech. 35, 109–115. doi:10.1016/S0021-9290(01)00158-0

Heller, M.O., König, C., Graichen, H., Hinterwimmer, S., Ehrig, R.M., Duda, G.N., Taylor, W.R., 2007. A new model to predict in vivo human knee kinematics under physiological-like muscle activation. J. Biomech. 40 Suppl 1, S45-53. doi:10.1016/j.jbiomech.2007.03.005

Hicks, J.L., Uchida, T.K., Seth, A., Rajagopal, A., Delp, S., 2015. Is my model good enough? Best practices for verification and validation of musculoskeletal models and simulations of human movement. J. Biomech. Eng. 137. doi:10.1115/1.4029304

Hyman, L.H., Wake, M.H., 1992. Hyman's comparative vertebrate anatomy. 788. doi:10.1038/152088a0

Kainz, H., Hoang, H., Stockton, C., Boyd, R.R., Lloyd, D.G., Carty, C.P., 2017. Accuracy and Reliability of Marker Based Approaches to Scale the Pelvis, Thigh and Shank Segments in Musculoskeletal Models. J. Appl. Biomech. 1–21. doi:10.1123/jab.2016-0282

Kim, H.S., Seon, J.K., Jo, A.R., 2013. Current Trends in Anterior Cruciate Ligament Reconstruction. Knee Surg. Relat. Res. 25, 165–173. doi:10.5792/ksrr.2013.25.4.165

Klein Horsman, M.D., Koopman, H.F.J.M., van der Helm, F.C.T., Prosé, L.P.,

Veeger, H.E.J., 2007. Morphological muscle and joint parameters for musculoskeletal modelling of the lower extremity. Clin. Biomech. (Bristol, Avon) 22, 239–47. doi:10.1016/j.clinbiomech.2006.10.003

Kostov, H., Arsovski, O., Kostova, E., Nikolov, V., 2014. Diagnostic assessment in anterior cruciate ligament (ACL) tears. Prilozi 35, 209–18.

Lafortune, M. a, Cavanagh, P.R., Sommer, H.J., Kalenak, a, 1992. Three-dimensional kinematics of the human knee during walking. J. Biomech. 25, 347–57.

Leardini, A., Chiari, L., Della Croce, U., Cappozzo, A., 2005. Human movement analysis using stereophotogrammetry. Part 3. Soft tissue artifact assessment and compensation. Gait Posture 21, 212–25. doi:10.1016/j.gaitpost.2004.05.002

Lenaerts, G., Bartels, W., Gelaude, F., Mulier, M., Spaepen, A., Van der Perre, G., Jonkers, I., 2009. Subject-specific hip geometry and hip joint centre location affects calculated contact forces at the hip during gait. J. Biomech. 42, 1246–1251. doi:10.1016/j.jbiomech.2009.03.037

Liggins, A.B., Shemerluk, R., Hardie, R., Finlay, J.B., 1992. Technique for the application of physiological loading to soft tissue in vitro. J. Biomed. Eng. 14, 440–441. doi:10.1016/0141-5425(92)90092-Y

Lu, T.-W., O'Connor, J.J., 1999. Bone position estimation from skin marker co-ordinates using global optimisation with joint constraints. J. Biomech. 32, 129–134. doi:10.1016/S0021-9290(98)00158-4

Lu, T.-W., Tsai, T.-Y., Kuo, M.-Y., Hsu, H.-C., Chen, H.-L., 2008. In vivo three-dimensional kinematics of the normal knee during active extension under unloaded and loaded conditions using single-plane fluoroscopy. Med. Eng. Phys. 30, 1004–12. doi:10.1016/j.medengphy.2008.03.001

Lucchetti, L., Cappozzo, A., Cappello, A., Della Croce, U., 1998. Skin movement artefact assessment and compensation in the estimation of knee-joint kinematics. J. Biomech. 31, 977–984. doi:10.1016/S0021-9290(98)00083-9

Mader, S.S., 2004. Mader: Understanding Human Anatomy and Physiology, Cell Structure and Function. doi:10.1177/0011392199047004007

Martelli, S., Valente, G., Viceconti, M., Taddei, F., 2014. Sensitivity of a subject-specific musculoskeletal model to the uncertainties on the joint axes location. Comput. Methods Biomech. Biomed. Engin. 18, 1555–63. doi:10.1080/10255842.2014.930134

Masouros, S.D., Bull, A.M.J., Amis, A.A., 2010. (i) Biomechanics of the knee joint. Orthop. Trauma 24, 84–91. doi:10.1016/j.mporth.2010.03.005

Modenese, L., Phillips, a. T.M., Bull, a. M.J., 2011. An open source lower limb model: Hip joint validation. J. Biomech. 44, 2185–2193. doi:10.1016/j.jbiomech.2011.06.019

Moglo, K.E., Shirazi-Adl, A., 2005. Cruciate coupling and screw-home mechanism in passive knee joint during extension-flexion. J. Biomech. 38, 1075–1083. doi:10.1016/j.jbiomech.2004.05.033

Mohtadi, N.G., Chan, D.S., Dainty, K.N., Whelan, D.B., 2011. Patellar tendon

versus hamstring tendon autograft for anterior cruciate ligament rupture in adults. Cochrane Database Syst. Rev. 9, CD005960. doi:10.1002/14651858.CD005960.pub2

Nadarajah, V., Roach, R., Ganta, A., Alaia, M.J., Shah, M.R., 2017. Primary anterior cruciate ligament reconstruction: perioperative considerations and complications. Phys. Sportsmed. 0, 1–13. doi:10.1080/00913847.2017.1294012

Øiestad, B.E., Engebretsen, L., Storheim, K., Risberg, M.A., 2009. Knee osteoarthritis after anterior cruciate ligament injury: a systematic review. Am. J. Sports Med. 37, 1434–43. doi:10.1177/0363546509338827

Ottoboni A, Parenti-Castelli V, Sancisi N, Belvedere C, L.A., 2010. Articular surface approximation in equivalent spatial parallel mechanism models of the human knee joint: an experiment-based assessment., in: Proc Inst Mech Eng H.

Pandy, M., 2001. Computer modeling and simulation of human movement. Annu. Rev. Biomed. Eng.

Park, S.E., DeFrate, L.E., Suggs, J.F., Gill, T.J., Rubash, H.E., Li, G., 2006. Erratum to "The change in length of the medial and lateral collateral ligaments during in vivo knee flexion." Knee 13, 77–82. doi:10.1016/j.knee.2004.12.012

R.A., G., R., S., J.S., T., Gurtler, R.A., Stine, R., Torg, J.S., 1987. Lachman test evaluated. Quantification of a clinical observation. Clin. Orthop. Relat. Res. No. 216, 141–150.

Ramsey, D.K., Wretenberg, P.F., 1999. Biomechanics of the knee: methodological considerations in the in vivo kinematic analysis of the tibiofemoral and patellofemoral joint. Clin. Biomech. (Bristol, Avon) 14, 595–611.

Reinbolt, J. a., Schutte, J.F., Fregly, B.J., Koh, B. Il, Haftka, R.T., George, A.D., Mitchell, K.H., 2005. Determination of patient-specific multi-joint kinematic models through two-level optimization. J. Biomech. 38, 621–626. doi:10.1016/j.jbiomech.2004.03.031

Richard, V., Camomilla, V., Cheze, L., Cappozzo, a., Dumas, R., 2012. Feasibility of incorporating a soft tissue artefact model in multi-body optimisation. Comput. Methods Biomech. Biomed. Engin. 15, 194–196. doi:10.1080/10255842.2012.713667

Richard, V., Lamberto, G., Lu, T.-W., Cappozzo, A., Dumas, R., 2016. Knee Kinematics Estimation Using Multi-Body Optimisation Embedding a Knee Joint Stiffness Matrix: A Feasibility Study. PLoS One 11, e0157010. doi:10.1371/journal.pone.0157010

Scheys, L., Desloovere, K., Spaepen, A., Suetens, P., Jonkers, I., 2011. Calculating gait kinematics using MR-based kinematic models. Gait Posture 33, 158–64. doi:10.1016/j.gaitpost.2010.11.003

Schreck, P.J., Kitabayashi, L.R., Amiel, D., Akeson, W.H., Woods, V.L., 1995. Integrin display increases in the wounded rabbit medial collateral ligament but not the wounded anterior cruciate ligament. J. Orthop. Res. 13, 174–183. doi:10.1002/jor.1100130205

Sharkey, N.A., Smith, T.S., Lundmark, D.C., 1995. Freeze clamping musculo-tendinous junctions for in vitro simulation of joint mechanics. J. Biomech. 28,

631–635. doi:10.1016/0021-9290(94)00100-I

Stagni, R., Fantozzi, S., Cappello, A., 2009. Double calibration vs. global optimisation: performance and effectiveness for clinical application. Gait Posture 29, 119–22. doi:10.1016/j.gaitpost.2008.07.008

Stagni, R., Fantozzi, S., Cappello, A., 2006. Propagation of anatomical landmark misplacement to knee kinematics: performance of single and double calibration. Gait Posture 24, 137–41. doi:10.1016/j.gaitpost.2006.08.001

Stagni, R., Fantozzi, S., Cappello, A., Leardini, A., 2005. Quantification of soft tissue artefact in motion analysis by combining 3D fluoroscopy and stereophotogrammetry: A study on two subjects. Clin. Biomech. 20, 320–329. doi:10.1016/j.clinbiomech.2004.11.012

Steele, K.M., Demers, M.S., Schwartz, M.H., Delp, S.L., 2012. Compressive tibiofemoral force during crouch gait. Gait Posture 35, 556–60. doi:10.1016/j.gaitpost.2011.11.023

Stevens, R., 2006. Gray's Anatomy for Students. Ann. R. Coll. Surg. Engl. doi:10.1308/003588406X116873b

Suderman, B.L., Vasavada, A.N., 2012. Moving muscle points provide accurate curved muscle paths in a model of the cervical spine. J. Biomech. 45, 400–404. doi:10.1016/j.jbiomech.2011.10.014

Tissakht, M., Ahmed, A.M., 1995. Tensile stress-strain characteristics of the human meniscal material. J. Biomech. 28, 411–422. doi:10.1016/0021-9290(94)00081-E

Tsai, T.-Y., Lu, T.-W., Kuo, M.-Y., Hsu, H.-C., 2009. Quantification of Three-Dimensional Movement of Skin Markers Relative To the Underlying Bones During Functional Activities. Biomed. Eng. Appl. Basis Commun. 21, 223–232. doi:10.4015/S1016237209001283

Valente, G., Pitto, L., Stagni, R., Taddei, F., 2015. Effect of lower-limb joint models on subject-specific musculoskeletal models and simulations of daily motor activities. J. Biomech. 1–8. doi:10.1016/j.jbiomech.2015.09.042

van Eck, C.F., Loopik, M., van den Bekerom, M.P., Fu, F.H., Kerkhoffs, G.M.M.J., 2013. Methods to diagnose acute anterior cruciate ligament rupture: A meta-analysis of instrumented knee laxity tests. Knee Surgery, Sport. Traumatol. Arthrosc. 21, 1989–1997. doi:10.1007/s00167-012-2246-5

Viceconti, M., Testi, D., Taddei, F., Martelli, S., Clapworthy, G.J., Van Sint Jan, S., 2006. Biomechanics modeling of the musculoskeletal apparatus: Status and key issues. Proc. IEEE 94, 725–738. doi:10.1109/JPROC.2006.871769

Walker, P., Rovick, J., Robertson, D., 1988. The effects of knee brace hinge design and placement on joint mechanics. J. Biomech.

Ward, S.R., Eng, C.M., Smallwood, L.H., Lieber, R.L., 2009. Are Current Measurements of Lower Extremity Muscle Architecture Accurate? Clin. Orthop. Relat. Res. 467, 1074–1082. doi:10.1007/s11999-008-0594-8

Wesseling, M., Derikx, L.C., de Groote, F., Bartels, W., Meyer, C., Verdonschot, N., Jonkers, I., 2015. Muscle optimization techniques impact the magnitude of

calculated hip joint contact forces. J. Orthop. Res. 33, 430–438. doi:10.1002/jor.22769

Whittle, M.W., 2007. An Introduction to Gait Analysis, Library. doi:10.1016/B978-075068883-3.50013-1

Wilson, D.R., Feikes, J.D., O'Connor, J.J., 1998. Ligaments and articular contact guide passive knee flexion. J. Biomech. 31, 1127–1136.

Woo, S.L.-Y., Abramowitch, S.D., Kilger, R., Liang, R., 2006. Biomechanics of knee ligaments: injury, healing, and repair. J. Biomech. 39, 1–20. doi:10.1016/j.jbiomech.2004.10.025

Woo, S.L., Gomez, M. a, Seguchi, Y., Endo, C.M., Akeson, W.H., 1983. Measurement of mechanical properties of ligament substance from a bone-ligament-bone preparation. J. Orthop. Res. 1, 22–9. doi:10.1002/jor.1100010104

Yagi, M., Wong, E.K., Kanamori, A., Debski, R.E., Fu, F.H., Woo, S.L.-Y., 2002. Biomechanical analysis of an anatomic anterior cruciate ligament reconstruction. Am. J. Sports Med. 30, 660–666.

Yamaguchi, G.T., Zajac, F.E., 1989. A planar model of the knee joint to characterize the knee extensor mechanism. J. Biomech. 22, 1–10. doi:10.1016/0021-9290(89)90179-6

Zajac, F., 1988. Muscle and tendon: properties, models, scaling, and application to biomechanics and motor control. Crit. Rev. Biomed. Eng.

Zantop, T., Kubo, S., Petersen, W., Musahl, V., Fu, F.H., 2007. Current techniques in anatomic anterior cruciate ligament reconstruction. Arthroscopy. doi:10.1016/j.arthro.2007.04.009

CHAPTER 3

Effects of the soft tissue artefact on current musculoskeletal models

In light of what discussed in Chapter 2, this chapter of the thesis investigates how the effects of the STA propagate to the estimates of MSKs. In fact, the STA included in the input data from studies conducted using stereophotogrammetry affects the model estimates in an unclear way, limiting the ability to draw meaningful conclusions on a specific population. For example, the variability of the ankle dorsi-flexion during normal walking of a cohort of ten healthy subjects could be confused with the coordinate variation only caused by the STA. This can generate issues when interpreting the results. The current chapter aims to quantify these aspects and overcome this issue. This was performed by implementing a realistic distribution of a location-dependent STA and assessing, using a Monte Carlo analysis, the impact on the joint angles, joint moments, muscle and joint contact forces of three publicly-available and widely adopted MSMs in OpenSim.

A considerable part of the material presented in this section is based on:

Lamberto, G., Martelli, S., Cappozzo, A., Mazzà, C., (2016). "To what extent is joint and muscle mechanics predicted by MSMs sensitive to soft tissue artefacts?" *J. Biomech.* , 1–9. doi:10.1016/j.jbiomech.2016.07.042.

Written permission has been obtained from all the co-authors.

Author's contribution for this chapter was related to the development of the STA model, running simulations in OpenSim, post-processing the results in MATLAB and manuscript preparation.

3.1. Introduction

As detailed in the previous Chapter, stereophotogrammetric recordings of skin-mounted marker trajectories and GRFs are fed to MSMs with the aim of estimating joint angles, intersegmental loads, and muscle and joint contact forces during movement (Anderson et al., 2007; Delp et al., 2007). Unfortunately, the skin-mounted markers move over the underlying bone generating the STA, which makes the estimation of the instantaneous skeletal pose awkward (Leardini et al., 2005). Normally, MSMs cope with this problem by using the MBO method which embeds a least squares approach and articular constraints (Delp et al., 2007; Lu and O'Connor, 1999). The residual artefact, however, might still propagate to MSM estimates, with an effect that is still unclear, especially as far as muscle and joint forces are concerned.

Recent studies attempted to address the aforementioned problem by quantifying the sensitivity of MSMs estimates to the STA. El Habachi et al., (2015), using a global probabilistic approach and, contrary to the available evidence (Leardini et al., 2005; Peters et al., 2010), modelling the STA with the same statistics for all markers independently from their location on the body, showed that the STA may cause joint angle variations of up to 36°. The variations of muscle and joint forces were not investigated. Myers et al., (2015) investigated the effects of the propagation of the STA for the MSM proposed by Delp et al. (1990) through a Monte Carlo analysis and showed that the STA can induce variations in the joint angles that are 1.8 times higher than the uncertainties due to anatomical landmark identification. Myers et al., (2015) also investigated the variations induced by the STA on the joint moments, and found that these were 2.3 to 4 times higher than those induced by improper positioning of skin markers on the anatomical landmarks and uncertainties in estimating the inertial parameters (i.e., mass, moment of inertia and centre of mass). The same authors also reported an impact on muscle forces, with variations due to the STA that, for gluteus medius and medial gastrocnemius, reached 50%. These effects, however, were about half of those generated by the inaccuracies affecting musculo-tendon parameters such as pennation angle, maximum isometric force, and tendon slack length. In this study, the STA model embedded marker-specific

parameters which were also gait-phase dependent. However, STAs were constrained to have a maximal amplitude of 15 mm, in contrast with the values reported in the literature, for example the 40 mm observed at the lateral epicondyle of the thigh (Leardini et al., 2005; Peters et al., 2010). Finally, the effects on joint contact forces were not investigated.

It therefore appears that the available information is limited to particular types of MSMs, not all of which are publicly available, to a specific subset of model outputs, and to simplified STA designs. Thus, a conclusive quantification of the sensitivity of the estimates of different MSMs to a realistic and comprehensive STA representation is still lacking.

The aim of the present study was thus to investigate the sensitivity of joint angles, joint moments, and muscle and joint contact forces to a STA consistent with the best knowledge available in the literature using three different open-source MSMs and relevant tools, which are commonly used in research contexts (Arnold et al., 2010; Delp et al., 1990; Modenese et al., 2011). A probabilistic approach and published STA models were used to design a realistic set of artefact-affected marker trajectories and, through a Monte Carlo simulation, assess the statistical impact of the artefact on the outputs of the selected MSMs when studying the gait of a representative subject.

3.1. Material and methods

A single healthy participant (male, age: 28 years, stature: 1.90 m, mass: 82 kg) was enrolled in the study after providing informed consent. Ethical approval for the study was obtained from the University Research Ethics Committee at the University of Sheffield.

Overall, twenty-eight 8mm-diameter reflective skin-markers were attached using double-sided tape to the feet (8), shanks (8), thighs (8), and pelvis (4). They were placed on the following anatomical landmarks (anatomical markers): anterior and posterior superior iliac spines (ASIS and PSIS), lateral femoral condyle (LE), tibial tuberosity (TT), lateral malleolus (LM), posterior distal aspect of the heel (HEE), forefoot (midpoint between second and third metatarsal heads; FF), heads of first

and fifth metatarsals (MT1 and MT5). Furthermore, additional markers were placed in the following positions (technical markers): laterally and equidistant along the length of the thigh (TH1, TH2 and TH3), and anterior and lateral to the mid-shank (SH1 and SH2). Marker trajectories were recorded using an 8-camera stereophotogrammetric system (Vicon MX, Vicon Motion Systems Ltd, Oxford, UK, 100 frames per second, resolution in pixels per camera: 1266 H x 1024 V) with synchronised measurement of the GRFs obtained using two strain-gauge force plates (Bertec Corp., Columbus, OH, USA, 1,000 samples per second). Motion tasks included a static standing posture with each foot on the two separate force platforms and five acquisitions of level walking at self-selected speed. Signals from sEMG were acquired following SENIAM protocol for the listed muscles (Hermens et al., 2000): medial gastrocnemius, biceps femoris (long head), tibialis anterior and vastus medialis.

3.1.1. Musculoskeletal models

Three lower limb MSMs (Figure 3.1), named ALLM, G2392, and LLLM respectively were downloaded from www.simtk.org. G2392 and ALLM were chosen for being widely adopted and cited. LLLM was chosen as being the one that most differed from them in terms of bone geometries, joint constraints, muscular attachment sites and lines-of-action, and number of muscle bundles, and for being a single lower limb model (Table 3.1). This last characteristic influences the model estimates because a MBO is employed.

Model name (Acronym)	References	Segments	Joints	DoFs	Ipsilateral muscle bundles
Lower Limb 2010 (ALLM)	Arnold et al., 2010; Ward et al., 2009	12	10	19	45
Gait 2392 (G2392)	Delp et al., 1990; Yamaguchi and Zajac, 1989	8	8	19	43
London Lower Limb* (LLLM)	Klein Horsman et al., 2007; Modenese et al., 2011	6	6	12	163

* Single lower limb model

Table 3.1 - MSMs used to perform the sensitivity analysis.

Each generic MSM, which includes the above-mentioned anatomical markers, was scaled to match the volunteer's anthropometry estimated using the ratio between the lengths of the model segments and those computed from the experimental data. The pelvis was scaled using the distance between the right and left anterior superior iliac spines, and the distance between the mid-points of the anterior and posterior superior iliac spines. The joint centres were located using the marker positions as acquired in a static trial and the Harrington regression equations (Harrington et al., 2007) for the hip joint, the mid-point between the femoral epicondyles for the knee joint, and the mid-point between the malleoli for the ankle joint. The size of the thighs, shanks and feet was scaled using the distances between the hip and knee centres, knee and ankle centres, and heel and second metatarsal head markers, respectively. The technical markers were finally embedded in the scaled MSMs by registering, using the MBO method, the anatomical markers of each model with the corresponding anatomical markers placed on the volunteer as recorded during the static trial. The segment masses in the model were uniformly scaled to match the total body mass of the participant.

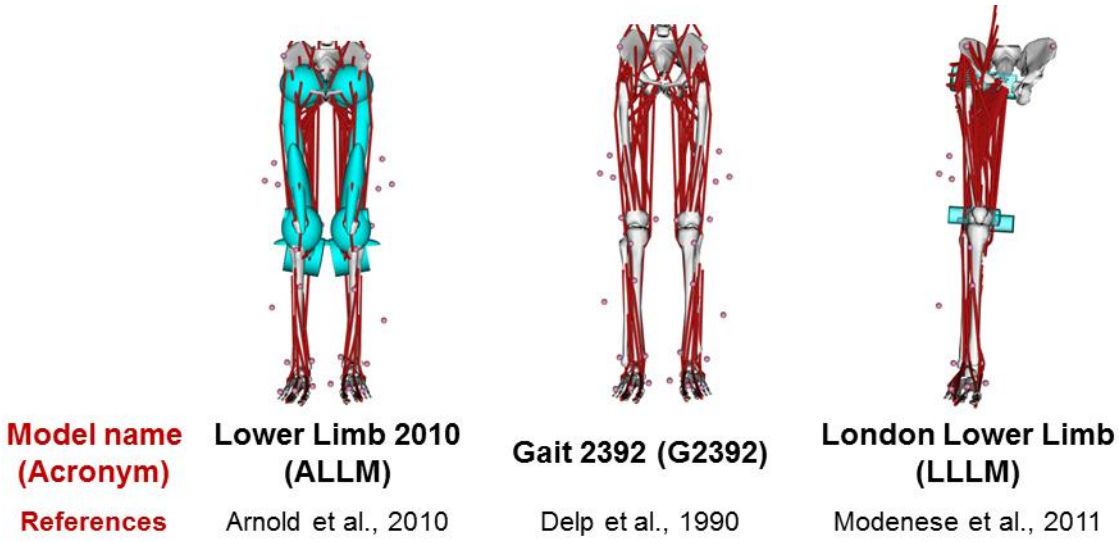

Figure 3.1 – MSMs analysed in this chapter.

The maximal isometric forces of the muscles represented in the MSMs, which are parameters needed to solve the myoskeletal indeterminacy problem (Viceconti et al., 2006), were uniformly scaled following criteria described in previous studies (Arnold et al., 2013; Laughlin et al., 2011; Mokhtarzadeh et al., 2014). In particular, a scaling factor equal to the ratio between the volunteer lower limb mass, estimated as a percentage of the total mass (De Leva, 1996), and the corresponding generic MSM lower limb mass was used.

However, when using ALLM and LLLM during gait, some muscles resulted to reach the maximal force values obtained as illustrated above (most of the muscles for ALLM, whereas mainly the medial gastrocnemius for LLLM). Given the nature of walking as a sub-maximal motor act, this is an unlikely outcome, so the affected maximal forces defined in the MSMs, were increased by up to a factor of three, confident in the fact that this would not significantly influence the sensitivity analysis of the present study.

One gait cycle was simulated for the participant's dominant lower limb using the standard OpenSim pipeline (Figure 3.2). First run was an "*inverse kinematics*" analysis which uses a MBO algorithm to determine the joint angles that best fit the experimental trajectories collected during the walking trial (Lu and O'Connor, 1999). The "*inverse dynamics*" tool subsequently estimated internal joint moments, using as an input the previously computed joint angles and the measured external

GRFs. The muscle forces were then calculated using the "*static optimisation"* function, solving muscle redundancy by minimising the sum of squared muscle activations and neglecting the force-length-velocity relationships of muscles (Anderson and Pandy, 2001). Finally, joint contact forces were calculated using the "*joint reaction analysis*" tool by recursively solving segment equilibrium, starting from the most distal and moving proximally (Steele et al., 2012). Despite the tool can be used for all the MSMs to extract the results, estimation of the knee contact force was only performed for G2392. This was due to the fact that in both ALLM and LLLM the pose of the patella is defined as a function of the tibiofemoral joint flexion-extension angle, which has been proven to lead to inaccurate estimates of the overall tibiofemoral contact force when computed using the available OpenSim tools (Koehle and Hull, 2008; Wagner et al., 2013). Since implementing *ad-hoc* tools to perform this calculation was beyond the scope of this study, relevant data will not be reported for these models. All analyses were conducted using OpenSim 3.1 (Delp et al., 2007) and MATLAB scripts (The MathWorks Inc., USA, version 2015a), including the publicly-available libraries (Barre and Armand, 2014; Mantoan et al., 2015).

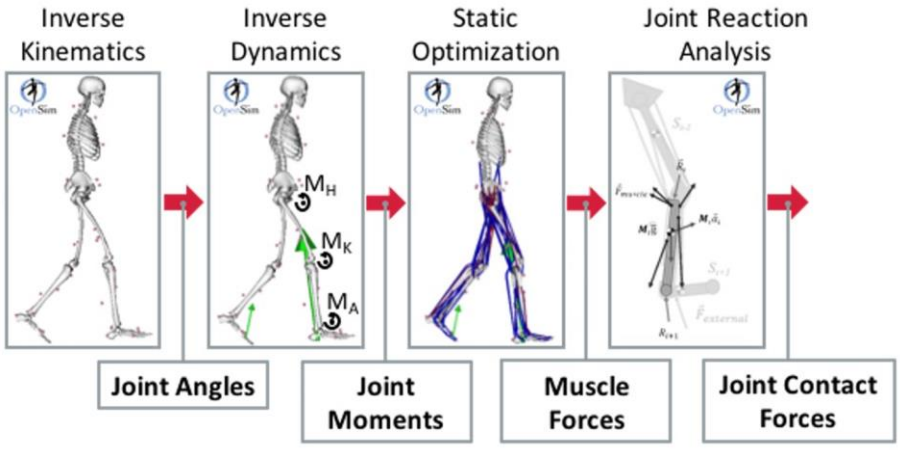

Figure 3.2 – Standard OpenSim inverse pipeline used in this part of the thesis (Delp et al., 2007).

The quality of the joint angles and moments and of the muscle and joint contact forces was assessed as suggested in (Hicks et al., 2015). In particular, despite some differences due to the different joint coordinate system definitions, the joint angles and moments showed good agreement with the literature (Kadaba et al., 1989), suggesting that the chosen subject can be considered as representative of the healthy

adult population. The muscle activations and forces were evaluated by visually comparing the recorded sEMG signals (Martelli et al., 2015) with the activation timing of MSM muscles (Figure 3.3). In addition, the hip, knee and ankle residuals were all below 0.06 Nm and hence far less than 1% of the COM height times the magnitude of the measured net external force, which is the limit suggested in (Hicks et al., 2015). The joint contact forces were compared to recent literature data and exhibited coherent patterns (Bergmann et al., 2001; Heller et al., 2001; Martelli et al., 2014; Modenese and Phillips, 2012; Valente et al., 2014; Wesseling et al., 2015), with slightly higher forces observed at the hip, likely due to the higher measured GRFs.

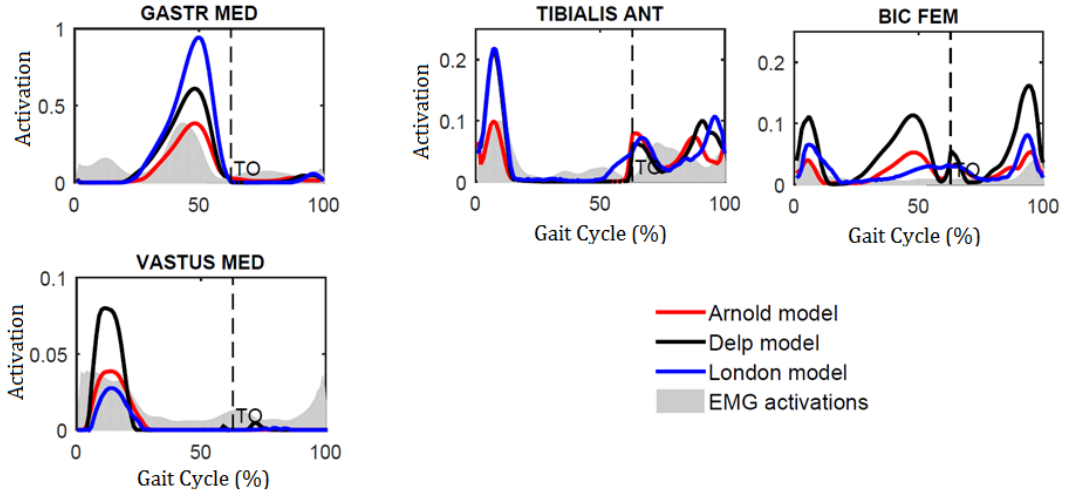

Figure 3.3- Agreement between measured sEMG and estimated muscle activation (0: muscle inactive; 1: muscle fully activated). GASR MED: medial gastrocnemius, BIC FEM: biceps femoris (long head), TIBIALIS ANT: tibialis anterior and VASTUS MED: vastus medialis.

3.1.2. Probabilistic analysis, baseline dataset and probabilistic design of the parametric STA

3.1.2.1. Background on probabilistic analysis

A probabilistic analysis, based on the Monte Carlo method, was used to evaluate the impact of the STA on the three selected MSMs. Probabilistic analyses have been extensively used over the last decades in the biomechanical and orthopaedic fields to account for uncertainties in the input data as well as in model parameters. The review of Laz and Browne, (2010) includes several examples and useful

explanations for the interested reader. Factors like subject geometry, motion data, and material properties can all have an influence on the outcomes. Monte Carlo simulation, the most commonly applied probabilistic method in biomechanics, involves the generation of random values for each variable according to its specific distribution and then estimating the performance and the effects of each case through repeated trials. This method typically requires many thousands of trials to achieve meaningful conclusions (Haldar and Mahadevan, 2000).

An adaption of the traditional Monte Carlo approach is represented by the implementation of the Latin Hypercube Sampling (LHS) method, which still requires a convergence analysis to assess result independence from the chosen sample size. Using LHS increases the efficiency of the probabilistic analysis because it allows for controlling the sampling in a predetermined way. LHS samples the possible design space by dividing it into subspaces characterised by an equal probability. This guarantees an even coverage of the design space and significantly reducing the overall sample size (Laz and Browne, 2010). For these reasons as well as the adoption in previous similar literature (Bosmans et al., 2015; El Habachi et al., 2015; Martelli et al., 2014), a LHS-adapted Monte Carlo method has been used in this study.

3.1.2.2. Baseline dataset

For each MSM, a set of marker trajectories was synthetically created as a baseline dataset for this sensitivity analysis (step one of Figure 3.4). This was achieved by running the "*point kinematics*" tool which, given the calculated joint angles, provides the global coordinates of the markers that are rigidly attached to the model body segments for each instant in time. As such, these coordinates are time-invariant when observed from their respective anatomical frame.

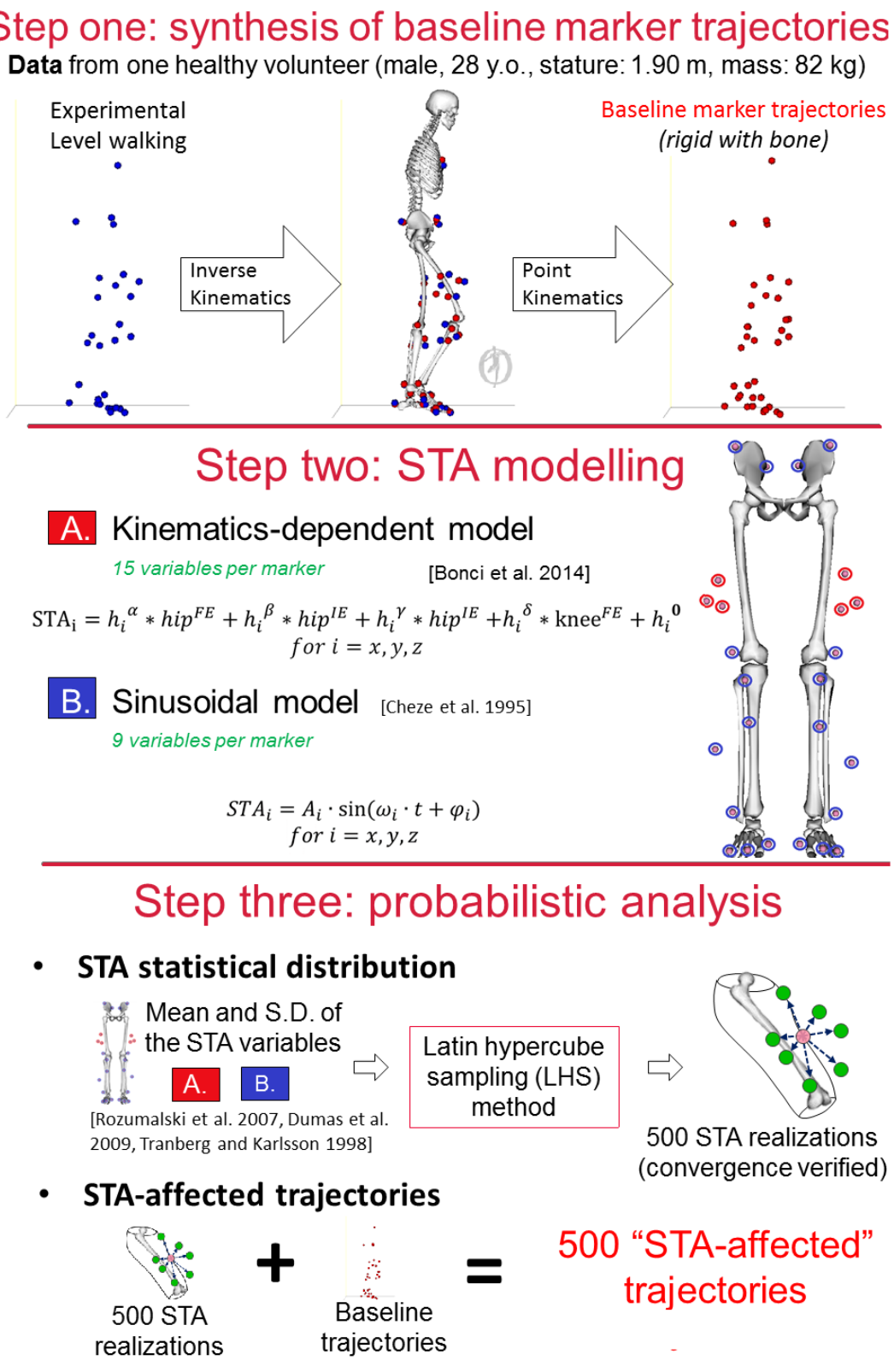

Figure 3.4 – Three steps for preparation and run of the probabilistic analysis.

3.1.2.3. Parametric STA modelling

The STAs for the feet, shanks, lateral femoral epicondyles and pelvis markers were modelled as sinusoidal functions of time described by nine parameters representing amplitude, frequency and phase of each marker's spatial coordinates (Chèze et al., 1995). Their statistical representation was obtained using their mean range ± three standard deviations. The pelvis marker amplitudes were varied non-uniformly for the three spatial coordinates using the findings reported by Rozumalski et al. (2007). The shank STA amplitudes were computed using the values suggested by Dumas and Cheze (2009) with the foot amplitudes similarly determined using the values reported by Tranberg and Karlsson (1998).

The STAs for the lateral-thigh markers were modelled as a linear function of the three hip angular rotations and the knee flexion angle (Bonci et al., 2014). Each coordinate of these STAs was described by four coefficients, which were used to multiply the reference hip flexion, abduction, rotation and knee flexion angles respectively, and by one constant (h^0, Table 3.2). The mean value for the statistical distribution of the four coefficients was set to be equal to the values of the *ex vivo* dataset of Subject 1 reported in Bonci et al. (2014). The standard deviation was computed using the ratio between the root mean square values of the STA components of the same subject and the average value of the corresponding joint angles over the gait cycle. The mean and standard deviations for h^0 were set using the standing joint angle statistics reported in Hemmerich et al. (2006). As a result of the above calculations (step two of Figure 3.4), 22 sinusoidal STAs and 6 kinematics-dependent STAs were defined for G2392 and ALLM, resulting in a total of 324 stochastic input variables for the Monte Carlo analysis. For the single-leg LLLM, only 13 sinusoidal STAs and 3 kinematics-dependent STAs were used, resulting in 162 input variables for the statistical analysis.

3.1.2.4. Probabilistic analysis

A LHS method was then used to generate 500 samples for each of the stochastic variables, reflecting the mean and standard deviation of each variable (step three of Figure 3.4). The distributions generated were then checked for normality using the

Lilliefors test (Lilliefors, 1967). This process produced 500 STA realisations in the local anatomical frames. A coordinate transformation to the laboratory frame was then performed, in order to sum the STA realisations to the reference marker trajectories and create the artefact-affected trajectories. Finally, the artefact-affected trajectories were then iteratively fed to the corresponding MSM. Joint angles, joint moments and muscle and joint contact forces were estimated using the generated artefact-affected trajectories while keeping the same measured GRFs. Joint moments were normalised to the volunteer's mass and muscle and contact forces were expressed as multiples of body weight (BW).

The appropriateness of the sample size generated by LHS was assessed via a convergence analysis. In fact, the outcome of the Monte Carlo needs to be independent of the number of samples to ensure a correct interpretation and a trustful generalisation of the study results (Baldwin et al., 2009). To this purpose, the changes of the entire set of generated input and output variable distributions were monitored. Starting from considering one sample and by progressively increasing the number to 500, the change of each variable was checked. When the sample size was higher than 300, the observed changes were found to stabilise. Choosing 500 samples allowed all the variables to be below a convergence threshold (Martelli et al., 2015). More details and a clarifying example on the convergence analysis are provided in Figure 3.5. No discrepancies were observed among the investigated MSMs for what concerns this analysis.

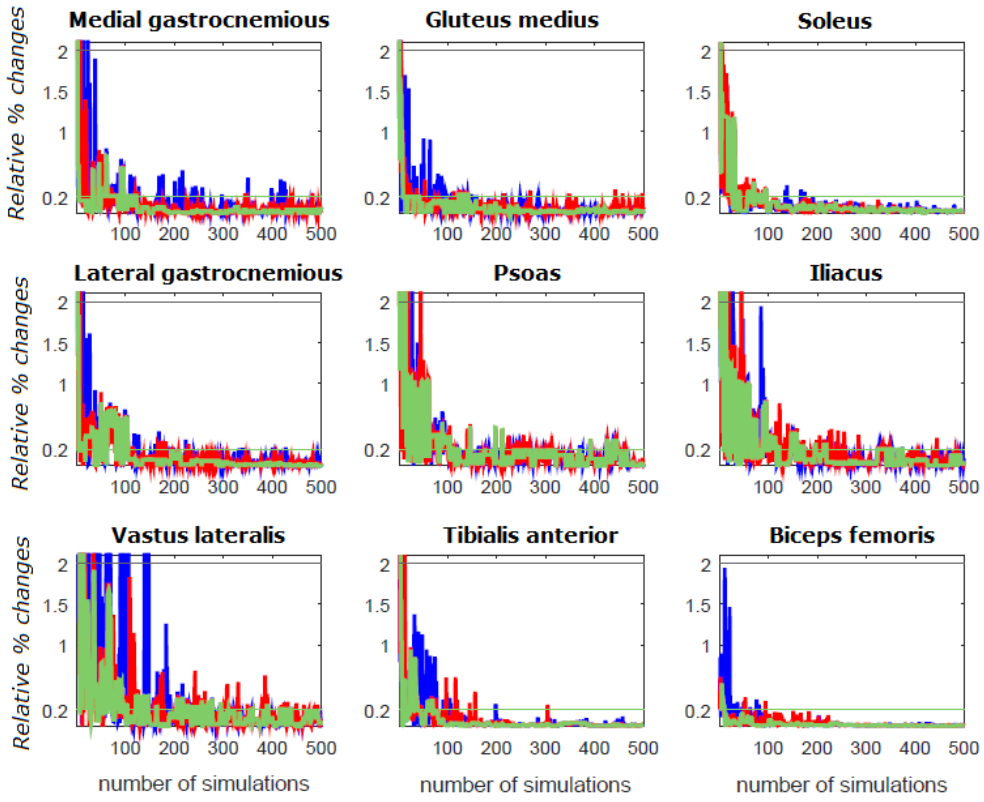

Figure 3.5 - Example of convergence analysis results performed for nine different muscle force estimated by the G2392. The same analysis was also performed on all the input variables as well as ALLM and LLLM estimates. The amount of 500 simulations was enough to make sure that the resulting increments were below the corresponding limits, set at 0.2% for the 50th percentile and at 2% for both the percentile ranges of 15th-50th and 50th - 85th (Martelli et al., 2015).

STA model	Marker acronym	Segment	Equations	Parameters / Range of parameters	Reference papers
Sinusoidal	RASIS LASIS RPSIS LPSIS	Pelvis	$STA_X = A_X \cdot \sin(\omega \cdot t + \varphi)$ $STA_Y = A_Y \cdot \sin(\omega \cdot t + \varphi)$ $STA_Z = A_Z \cdot \sin(\omega \cdot t + \varphi)$	$A_x^m = 17, A_y^m = 20, A_z^m = 26$, $A_x^{95IC} = 3, A_y^{95IC} = 8, A_z^{95IC} = 6$, $\omega \leq 25\frac{rad}{s}$, $\varphi \leq 2\pi$ $A_x^m = 14, A_y^m = 8, A_z^m = 12$, $A_x^{95IC} = 2, A_y^{95IC} = 2, A_z^{95IC} = 1$, $\omega \leq 25\frac{rad}{s}$, $\varphi \leq 2\pi$	(Chèze et al., 1995; Rozumalski et al., 2007)
Kinematics-dependent	RTH1* RTH2* RTH3*	Right thigh	$\mathrm{STA}_{\mathrm{vector(i)}} = \boldsymbol{h^{\alpha}} * hip^{FE}$ $+\boldsymbol{h^{\beta}} * \boldsymbol{hip}^{IE} + \boldsymbol{h^{\gamma}} * \boldsymbol{hip}^{IE}$ $+\boldsymbol{h^{\delta}} * \mathrm{knee}^{FE} + \boldsymbol{h^{0}}$, $for\ i = x, y, z$	h_{RTHI}^{α}, h_{RTHI}^{β}, h_{RTHI}^{γ}, h_{RTHI}^{δ}, h_{RTHI}^{0} h_{RTH2}^{α}, h_{RTH2}^{β}, h_{RTH2}^{γ}, h_{RTH2}^{δ}, h_{RTH2}^{0} h_{RTH3}^{α}, h_{RTH3}^{β}, h_{RTH3}^{γ}, h_{RTH3}^{δ}, h_{RTH3}^{0}	(Bonci et al., 2014)
Sinusoidal	RLE*	Right thigh	$STA_X = A \cdot \sin(\omega \cdot t + \varphi)$ $STA_Y = A \cdot \sin(\omega \cdot t + \varphi)$ $STA_Z = A \cdot \sin(\omega \cdot t + \varphi)$	$A \leq 30,\ \omega \leq 25\frac{rad}{s},\ \varphi \leq 2\pi$	(Chèze et al., 1995; Dumas and Cheze, 2009)
	RSH1* RSH2* RTT*	Right shank		$A \leq 15,\ \omega \leq 25\frac{rad}{s},\ \varphi \leq 2\pi$	
	RLM*	Right shank		$A \leq 4.3,\ \omega \leq 25\frac{rad}{s},\ \varphi \leq 2\pi$	(Chèze et al., 1995; Tranberg and Karlsson, 1998)
	RHEE*	Right foot		$A \leq 2.56,\ \omega \leq 25\frac{rad}{s},\ \varphi \leq 2\pi$	
	RFF* RMT1* RMT5*	Right foot		$A \leq 1.81,\ \omega \leq 25\frac{rad}{s},\ \varphi \leq 2\pi$	

(*): Model markers repeated for the left limb for G2392 and ALLM.

Table 3.2 – STA design per marker. The first letter in the marker code indicates the body side (R = right, L = left).

3.1.3. Data Analysis

The distribution of the STA realisations of the pelvis and right lower limb was calculated and compared with published STA measurements excluding those used to generate the artefact-affected trajectories (Akbarshahi et al., 2010; Cappozzo et al., 1996; Hara et al., 2014; Maslen and Ackland, 1994; Stagni et al., 2005; Tsai et al., 2009; Wrbaskić and Dowling, 2007).

The sensitivity of each of the three MSMs was determined by calculating the 5^{th}, 50^{th} and 95^{th} percentiles of their output for the right lower limb over the entire gait cycle. The difference between the 95^{th} and 5^{th} percentile variation of each output of interest (hereinafter referred to as the variation interval), was described using maximum, mean and standard deviation values. Relative variations were also quantified by calculating the ratio between the mean variation interval and the range of the 50^{th} percentile.

3.2. Results

The marker-depended STA distribution showed good agreement to published STA measurements (Table 3.3). The STA for the markers in the thigh segment exhibited the largest range of values with mean and standard deviation reaching 39.7 ± 17.6 mm (peak STA value: 46.6 ± 21.7 mm found for the RTH2 marker). The mean STA for the markers on the pelvis was 28.7 ± 6.7 mm (peak STA value: 36.9 ± 8.2 mm found for the ASIS markers), was for those on the shank 11.9 ± 3.8 mm (peak STA value: 14.5 ± 4.6 mm found for the RSH1 marker) and was for those on the foot was 1.9 ± 0.6mm (peak STA value: 2.5 ± 0.8 mm found for the RHEE marker).

Marker/Segment	Mean ± Std. (mm)	Peak ± Std. (mm)
RASIS	26.3 ± 6.9	36.9 ± 8.2
LASIS	26.2 ± 6.9	36.9 ± 8.2
RPSIS	14.3 ± 4.0	20.4 ± 5.2
LPSIS	14.5 ± 4.0	20.5 ± 5.2
Pelvis	20.3 ± 5.5	28.7 ±6.7
RTH1	26.0 ± 11.6	44.4 ± 21.7
RTH2	26.1 ± 11.9	46.6 ± 21.7
RTH3	20.4 ± 10.1	38.6 ± 18.3
RLE	20.3 ± 5.9	28.9 ± 9.0
Thigh	23.2 ± 9.9	39.7 ± 17.6
RSH1	10.1 ± 2.9	14.5 ± 4.6
RSH2	10.1 ± 2.9	14.4 ± 4.6
RTT	10.2 ± 2.9	14.5 ± 4.5
RLM	2.9 ± 0.8	4.1 ± 1.4
Shank	8.3 ± 2.4	11.9 ± 3.8
RHEE	1.7 ± 0.5	2.5 ± 0.8
RFF	1.2 ± 0.4	1.7 ± 0.6
RMT1	1.2 ± 0.3	1.7 ± 0.6
RMT5	1.2 ± 0.4	1.8 ± 0.5
Foot	1.4 ± 0.4	1.9 ± 0.6

Table 3.3 - Mean (± standard deviation) and peak (± standard deviation) STA values from the 500 samples, with highest values per segment highlighted.

The shape, magnitude and timing of the joint angle and moment time histories were not significantly affected throughout the entire gait cycle (Figure 3.6 to Figure 3.11). Minor magnitude variations across the different gait phases were observed in the muscle and joint forces. These variations were consistently found in the estimates of the three models, with the highest percentage values occurring for the peak values of the quantitative involved (Figure 3.10 and Figure 3.11).

The time histories of the muscle forces estimated using the three MSMs showed similar patterns but different magnitudes. The largest difference was found for the soleus and the gastrocnemius muscles, where the peak values of the 95th percentile were 3.1 BW and 2.1 BW as calculated by the ALLM, 3.3 BW and 1.5 BW as calculated by the G2392 and 1.4 BW and 3.2 BW as calculated by the LLLM, respectively. The STA effect on the estimation of the joint reaction forces was joint-dependent, showing the highest effect at the hip and a reduced impact at the ankle. This was consistent across the three MSMs analysed. The maximum force variation intervals at the hip were 1.8 BW, 1.5 BW and 1.6 BW for ALLM, G2392 and

LLLM, respectively, while the maximum knee force variation was 0.9 BW for G2392 and the maximum ankle force variations were of about 0.6 BW for all three MSMs (Figure 3.12).

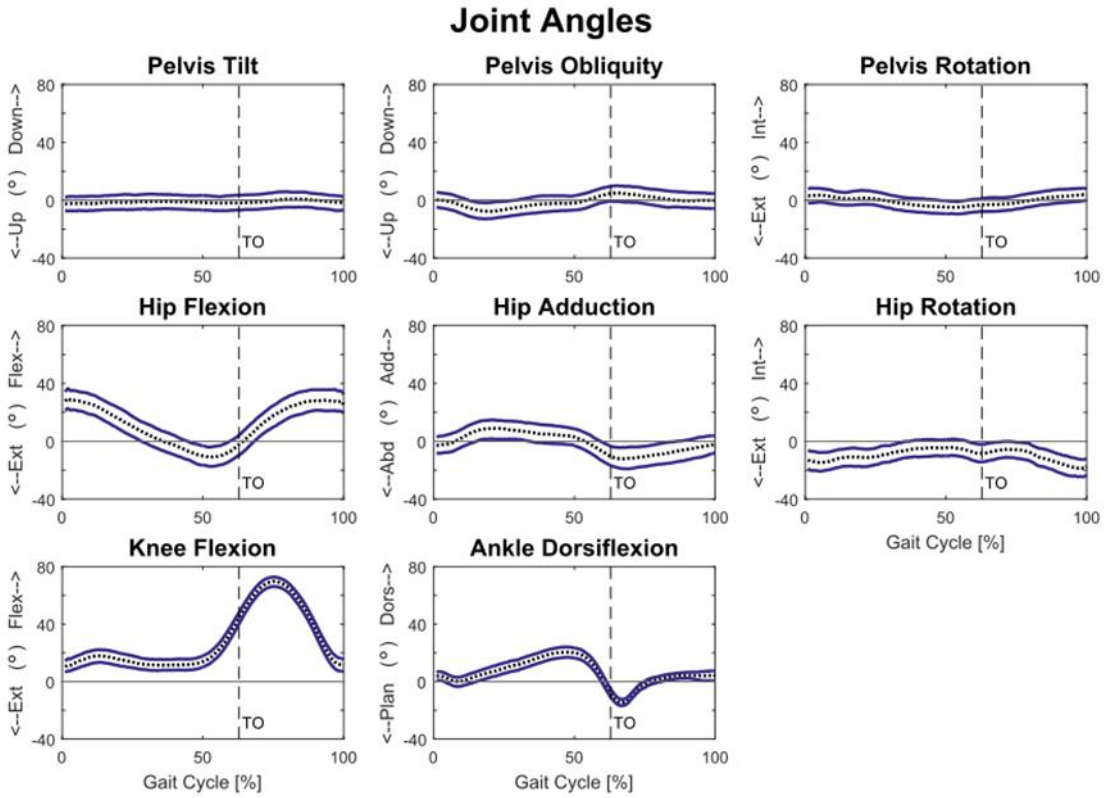

Figure 3.6 - Joint angle variations for the ALLM across the gait cycle. The 5th and 95th percentiles are shown in solid lines, while dotted lines are for the 50th percentile. A vertical dashed line specifies the right foot toe-off during the gait cycle.

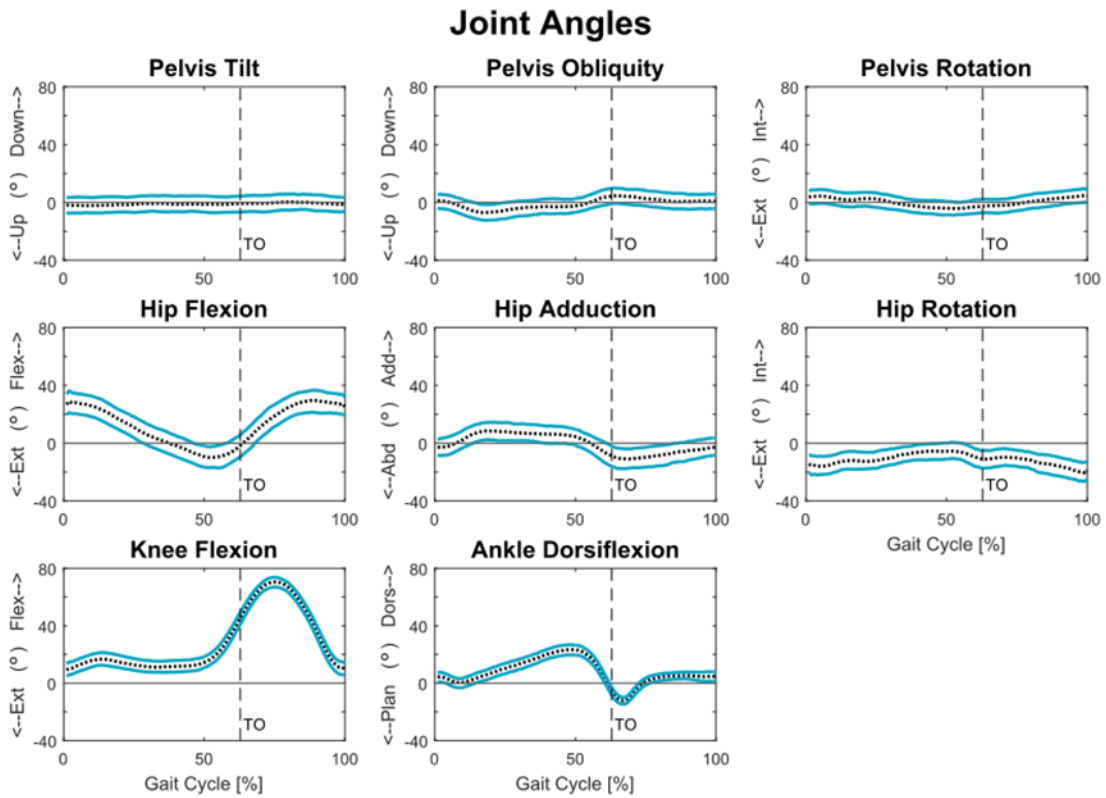

Figure 3.7 – Joint angle variations for the G2392 across the gait cycle. The 5th and 95th percentiles are shown in solid lines, while dotted lines are for the 50th percentile. A vertical dashed line specifies the right foot toe-off during the gait cycle.

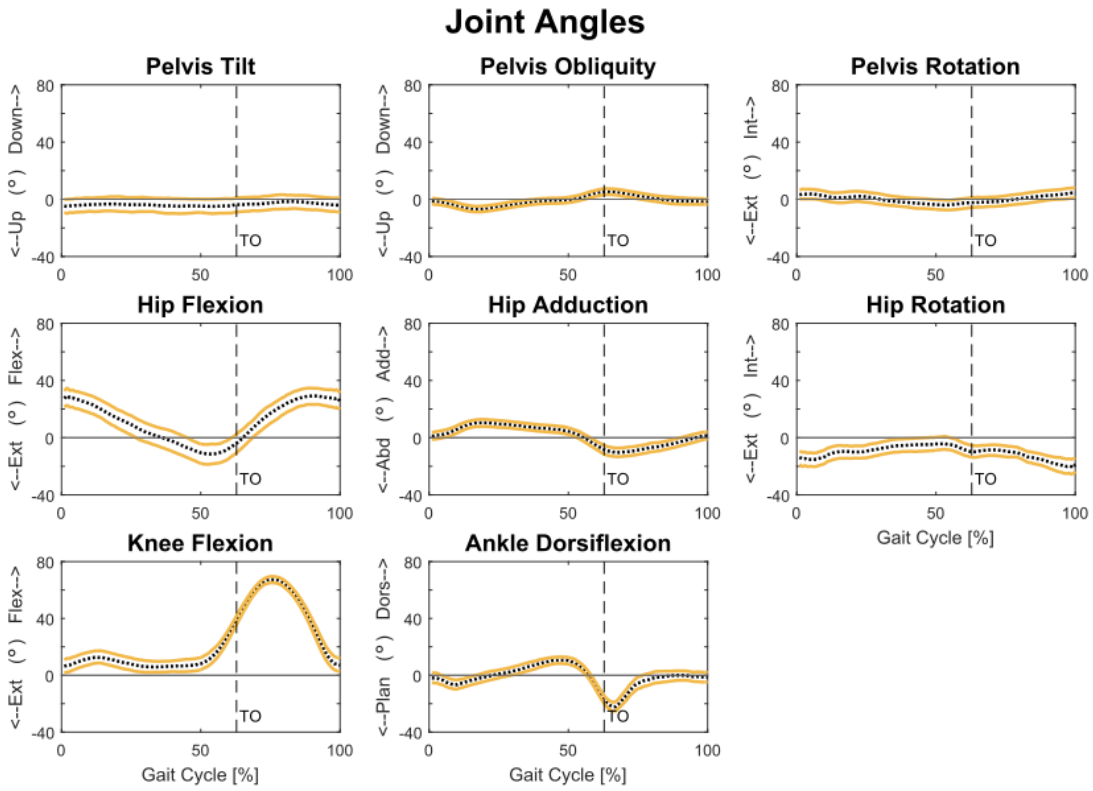

Figure 3.8 - Joint angle variations for the LLLM across the gait cycle. The 5th and 95th percentiles are shown in solid lines, while dotted lines are for the 50th percentile. A vertical dashed line specifies the right foot toe-off during the gait cycle.

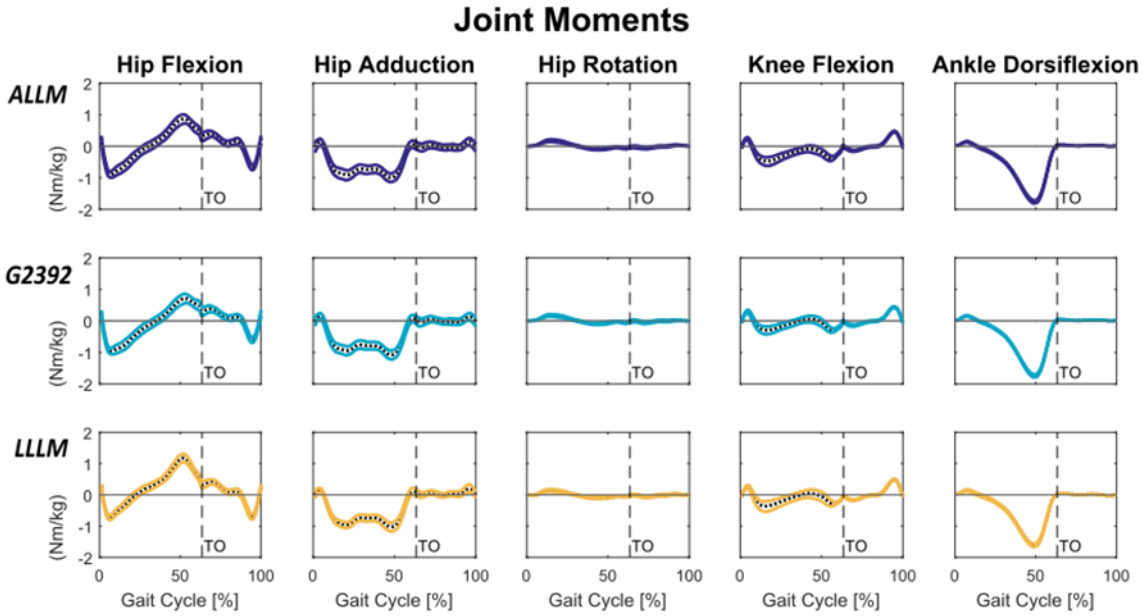

Figure 3.9 – Joint moment variations for the observed MSMs across the gait cycle. The top, middle and lower panels contain the output variations for ALLM, G2392 and LLLM, respectively.

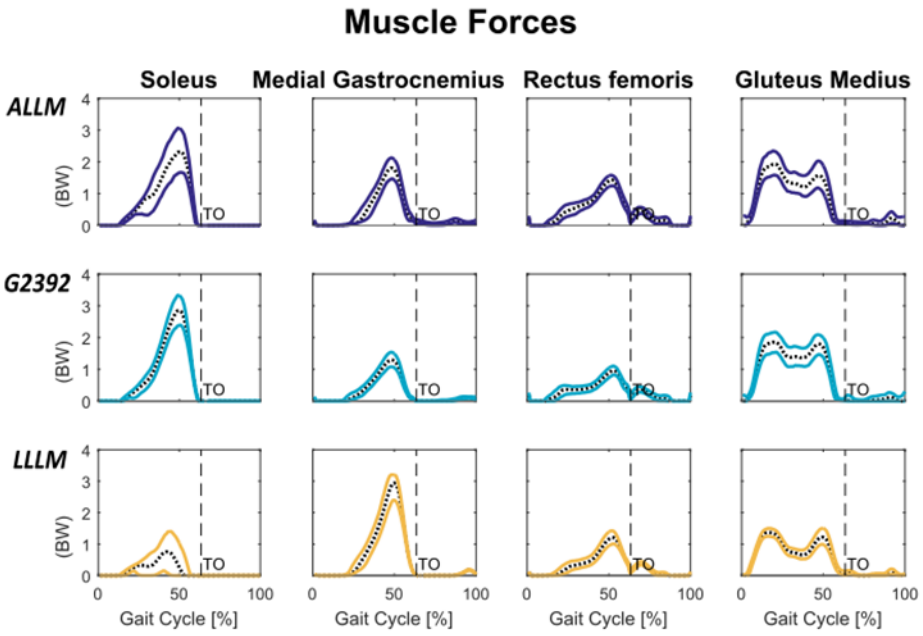

Figure 3.10 - Muscle force variations for the observed MSMs across the gait cycle. The top, middle and lower panels contain the output variations for ALLM, G2392 and LLLM, respectively.

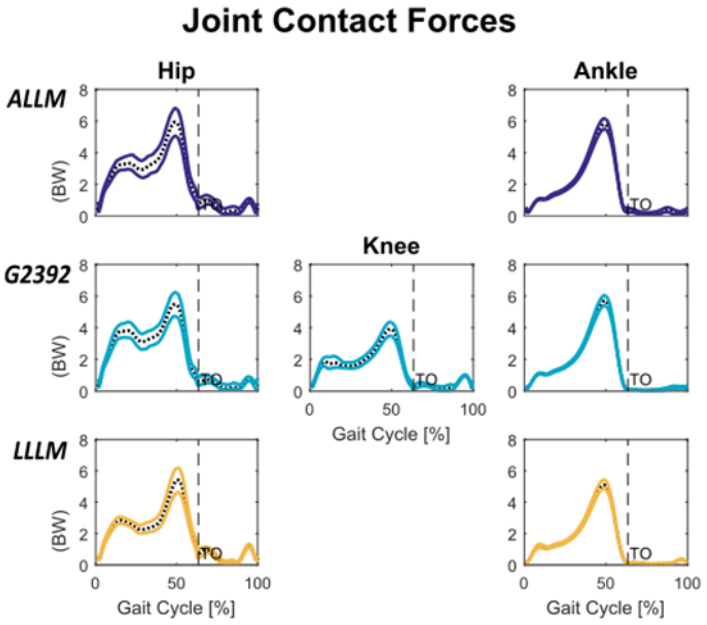

Figure 3.11 - Joint contact force variations for the observed MSMs across the gait cycle. The top, middle and lower panels contain the output variations for ALLM, G2392 and LLLM, respectively.

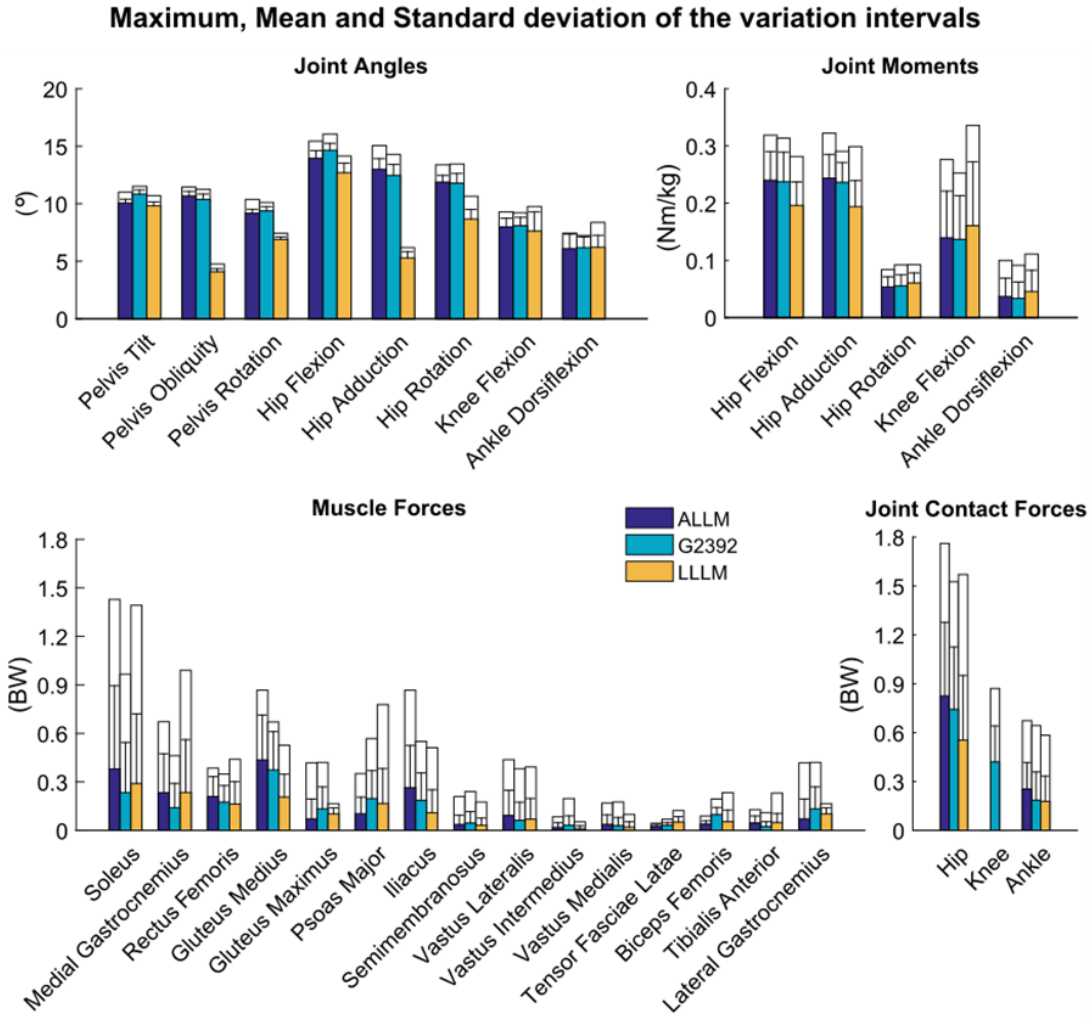

Figure 3.12 - Output variation intervals. Maximum, mean and standard deviation are displayed for each range, each variable and each MSM. Solid filled bars show the mean values while the corresponding standard deviations and maximum values are presented upward as error bars and solid bounding boxes, respectively.

For the pelvis and hip angles, relative variations higher than 30% occurred consistently for the three MSMs, whereas values below 20% were observed for both the knee and ankle angles. The relative variations found for the joint moments and muscle forces ranged between 5% and 25% and were to a great extent consistent across MSMs. For LLLM only, slightly higher values were found for the soleus (38%), the gluteus maximus (31%) and the lateral gastrocnemius (31%). Finally, relative variations ranging from 5% to 15% were consistently found across the three MSMs for the joint contact forces.

3.3. Discussion

The aim of this study was to quantify the sensitivity of three different MSMs to the STA affecting their input positional measurements. This was achieved through a probabilistic analysis, which overall showed that the output variations increased from the ankle to the hip, while the shape and magnitude of the outputs of interest were mostly preserved throughout the entire gait cycle. The observed effects were similar across MSMs.

The STA realisations generated in this study were found to be in line with measured STAs reported in the literature, excluding those used for STA model calibration. The magnitude of the STA estimated for the pelvis markers during walking was on average 20 mm (Table 3.3) which, as expected, was higher than the 17 mm found by Hara et al., (2014) for multiple static standing postures. STA magnitude was higher at the thigh than at the shank (Table 3.3), as per in previous studies (Akbarshahi et al., 2010; Stagni et al., 2005; Tsai et al., 2009). The average thigh STA peak-to-peak value was higher than those previously reported (23 mm vs 9 mm in Akbarshahi et al., 2010, and 14 mm in Tsai et al., 2009), but its 40 mm peak value was in line with that reported by Cappozzo et al., (1996) and Sati et al., (1996). Average values at the shank, were similar to the 8 mm reported by Akbarshahi et al., (2010), with lateral malleus values comparable to the 2 ± 3 mm observed in static positions by Maslen and Ackland, (1994). Finally, the low-magnitude STA generated at the foot (peak values of 1.9 ± 0.6 mm) confirmed the fluoroscopy-based results of Wrbaskić and Dowling (2007), who found strongly correlated patterns for skin and bone mounted marker trajectories.

The sensitivity of the three selected MSMs to the STA was evident for most of the investigated output quantities, with different amplitudes but similar patterns observed for the three models, despite the differences in their bone and joint definitions, muscular-tendon parameters and even number of limbs. Maximum, mean and standard deviation of the output variation intervals increased from the ankle to the hip for most of the variables, reflecting the STA amplitude found on adjacent segments. When investigating the probabilistic effect of the STA on joint kinematics for different models, El Habarachi et al (2015) found a different pattern,

with the highest values reported for the ankle. This disagreement is likely due to the fact that, in contrast with the literature, they considered the pelvis and foot segments affected by a STA modelled with the same amplitude. Our results partially differ also from those of Myers et al., (2015), who also investigated G2392. They observed mean joint angle variation intervals of 5°, 2° and 6° for hip flexion, knee flexion and ankle dorsiflexion, respectively, whereas we found values of 15°, 8° and 6°, respectively. However, Myers et al. (2015) set a maximum constraint of 15 mm for their probabilistically generated STA. Although this constraint seems to be plausible for the markers used to estimate the foot kinematics, much higher values would be expected for the thigh and shank markers, and this may explain the divergence from our results. This may also explain the similar variation of the joint moments at the ankle (0.03 Nm/kg) and the almost doubled variation at the hip and the knee as compared to corresponding variations reported by Myers et al., (hip: 0.09 Nm/kg vs 0.24 Nm/kg; knee: 0.07 Nm/kg vs 0.14 Nm/kg).

The present study was affected by some limitations. Firstly, only gait was investigated while different motor tasks exhibiting a larger range of motion such as squatting or running may have shown different sensitivities to the STA. Further studies are however needed to prove this prediction. Secondly, we limited the analysis to data from one representative subject of a healthy population and caution should therefore be used when considering the reported results in association with data from pathological subjects. Pathological gait kinematics may in fact be characterised by different baseline data with the corresponding sensitivity analysis leading to different output variations. Thirdly, we investigated the model sensitivity to STA alone while the interaction between this aspect and other parameters and assumptions (e.g. model anatomy such as joint centre estimation, inertial parameters, and muscle function) may have altered the model sensitivity further. More research is needed to fully address this aspect. Lastly, raw marker data was used as an input to the inverse kinematics tool to provide a first and general assessment on the STA effects on MSMs; however, methods to reduce the STA on the bone pose estimation from stereophotogrammetric skin markers have been extensively studied, possibly offering an additional step to be tested in a new sensitivity study. These methods include the Point Cluster Technique (Andriacchi et al., 1998), SVD-based

approaches (Chèze et al., 1995), Geometrical approaches (Della Croce et al., 2003), and the Optimal Common Shape Technique (Taylor et al., 2005).

Despite the above limitations, the present analysis provides useful information to deal with the unsolved problem of the STA that inevitably propagates to the estimates of MSMs. The reported results suggest that current MSMs, driven by stereophotogrammetric recordings of skin-mounted marker trajectories, might be effectively used when an overall pattern is more important than an accurate quantitative estimation, such as in comparative cohort-based studies (Steele et al., 2012; Zabala et al., 2013). The amount of observed variation, higher than 30% in some cases, suggests that caution should be exercised in interpreting the results when MSMs are used for applications requiring a very accurate level of estimation, and in particular when they are used for subject-specific estimation of joint kinetics and bone strains. More research is required to optimise marker sets and their placement, the inverse kinematics algorithm and to develop STA compensation techniques.

In conclusion, this part of the thesis determined how much traditional MSMs combined with traditional MBO are affected by STA. This is crucial to be able to (a) clearly understand the limitations of the state-of-the-art, (b) identify directions of improvement for the future work, and (c) draw meaningful conclusions on a specific population. As discussed previously, the amount of variation observed in the MSM estimates due to STA is not trivial when stereophotogrammetry and skin markers are used. Concerning clinical applications, caution should be exercised in using muscle and joint contact forces predicted by MSMs. Indeed, especially at the hip, the level of output uncertainty observed might jeopardise clinical decisions based on the current models and methods. However, by looking at the results of the current chapter, users of the described MSMs and tools should now be aware of the actual sensitivity of the model output to the STA. This will allow establishing the limits within which output variations found in a certain population are to be deemed significant. This awareness should help to better design and tailor each research question or clinical application to be in line with the strengths and limitations of the available framework.

The following chapters of this thesis will focusing on proposing and test alternatives to this traditional framework both in terms of alternative joint modelling and innovative MBO methods.

References

Akbarshahi, M., Schache, A.G., Fernandez, J.W., Baker, R., Banks, S., Pandy, M.G., 2010. Non-invasive assessment of soft-tissue artifact and its effect on knee joint kinematics during functional activity. J. Biomech. 43, 1292–301.

Anderson, A.E., Ellis, B.J., Weiss, J.A., 2007. Verification, validation and sensitivity studies in computational biomechanics. Comput. Methods Biomech. Biomed. Engin. 10, 171–84.

Anderson, F.C., Pandy, M.G., 2001. Static and dynamic optimization solutions for gait are practically equivalent. J. Biomech. 34, 153–161.

Andriacchi, T.P., Alexander, E.J., Toney, M.K.K., Dyrby, C.O., Sum, J. a., 1998. A point cluster method for in vivo motion analysis: applied to a study of knee kinematics. J. Biomech. Eng. 120, 743.

Arnold, E.M., Hamner, S.R., Seth, A., Millard, M., Delp, S.L., 2013. How muscle fiber lengths and velocities affect muscle force generation as humans walk and run at different speeds. J. Exp. Biol. 216, 2150–2160.

Arnold, E.M., Ward, S.R., Lieber, R.L., Delp, S.L., 2010. A model of the lower limb for analysis of human movement. Ann. Biomed. Eng. 38, 269–79.

Baldwin, M. a, Laz, P.J., Stowe, J.Q., Rullkoetter, P.J., 2009. Efficient probabilistic representation of tibiofemoral soft tissue constraint. Comput. Methods Biomech. Biomed. Engin. 12, 651–659.

Barre, A., Armand, S., 2014. Biomechanical ToolKit: Open-source framework to visualize and process biomechanical data. Comput. Methods Programs Biomed. 114, 80–87.

Bergmann, G., Deuretzbacher, G., Heller, M., Graichen, F., Rohlmann, a., Strauss, J., Duda, G.N., 2001. Hip contact forces and gait patterns from routine activities. J. Biomech. 34, 859–871.

Bonci, T., Camomilla, V., Dumas, R., Chèze, L., Cappozzo, A., 2014. A soft tissue artefact model driven by proximal and distal joint kinematics. J. Biomech. 47, 2354–61.

Bosmans, L., Valente, G., Wesseling, M., Van Campen, A., De Groote, F., De Schutter, J., Jonkers, I., 2015. Sensitivity of predicted muscle forces during gait to anatomical variability in musculotendon geometry. J. Biomech. 48, 2116–2123.

Cappozzo, A., Catani, F., Leardini, A., Benedetti, M.G., Della Croce, U., 1996. Position and orientation in space of bones during movement: Experimental artefacts. Clin. Biomech. 11, 90–100.

Cereatti, A., Della Croce, U., Cappozzo, A., 2006. Reconstruction of skeletal movement using skin markers: comparative assessment of bone pose estimators. J. Neuroeng. Rehabil. 3, 7.

Chèze, L., Fregly, B.J., Dimnet, J., 1995. A solidification procedure to facilitate kinematic analyses based on video system data. J. Biomech. 28, 879–884.

De Leva, P., 1996. Adjustments to zatsiorsky-seluyanov's segment inertia parameters. J. Biomech. 29, 1223–1230.

Della Croce, U., Camomilla, V., Leardini, A., Cappozzo, A., 2003. Femoral anatomical frame: Assessment of various definitions. Med. Eng. Phys. 25, 425–431.

Delp, S.L., Anderson, F.C., Arnold, A.S., Loan, P., Habib, A., John, C.T., Guendelman, E., Thelen, D.G., 2007. OpenSim: Open-Source Software to Create and Analyze Dynamic Simulations of Movement. IEEE Trans. Biomed. Eng. 54, 1940–1950.

Delp, S.L., Loan, J.P., Hoy, M.G., Zajac, F.E., Topp, E.L., Rosen, J.M., 1990. An interactive graphics-based model of the lower extremity to study orthopaedic surgical procedures. IEEE Trans. Biomed. Eng. 37, 757–67.

Dumas, R., Cheze, L., 2009. Soft tissue artifact compensation by linear 3D interpolation and approximation methods. J. Biomech. 42, 2214–2217.

El Habachi, A., Moissenet, F., Duprey, S., Cheze, L., Dumas, R., 2015. Global sensitivity analysis of the joint kinematics during gait to the parameters of a lower limb multi-body model. Med. Biol. Eng. Comput. 655–667.

Haldar, A., Mahadevan, S., 2000. Probability, reliability and statistical methods in engineering design. John Wiley & Sons, Inc., New York.

Hara, R., Sangeux, M., Baker, R., McGinley, J., 2014. Quantification of pelvic soft tissue artifact in multiple static positions. Gait Posture 39, 712–717.

Harrington, M.E., Zavatsky, a. B., Lawson, S.E.M., Yuan, Z., Theologis, T.N., 2007. Prediction of the hip joint centre in adults, children, and patients with cerebral palsy based on magnetic resonance imaging. J. Biomech. 40, 595–602.

Heller, M.O., Bergmann, G., Deuretzbacher, G., Dürselen, L., Pohl, M., Claes, L., Haas, N.P., Duda, G.N., 2001. Musculo-skeletal loading conditions at the hip during walking and stair climbing. J. Biomech. 34, 883–893.

Hemmerich, A., Brown, H., Smith, S., Marthndam, S.S.K., Wyss, U.P., 2006. Hip, Knee, and Ankle Kinematics of High Range of Motion. J. Orthop. Res. 11, 770–781.

Hermens, H.J., Freriks, B., Disselhorst-Klug, C., Rau, G., 2000. Development of recommendations for SEMG sensors and sensor placement procedures. J. Electromyogr. Kinesiol. 10, 361–374.

Hicks, J.L., Uchida, T.K., Seth, A., Rajagopal, A., Delp, S., 2015. Is my model good enough? Best practices for verification and validation of musculoskeletal models and simulations of human movement. J. Biomech. Eng. 137.

Kadaba, M.P., Ramakrishnan, H.K., Wootten, M.E., Gainey, J., Gorton, G., Cochran, G. V, 1989. Repeatability of kinematic, kinetic, and electromyographic data in normal adult gait. J. Orthop. Res. 7, 849–860.

Klein Horsman, M.D., Koopman, H.F.J.M., van der Helm, F.C.T., Prosé, L.P., Veeger, H.E.J., 2007. Morphological muscle and joint parameters for musculoskeletal modelling of the lower extremity. Clin. Biomech. (Bristol, Avon) 22, 239–47.

Koehle, M.J., Hull, M.L., 2008. A method of calculating physiologically relevant joint reaction forces during forward dynamic simulations of movement from an existing knee model. J. Biomech. 41, 1143–6.

Laughlin, W.A., Weinhandl, J.T., Kernozek, T.W., Cobb, S.C., Keenan, K.G., O'Connor, K.M., 2011. The effects of single-leg landing technique on ACL loading. J. Biomech. 44, 1845–1851.

Laz, P.J., Browne, M., 2010. A review of probabilistic analysis in orthopaedic biomechanics. Proc. Inst. Mech. Eng. Part H J. Eng. Med. 224, 927–943.

Leardini, A., Chiari, L., Della Croce, U., Cappozzo, A., 2005. Human movement analysis using stereophotogrammetry. Part 3. Soft tissue artifact assessment and compensation. Gait Posture 21, 212–25.

Lilliefors, H.W., 1967. On the Kolmogorov-Smirnov Test for Normality With Mean and Variance Unknown. J. Am. Stat. Assoc. 62, 399–402.

Lu, T.-W., O'Connor, J.J., 1999. Bone position estimation from skin marker co-ordinates using global optimisation with joint constraints. J. Biomech. 32, 129–134.

Mantoan, A., Pizzolato, C., Sartori, M., Sawacha, Z., Cobelli, C., Reggiani, M., 2015. MOtoNMS: A MATLAB toolbox to process motion data for neuromusculoskeletal modeling and simulation. Source Code Biol. Med. 10, 12.

Martelli, S., Calvetti, D., Somersalo, E., Viceconti, M., 2015. Stochastic modelling of muscle recruitment during activity. Interface Focus 5, 20140094–20140094.

Martelli, S., Valente, G., Viceconti, M., Taddei, F., 2014. Sensitivity of a subject-specific musculoskeletal model to the uncertainties on the joint axes location. Comput. Methods Biomech. Biomed. Engin. 18, 1555–63.

Maslen, B. a., Ackland, T.R., 1994. Radiographic study of skin displacement errors in the foot and ankle during standing. Clin. Biomech. 9, 291–296.

Modenese, L., Phillips, A.T.M., 2012. Prediction of hip contact forces and muscle activations during walking at different speeds. Multibody Syst. Dyn. 28, 157–

168.

Modenese, L., Phillips, a. T.M., Bull, a. M.J., 2011. An open source lower limb model: Hip joint validation. J. Biomech. 44, 2185–2193.

Mokhtarzadeh, H., Perraton, L., Fok, L., Muñoz, M.A., Clark, R., Pivonka, P., Bryant, A.L., 2014. A comparison of optimisation methods and knee joint degrees of freedom on muscle force predictions during single-leg hop landings. J. Biomech. 47, 2863–2868.

Myers, C. a., Shelburne, K.B., Laz, P.J., Davidson, B.S., 2015. A Probabilistic Approach to Quantify the Impact of Uncertainty Propagation in Musculoskeletal Simulations. Ann. Biomed. Eng. In Review, 1098–1111.

Peters, A., Galna, B., Sangeux, M., Morris, M., Baker, R., 2010. Quantification of soft tissue artifact in lower limb human motion analysis: a systematic review. Gait Posture 31, 1–8.

Rozumalski, A., Schwartz, M.H., Novacheck, T.F., Wervey, R., Swanson, A., Dykes, D.C., 2007. Quantification of pelvic soft tissue artifact. In: Gait and Clinical Movement Analysis Society. pp. 10–11.

Sati, M., De Guise, J.A., Larouche, S., Drouin, G., 1996. Quantitative assessment of skin-bone movement at the knee. Knee 3, 121–138.

Stagni, R., Fantozzi, S., Cappello, A., Leardini, A., 2005. Quantification of soft tissue artefact in motion analysis by combining 3D fluoroscopy and stereophotogrammetry: A study on two subjects. Clin. Biomech. 20, 320–329.

Steele, K.M., Demers, M.S., Schwartz, M.H., Delp, S.L., 2012. Compressive tibiofemoral force during crouch gait. Gait Posture 35, 556–60.

Taylor, W.R., Ehrig, R.M., Duda, G.N., Schell, H., Seebeck, P., Heller, M.O., 2005. On the influence of soft tissue coverage in the determination of bone kinematics using skin markers. J. Orthop. Res. 23, 726–734.

Tranberg, R., Karlsson, D., 1998. The relative skin movement of the foot: A 2-D roentgen photogrammetry study. Clin. Biomech. 13, 71–76.

Tsai, T.-Y., Lu, T.-W., Kuo, M.-Y., Hsu, H.-C., 2009. Quantification of Three-Dimensional Movement of Skin Markers Relative To the Underlying Bones During Functional Activities. Biomed. Eng. Appl. Basis Commun. 21, 223–232.

Valente, G., Pitto, L., Testi, D., Seth, A., Delp, S.L., Stagni, R., Viceconti, M., Taddei, F., 2014. Are Subject-Specific Musculoskeletal Models Robust to the Uncertainties in Parameter Identification? PLoS One 9, e112625.

Viceconti, M., Testi, D., Taddei, F., Martelli, S., Clapworthy, G.J., Van Sint Jan, S., 2006. Biomechanics modeling of the musculoskeletal apparatus: Status and key issues. Proc. IEEE 94, 725–738.

Wagner, D.W., Stepanyan, V., Shippen, J.M., DeMers, M.S., Gibbons, R.S., Andrews, B.J., Creasey, G.H., Beaupre, G.S., 2013. Consistency Among Musculoskeletal Models: Caveat Utilitor. Ann. Biomed. Eng. 41, 1787–1799.

Ward, S.R., Eng, C.M., Smallwood, L.H., Lieber, R.L., 2009. Are Current Measurements of Lower Extremity Muscle Architecture Accurate? Clin. Orthop. Relat. Res. 467, 1074–1082.

Wesseling, M., Derikx, L.C., de Groote, F., Bartels, W., Meyer, C., Verdonschot, N., Jonkers, I., 2015. Muscle optimization techniques impact the magnitude of calculated hip joint contact forces. J. Orthop. Res. 33, 430–438.

Wrbaskić, N., Dowling, J.J., 2007. An investigation into the deformable characteristics of the human foot using fluoroscopic imaging. Clin. Biomech. (Bristol, Avon) 22, 230–8.

Yamaguchi, G.T., Zajac, F.E., 1989. A planar model of the knee joint to characterize the knee extensor mechanism. J. Biomech. 22, 1–10.

Zabala, M.E., Favre, J., Scanlan, S.F., Donahue, J., Andriacchi, T.P., 2013. Three-dimensional knee moments of ACL reconstructed and control subjects during gait, stair ascent, and stair descent. J. Biomech. 46, 515–20.

CHAPTER 4

Modelling the mechanical behaviour of the tibiofemoral joint using compliance matrices

As introduced in the previous chapters, the knee is usually represented in MSMs with very simple mechanical equivalents, such as a hinge joint or a spherical joint. This simplified representation only accounts for the kinematics of the joint, usually neglecting the possibility of a more complex motion (i.e. translation along certain directions and/or rotations about specific axes), which could indeed be crucial to capture pathological conditions. Increasing the model complexity to account for a force-dependent behaviour at the joint is one possible direction to go. This idea, based on calculating a discrete set of compliance matrices of the knee, is described in the first part of the current chapter (4.1.).

When a more complex knee joint model is designed, however, a new challenge needs to be addressed. This is related to the implementation of new MBO algorithms being able to deal with the increased model complexity. Indeed, when the force information is included in the knee model, the traditional MBO become not usable. The second part of this chapter (4.2.) will describe the mathematical basis upon which a new MBO algorithm, which uses stereophotogrammetric data as an input. The new MBO algorithm will be based on one representative compliance matrix calculated in the first part of the chapter.

4.1. Tibiofemoral model development

A considerable part of the material presented in this section is based on:

Lamberto, G., Richard, V., Dumas, R., Valentini, P.P., Pennestrì, E., Lu, T.-W., Camomilla, V., Cappozzo, A., (2016). "Modeling the Human Tibiofemoral Joint Using *Ex Vivo* Determined Compliance Matrices.", *J. Biomech. Eng*. 138, 61010. doi:10.1115/1.4033480.

Written permission was obtained from all the co-authors as well as the publisher (ASME).

Author's contribution for this section (4.1) was related to the design of the experimental protocol and supervise the execution of the experiments in person. The experiments took place in Taiwan due an ongoing collaboration between Prof. Aurelio Cappozzo and Prof. Tung-Wu Lu, established several years ago. Author's thesis also worked at the post-processing of the results and model development in MATLAB, and manuscript preparation.

4.1.1. Introduction

Biomechanical modelling of the knee joint has been the object of several studies in the last 30 years (Arnold et al., 2010; Baldwin et al., 2012; Beynnon et al., 1996; Fernandez and Pandy, 2006; Halloran et al., 2005; Hu et al., 2013; Moissenet et al., 2014; Ribeiro et al., 2012; Sancisi and Parenti-Castelli, 2011; Shelburne et al., 2005; Yamaguchi and Zajac, 1989; Yang et al., 2010) with the aim of better understanding the passive joint behaviour and estimate the joint contact and ligament forces during motor tasks under physiological and pathological conditions. To address these objectives, comprehensive finite element or multi-body models (Bendjaballah et al., 1998; Donahue et al., 2002; Guess et al., 2010; Kazemi et al., 2013; Li et al., 1999; Peña et al., 2006) have been developed and, in some cases, validated against *ex vivo* data.

Due to numerical issues, knee models in general rely on kinematic constraints (i.e. allowing movement only in a predetermined way or in certain directions – see Chapter 2.2), which may include ligaments with infinite stiffness and/or passive joint moments (Al Nazer et al., 2008; Anderson and Pandy, 2001). Passive joint moments are introduced in simulations mainly with the aim of preventing exceedingly large joint amplitudes. They account for all the passive contribution at each joint (i.e. ligaments, cartilage, and shape of the contacting articular surfaces) and can be related to the level of activity of a subject (i.e. stiffer joint if a subject is not moving due to a surgical operation). In general, higher passive moments are associated to more inactive subjects with stiffer joints (Amankwah et al., 2004). The passive moments are defined as linear or exponential functions of the joint angles. The stiffness values, embedded in these curves, are not determined experimentally but result from a tuning or calibration procedure and comply with numerical requirements of the optimisation approach. Another modelling approach, called "force dependent kinematics", has been recently proposed (Andersen et al., 2011; Andersen and Rasmussen, 2011). The idea is to optimise the estimate of joint kinematics to ensure the static equilibrium of the joint according to a set of stiffness values, again, resulting from a numerical procedure.

An alternative modelling approach would be to directly introduce a knee compliance matrix (or its inverse named stiffness matrix) resulting from *ex vivo* experiments into the MSM. This matrix provides the joint displacements as a function of the loads acting through the joint. Such approach has been previously proposed for the intervertebral joints (Christophy et al., 2012; Koell et al., 2010; Marin et al., 2010; Petit et al., 2004), but not for other joints. One interesting property of the compliance matrix is that the extra-diagonal terms describe the physiological couplings between the DoFs. In addition, pathological conditions, such as ligament or meniscal tears, can be revealed by altered matrix terms. Nevertheless, despite a general availability of robotic-manipulators (Fujie et al., 1993), the knowledge of the knee compliance matrix is rather limited. Indeed, investigations of the tibiofemoral joint kinematics response to loading have been restricted either to few selected directions or to a limited number of knee configurations (i.e., typically 0° of flexion). For example, Markolf et al. (1976) performed one of the most complete studies available, analysing the relationship between moments and adduction-abduction and internal-

external rotations, as well as force and linear displacement in the anterior-posterior direction, at six different flexion angles. Eagar et al. (2001) quantified the anterior-posterior load-displacement behaviour in both linear and non-linear regions at four different flexion angles. Fox et al. (1998) and Kanamori et al. (2000) determined the *in situ* forces in the posterior and anterior cruciate ligaments, respectively, in response to different loading conditions and in more than one configuration (i.e. 0°, 15°, 30°, 60°, 90° of flexion). However, to the best of the author's knowledge, only Loch et al. (1992) tried to characterise the mechanical behaviour of the passive structures that constrain the knee joint using a compact 6x6 matrix, but that research was limited to a single knee configuration (i.e., 0° of flexion). Moreover, the way the terms of the matrix were derived from experimental data is not clearly stated.

The aim of this part of the thesis was to present a method to mathematically define and experimentally determine a set of compliance matrices in different knee configurations. A quasi-static approach was selected by applying, through a robotic arm, small displacements about a number of selected equilibrium poses of the knee (Fox et al., 1998; Kanamori et al., 2000). The load-displacement relationships were expressed by 6x6 symmetric compliance matrices. Experiments were carried out on a cadaveric knee specimen, both intact and with the anterior cruciate ligament (ACL) transected. In addition, a validation procedure was implemented to test the ability of the compliance matrix to estimate linear and angular displacements as caused by an arbitrary load.

4.1.2. Material and methods

4.1.2.1. Specimen preparation

A single intact fresh-frozen human knee joint obtained from a 75 year old female was tested. The specimen was a left leg derived from an amputation due to an acute arterial occlusion. Ethical approval for the experimental work was granted by the Institutional Research Board of China Medical University Hospital (Taichung City, Taiwan). The knee was kept frozen until the time of use. The effects of post-mortem on ligaments material properties have been reported as no significant for human and animal specimens kept frozen and stored effectively (Noyes and Grood, 1976; Viidik

et al., 1965; Woo et al., 1986). The surgeon, who prepared the knee for the experiments, declared it normal. The specimen was sectioned at the mid-shaft of the femur and tibia and dissected down to the joint capsule and major ligaments. All the muscles, the patella, and the patellar tendon were removed in order to mechanically characterise the behaviour of the tibiofemoral passive structures. The bones were mounted through cement in two aluminium fixation supports to be connected to a Robot-based Joint Testing System (RJTS) (Hsieh et al., 2016). On the day of testing, the knee was thawed and pre-conditioned (Most et al., 2004), and the tissues regularly sprayed with a saline mist. The last aspect is crucial to maintain a proper level of tissue hydration; otherwise reduced level of hydration determined a change in material properties (Haut and Powlison, 1990). After testing the intact knee, all the ACL bundles were surgically transected and the experimental procedure repeated.

4.1.2.2. Experimental apparatus and procedure

The RJTS consists of an industrial robotic system (RV-20A, Mitsubishi Electric Corporation, Japan) and a six-component load cell (Universal Force Sensor, Model PY6-100, Bertec Corporation, USA) that was attached to the end effector of the robot for the measurement of the three force and three moment components of the load (Figure 4.1A). The robot was recently developed for applications in *ex vivo* biomechanical studies (Hsieh et al., 2016). This testing device is capable of a hybrid position/load control using traditional and innovative methods. Control methods were evaluated performing tests on a human cadaveric knee both in translation along and in rotation about a selected axis, where their convergence and their residual constraining load were compared against published standard methods. The results, showing a repeat accuracy of 0.1 mm, suggested system suitability for accurate and reliable testing of biological joints (Hsieh et al., 2016). The sampling rate of the acquisition was 10 samples per second.

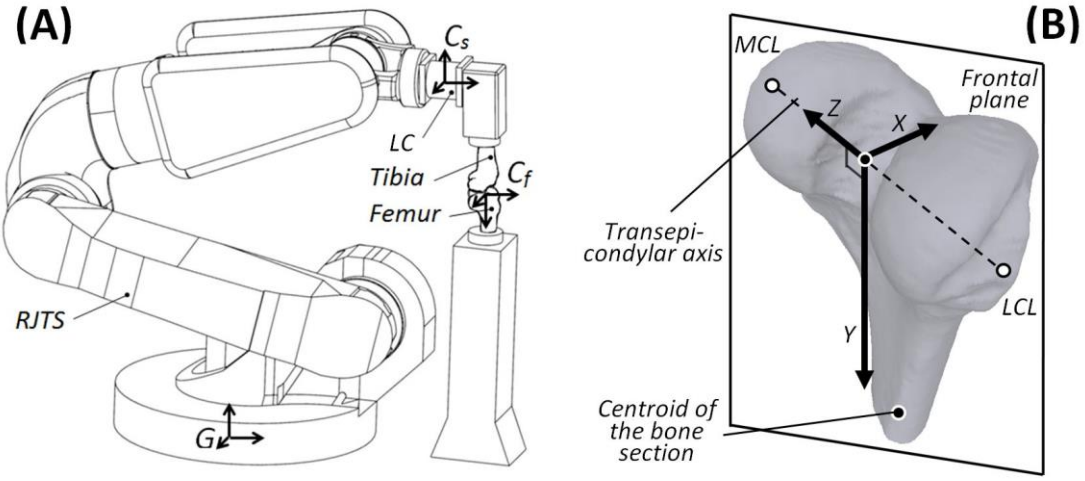

Figure 4.1 - A) A schematic representation of the Robot-based Joint Testing System (RJTS) and the reference systems used are provided: G is the global coordinate system; C_s is the coordinate system of the load cell (LC) and C_f is the anatomical coordinate system of the femur. B) C_f was defined as follows: the origin was the midpoint between the medial collateral ligament (MCL) and lateral collateral ligament (LCL) insertions; the z-axis was made to pass through LCL and MCL (transepicondylar axis) and pointed towards the latter point. The y axis was defined as lying on the plane defined by LCL, MCL, and the centroid of the bone section (frontal plane) and perpendicular to the z axis pointing toward the proximal part of the bone. Finally, the x-axis was defined to be perpendicular to both the y- and the z-axes and oriented to generate a right-handed frame. Obtained from Lamberto et al., (2016) with ASME permission.

A method to identify bony landmarks for the definition of femur and tibia anatomical coordinated systems and therefore of the knee joint coordinate system (JCS) was adapted from Fujie et al. (2004).

A calibration procedure was performed using a pointer mounted on the end-effector of the robot (Figure 4.2). Using this pointer, the position of the femoral insertion sites of the medial collateral ligament and the lateral collateral ligament were identified in the global coordinate system. The centroid of the femoral section was assumed as coincident with the geometrical centre of the fixation support, the position of which was determined before mounting the specimen. These points were used to define the anatomical coordinate system of the femur (C_f) (details in Figure 4.1B). The anatomical coordinate system of the tibia (C_t) was defined as coincident with C_f at full extension. The forces and moments were recorded by the load cell in the sensor coordinate system (C_s) (Figure 4.1A).

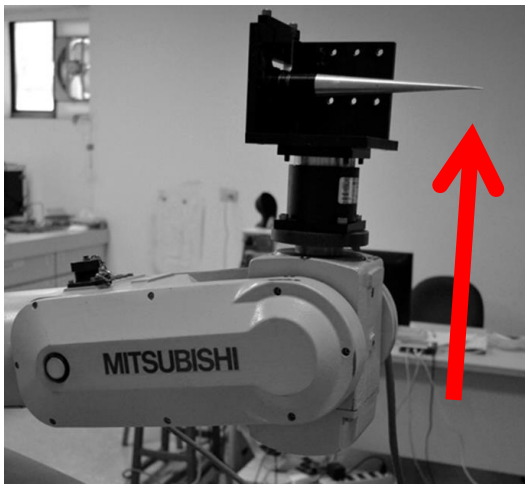

Figure 4.2 - Pointer used to identify bony landmarks (end point indicated by the red arrow).

Flexion-extension (F-E), adduction-abduction (A-A), and internal-external (I-E) rotations were defined as motions about the JCS axes (e1: *z*-axis of C_f, e2: floating axis, e3: y-axis of C_t). Medial-lateral (M-L), anterior-posterior (A-P), and proximal-distal (P-D) linear displacements were characterised as motions along these axes. A sign inversion was used to report positive values for the flexion angles, otherwise negative by convention. Measured loads were represented in the JCS using a Jacobian matrix. Full details about this transformation are available in the study of Fujie et al., (1996).

A set of pre-determined F-E angles were used to determine the compliance matrices of the intact knee: 0°, 15°, 30°, 45°, 60°, 75°and 90°. For each F-E angle, the neutral pose, i.e. the A-A and I-E rotations, and M-L, A-P and P-D displacements, was determined so that the measured joint moments and forces were minimal (Fujie et al., 1996). The same neutral poses were later used for the ACL-deficient knee experiment. Constrained control was then used to perform single DoF tests (Hsieh et al., n.d.). These tests were defined by the application of the following procedure: starting from the neutral pose, linear or angular displacement increments (at rates of 0.93 mm/s and 0.97 °/s) were applied one at a time along and about each single DoF, under moment and force limitations to avoid any damage to the soft tissues. The force limitations, adopted both for the intact and ACL-deficient knee, were 100 N along A-P and P-D, and 80 N along L-M as similarly applied in (Grood, 1988). Limitations of moments were conservatively set at 25% of those used in (Markolf KL et al., 1976; Zantop et al., 2007), and were 2.5 Nm for A-A, and 1 Nm for I-E.

To evaluate the prediction capability of the compliance matrix, a Lachman test was simulated. With the knee flexed at 30°, a force, linearly increasing in time, was applied to the tibia along the A-P axis, under the force limitation mentioned previously. The whole experimental procedure is summarised in Table 4.1.

Status of Knee	Knee F-E angle	Procedure steps	Robot Control	Compliance matrix calculation	Compliance matrix validation
Intact knee	0°, 15°, 30°, 45° 60°, 75° and 90°	Determination of the neutral pose of the knee	Hybrid control	✓	
		Single DoF tests	Constrained Control	✓	
	30°	Lachman test	Force control		✓
ACL-deficient knee	0°, 15°, 30°, 45°, 60°, 75° and 90°	Single DoF tests	Constrained Control	✓	
	30°	Lachman test	Force control		✓

Table 4.1 - The experimental procedure for the compliance matrices calculation and validation is summarised in a chronological order.

4.1.2.3. Post-processing procedure

The post-processing procedure was based on the procedure proposed by Stokes et al. (2002) and adapted to the experimental data of the present procedure.

The compliance matrix $[C]$ was assumed 6x6 symmetric:

$$[C]\{F - F_0\} = \{X - X_0\} \quad 4.1$$

where $\{X\}$ is a 6x1 generalised displacement vector of the A-P, P-D and M-L displacements followed by the A-A, I-E, and F-E rotations and $\{F\}$ is a 6x1 load vector of the corresponding forces and moments. $\{X_0\}$ and $\{F_0\}$ are the same 6x1 vectors obtained at the neutral poses of the knee. The generic 6x6 symmetric compliance matrix [C] has 21 independent compliance terms (6 translational, 6 rotational, and 9 coupling terms), $\{c\}$, that can be obtained by rearranging Equation 4.1 into the standard least squares inversion form:

$$[L]\{c\} = \{X - X_0\} \quad 4.2$$

where $[L]$ is a 6x21 matrix based on the six terms of $\{F - F_0\}$ (the incremental load vectors) and $\{c\}$ is a 21x1 vector of the 21 independent compliance matrix terms. This vector $\{c\}$ was obtained through a least squares inversion using, for each F-E angle, the 3D displacements and loads obtained from all the incremental displacements applied about each single DoF. In this way, it is not the 6*6 matrix terms that were computed but the 21 independent terms directly. Thus, the 9 coupling terms have not been averaged to make the matrix symmetric, as is performed classically in the literature (Gardner-Morse and Stokes, 2004).

The compliance terms were set as unknown to be determined with respect to the stiffness terms. This approach prevented proportional vectors in the coefficient matrix of the standard least squares form (Equation 4.2). In fact, setting stiffness terms as unknown would have filled the coefficient matrix with the proportional imposed linear increments of the single DoF tests, introducing a rank-deficiency in the computation. In addition, a QR decomposition (Equation 4.3) was used to avoid numerical instability (Pennestrì and Cheli, 2006) and each matrix was constrained to be positive defined. Re-sampling using cubic spline interpolation was performed since the data has different frame numbers, according to the different moment and force limitations imposed. Ultimately, only the first fifteen frames were considered to ensure a certain range of linearity around the neutral pose and, at the same time, to consider the contribution of each single DoF test to the overall matrix. Concerning the latter aspect, at least ten frames from each single DoF test were assumed to be representative in the overall matrix.

$$[A] = [Q][R]; \qquad Q\ orthogonal\ matrix, R\ upper\ triangular\ matrix \quad 4.3$$

4.1.2.4. Validation

For the purpose of validation, the compliance matrices computed at 30° of F-E with both intact and ACL-deficient knee were used to predict the A-P, P-D and M-L displacements and A-A, I-E and F-E rotations using Equation 4.1 and the forces and moments measured during the simulated Lachman test. The absolute errors between

calculated and measured linear and angular displacements were computed (Equation 4.4).

$$\{Abs_{err}\} = [C_{30}]_{computed}\{F - F_0\}_{measured} - \{X - X_0\}_{measured} = \\ = \{X - X_0\}_{predicted} - \{X - X_0\}_{measured} \quad 4.4$$

4.1.3. Results

The compliance matrices for the intact and the ACL-deficient knee are displayed at 0° and 30° of F-E in Table 4.2 and Table 4.3, respectively. The matrices at 15°, 45°, 60°, 75° and 90° can be found in Table 4.4 and Table 4.5.

Status of knee	F_x	F_y	F_z	M_x	M_y	M_z	
intact	8483.0	-3601.3	1653.0	24.7	113.1	185.0	**T_x**
ACL cut	*29173.0*	*-12305.8*	*-11451.1*	*104.8*	*-40.8*	*496.7*	
intact		5575.4	-561.1	-1.9	-43.4	-134.7	**T_y**
ACL cut		*14879.4*	*1225.2*	*59.2*	*15.0*	*-362.8*	
intact			15712.5	28.0	279.9	-135.9	**T_z**
ACL cut			*24440.1*	*-153.7*	*-66.0*	*-365.2*	
intact				3.4	2.7	1.3	**R_x**
ACL cut		Symmetric		*8.0*	*-1.3*	*-0.6*	
intact					11.7	2.5	**R_y**
ACL cut					*1.1*	*-0.8*	
intact						12.7	**R_z**
ACL cut						*22.0*	

Table 4.2 - Compliance matrix computed at 0° of F-E. Units of measurements are N, mm and rad. All the compliance matrix terms have to be scaled down by a factor of $10^{(-5)}$. In this and the following tables, F_x, F_y, F_z, M_x, M_y, M_z refer to the force and moment components, respectively, and T_x, T_y, T_z, R_x, R_y, R_z to the linear displacement components and the rotations, respectively.

Status of knee	F_x	F_y	F_z	M_x	M_y	M_z	
intact	2991.3	572.9	5793.4	92.5	42.1	-180.0	T_x
ACL cut	*21321.8*	*-5513.2*	*27461.0*	*0.1*	*-332.5*	*-286.9*	
intact		8559.8	-5852.4	-7.6	1.6	-312.3	T_y
ACL cut		*17246.3*	*-24766.5*	*89.5*	*26.4*	*-258.2*	
intact			16999.8	190.3	68.3	-56.0	T_z
ACL cut			*76015.9*	*-217.6*	*-46.0*	*800.0*	
intact				9.8	8.5	-18.4	R_x
ACL cut		Symmetric		*33.9*	*39.1*	*-60.7*	
intact					21.2	-26.3	R_y
ACL cut					*62.9*	*-51.9*	
intact						126.7	R_z
ACL cut						*133.2*	

Table 4.3 - Compliance matrix computed at 30° of F-E. Units of measurements are N, mm and rad. All the compliance matrix terms have to be scaled down by a factor of $10^{(-5)}$.

The vast majority of the calculated compliance terms were modified by the ACL transection. As expected, the values of the compliance terms increased after the ACL dissection when compared to their values for the intact knee structures (Table 4.2 - Table 4.5). For instance, at full extension, the incremental ratios between the sum of the compliance terms of each subgroup before and after the dissection were 1.51, 2.60, and 0.83 for the translational, rotational, and coupling terms, respectively. This behaviour accounts for the fundamental role of the ACL in preventing extreme tibiofemoral displacements when a force is applied. In addition, non-negligible coupling terms depending to the particular flexion angle were found. This highlights the importance of estimating the compliance matrix in more than one configuration.

The validation tests performed using the compliance matrices obtained at 30° of F-E for the intact and ACL-deficient knee (Table 4.3), are illustrated in Figure 4.3 and Figure 4.4, respectively. The following quantities are depicted as a function of time: the absolute errors (panels A and B) and the values of the three linear and three angular displacement components (panels C and D) computed through the compliance matrix (Equation 4.1) using the forces and moments (panels E and F) recorded during the simulated Lachman test. Coherent results were achieved both for the intact and the ACL-deficient knees at the beginning of the validation experiments, which is, when small loads were applied in proximity of the neutral pose. However, at a later stage of the experiment, absolute errors were found to increase. In particular, for controlled forces below 6 N and 3 N for the intact and the

ACL-deficient knee (0-0.5 s of testing), the maximum absolute errors were 0.58 mm, 0.21 mm and 1.49°, 0.57° for the linear and angular displacements, respectively. For controlled forces below 11 N and 8 N (0.6-1 s of testing), the errors were 1.14 mm, 0.83 mm, and 4.60°, 2.95°, respectively and increased to 1.49 mm, 2.35 mm, and 10.36°, 3.36° when forces reached 18 N and 15 N (1.1-1.5 s of testing).

15° of F-E

Status of knee	**F_x**	**F_y**	**F_z**	**M_x**	**M_y**	**M_z**	
Intact	15023.3	-14374.5	26922.1	-84.1	300.0	56.8	**T_x**
ACL cut	*44335.6*	*-313.0*	*-2912.9*	*-19.7*	*-808.2*	*-797.4*	
Intact		28838.7	-4517.2	293.0	128.1	-165.0	**T_y**
ACL cut		*13218.2*	*-6324.4*	*140.5*	*-135.7*	*-713.0*	
intact			96628.6	-175.2	-1065.2	108.3	**T_z**
ACL cut			*13028.0*	*-134.9*	*14.7*	*-227.9*	
intact				47.1	34.2	-16.6	**R_x**
ACL cut		Symmetric		*4.9*	*1.5*	*-4.6*	
intact					279.4	-13.7	**R_y**
ACL cut					*21.9*	*26.3*	
intact						26.5	**R_z**
ACL cut						*95.1*	

45° of F-E

Status of knee	**F_x**	**F_y**	**F_z**	**M_x**	**M_y**	**M_z**	
intact	2809.7	-2269.2	2404.2	80.8	131.0	-146.6	**T_x**
ACL cut	*6844.2*	*-2180.9*	*3974.5*	*7.5*	*-91.2*	*-183.7*	
intact		5999.5	-2814.8	-44.4	-233.3	-259.5	**T_y**
ACL cut		*6825.3*	*-3309.0*	*14.7*	*-173.7*	*-497.3*	
intact			5413.3	-38.9	-31.5	106.3	**T_z**
ACL cut			*8286.1*	*-15.4*	*-85.7*	*29.4*	
intact				6.1	7.7	-11.5	**R_x**
ACL cut		Symmetric		*3.7*	*0.3*	*-3.6*	
intact					25.3	-1.0	**R_y**
ACL cut					*18.2*	*28.0*	
intact						50.2	**R_z**
ACL cut						*62.2*	

Table 4.4 - Compliance matrix computed at 15° and 45° of F-E. Units of measurements are N, mm and rad. All the compliance matrix terms have to be scaled down by a factor of $10^{(-5)}$.

60° of F-E

Status of knee	F_x	F_y	F_z	M_x	M_y	M_z	
intact	1038.8	-2009.0	883.6	36.7	51.2	-19.6	T_x
ACL cut	*7395.4*	*390.6*	*7797.7*	*14.4*	*-335.8*	*-469.8*	
intact		4572.4	-614.6	-12.9	-70.6	-152.1	T_y
ACL cut		*13138.0*	*-16450.8*	*80.1*	*-163.3*	*-403.5*	
intact			6649.7	-129.9	-230.8	23.3	T_z
ACL cut			*54978.5*	*-37.2*	*-217.4*	*-328.3*	
intact				22.5	23.7	-37.3	R_x
ACL cut		Symmetric		*33.2*	*10.9*	*-27.6*	
intact					28.3	-35.1	R_y
ACL cut					*38.6*	*11.3*	
intact						81.5	R_z
ACL cut						*64.2*	

75° of F-E

Status of knee	F_x	F_y	F_z	M_x	M_y	M_z	
intact	4169.3	-3777.8	-605.7	9.7	26.8	107.9	T_x
ACL cut	*1957.1*	*-2342.8*	*457.9*	*6.8*	*-7.9*	*30.4*	
intact		3463.6	32.0	-0.1	-11.6	-99.6	T_y
ACL cut		*2841.6*	*-579.5*	*4.9*	*-5.8*	*-89.2*	
intact			6728.5	-104.2	-167.2	-20.3	T_z
ACL cut			*7293.1*	*-68.4*	*-161.7*	*-44.8*	
intact				3.3	3.8	-2.1	R_x
ACL cut		Symmetric		*8.7*	*-2.5*	*-17.0*	
intact					8.6	2.7	R_y
ACL cut					*13.2*	*23.8*	
intact						13.8	R_z
ACL cut						*77.2*	

90° of F-E

Status of knee	F_x	F_y	F_z	M_x	M_y	M_z	
intact	5369.0	-4264.1	84.9	-5.0	62.9	186.8	T_x
ACL cut	*3212.3*	*-2740.7*	*123.7*	*5.9*	*-66.1*	*10.8*	
intact		3668.6	-1475.8	18.5	-43.0	-156.1	T_y
ACL cut		*2784.9*	*-1602.1*	*24.1*	*-35.7*	*-158.0*	
intact			7038.5	-73.3	-40.4	35.5	T_z
ACL cut			*8908.0*	*-60.5*	*-133.3*	*-45.3*	
intact				1.9	1.5	0.4	R_x
ACL cut		Symmetric		*7.5*	*-10.2*	*-14.3*	
intact					10.7	11.0	R_y
ACL cut					*70.1*	*92.1*	
intact						15.5	R_z
ACL cut						*126.1*	

Table 4.5 - Compliance matrix computed at 60°, 75° and 90° of F-E. Units of measurements are N, mm and rad. All the compliance matrix terms have to be scaled down by a factor of $10^{(-5)}$.

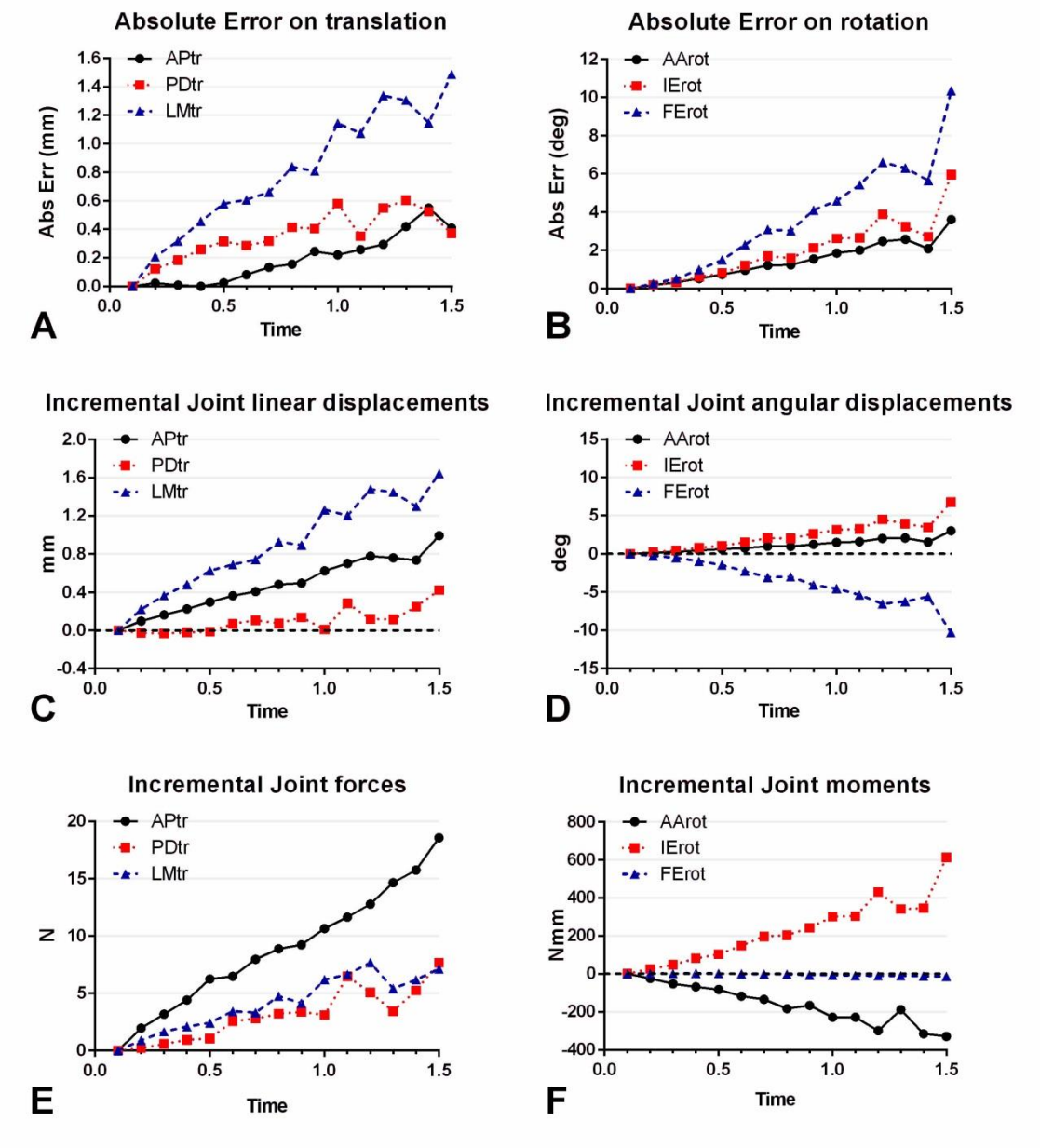

Figure 4.3 - The absolute error for the intact knee between displacements (A) and rotations (B) measured and computed with the compliance matrix at 30° of F-E is displayed. The values of A-P, P-D and M-L computed displacements (C) and measured forces (E), of A-A, I-E and F-E rotations (D) and moments (F) are also illustrated. Adapted from Lamberto et al., (2016) with ASME permission.

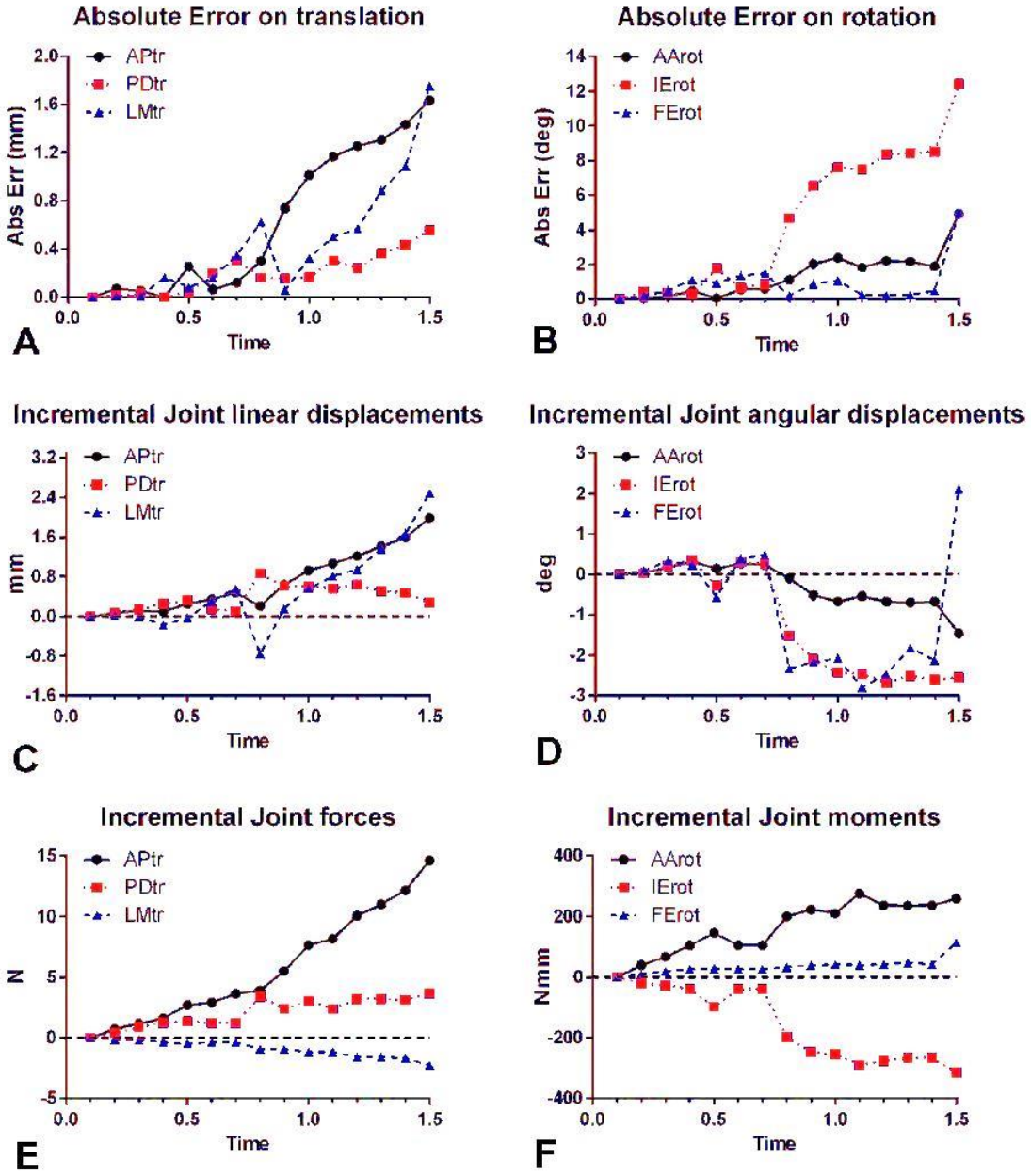

Figure 4.4 - Compliance matrix validation of the ACL-deficient knee. See the previous figure for the explanation. Adapted from Lamberto et al., (2016) with ASME permission.

4.1.4. Discussion

In this chapter, the mathematical definition and experimental determination of compliance matrices in different knee configurations was developed. The mathematical definition is based on a compliance matrix which led to a higher number of independent rows in the calculation process with respect to the stiffness matrix. The compliance terms are computed through a least squares inversion based

on QR decomposition, and the positive definition of all the matrices computed was ensured for a possible use as stiffness matrices. The experimental determination was performed, using a previously described Robot-based Joint Testing System (Hsieh et al., 2016), in different knee configurations on both an intact and ACL-deficient knee. The compliance of the knee/robot complex was computed under the assumption that the stiffness of the robot components is much higher than the knee surrounding tissues and, therefore, can be attributed exclusively to the knee (Fox et al., 1998; Zantop et al., 2007).

Validation tests of the compliance matrix determined at 30° of F-E (Lachman test) confirmed the ability to predict the A-P, P-D and M-L displacements and A-A, I-E and F-E rotations for given loads applied on the JCS axes. The maximum absolute error between predicted and measured knee linear and angular displacements increased non-linearly with respect to the values of the applied load, both for the intact and the ACL-deficient knee. As a result of the deviations from the starting neutral pose (more than 1mm and/or 1°) occurring when a force higher than 10 N in the A-P direction was applied, caution should be exercised in using the compliance matrix when high loads/displacements occur. This is also why only the first fifteen frames of the linear and angular increments of each single DoF test were used for the determination of the compliance terms. Some preliminary tests revealed that for a larger number of frames the residual of the least squares inversion was higher. The cited number of frames was selected as a good trade-off between a warranted linearity of load-displacement curves and an ensured contribution of each single DoF test to the overall matrix.

Although no other study performed the determination of a set of compliance matrices in different knee configurations, the current results can be compared with studies estimating specific terms of the compliance matrix obtained at 0° of F-E (Table 4.2). The obtained compliance terms in the first row and first column compared well with those obtained in *Markolf*'s work (1976), during an A-P stability test: the ratio after and before ACL-section was 0.29 in the current research and 0.31 by them. Similarly, in A-P direction the first diagonal term (about 0.08 mm/N) was in the range obtained by Eagar et al. (2001) who tested seven intact knee specimens (mean ± SD = 0.05 ± 0.09 and range between 0.02 and 0.17 mm/N). However, in

that study, the neutral path of flexion-extension at the knee was not defined and, as a result, no other knee configuration can be compared with the current research. Ultimately, comparing our results with the stiffness matrix calculated by Loch et al. (1992) some similarities and differences could be found. In particular, the first two translation compliance terms have the same order of magnitude as in (Loch et al., 1992), during six independent displacement tests. Conversely, in our compliance matrix the third translation compliance term and the rotational terms are two or more orders of magnitude bigger than in (Loch et al., 1992). These discrepancies can be attributed to the difference in the neutral pose at full extension since a preload was applied in (Loch et al., 1992).

This part of the thesis is based on one important assumption, which may limit the domain of application of the obtained results. In accordance with the literature (Loch et al., 1992), it is assumed that, for small linear or angular displacements relative to the overall dimension of the knee bones, the load-displacement behaviour is linear, i.e. the compliance matrices are symmetric. A second limiting factor in the application of current results is narrowing the focus only on the passive structures that constrain the human knee, therefore excluding muscular tendinous tissues, patella and patellar tendon as possible contributors to the stability or load-bearing forces. Thirdly, this part of the thesis focused on only one knee specimen. The experimental procedure was extremely time-consuming and the focus was more on determining the compliance matrices in different knee configurations than testing multiple specimens. Additionally, the definition of the reference systems (using points palpated with the rigid pointer and the centroid of the geometrical fixation centre) was limited by a lack of sensitivity analysis studying the effects of these choices on the measured outputs. Lastly, the calculation method was limited by two main factors. Only the first fifteen frames of the single DoF tests were taken into account, discarding a part of information that could be significant. Furthermore, during least square matrix inversion, the non-homogeneity of the compliance matrix was not considered as an important factor to be included in the calculation process.

Despite the above limitations, the proposed set of compliance matrices can be used to model the knee joint for its effective embedment in a MSM of the lower limb with low computational cost. The stiffness matrix (i.e., inverse of the compliance matrix)

of the intervertebral joints has been widely used in multi-body models (Christophy et al., 2013, 2012; Kim et al., 2012; Petit et al., 2004). The method proposed here for the knee joint could be the first step on the path covered previously for the spine. For that, the definition of the neutral pose is of paramount importance to compute the joint passive moments and the elastic energy. As shown in the compliance matrix validation performed in this part of the thesis, this joint modelling is valid only near the neutral poses. Therefore, the definition of a set of compliance matrices at different knee configurations (0°, 15°, 30°, 45°, 60°, 75° and 90° in this work) is of paramount importance.

The introduction of these compliance matrices, or of the corresponding stiffness matrices, into MSMs of the lower limb will be the next step to provide alternatives for femur and tibia pose estimation during movement using stereophotogrammetry and skin markers and the so-named multi-body optimisation (Lu and O'Connor, 1999). Such "compliant" constraints may provide better results than infinitely stiff constraints, like spherical or hinge joints or parallel mechanisms (Di Gregorio and Parenti-Castelli, 2003; Mokhtarzadeh et al., 2014; Ottoboni A, Parenti-Castelli V, Sancisi N, Belvedere C, 2010). The use of the matrices determined with the ACL-deficient knee open the way for defining pathological constraints.

In conclusion, the method proposed in this chapter may be a viable alternative to characterise the tibiofemoral load-dependent behaviour in several applications. This contribution might have implications on a new generation of lower limb MSMs.

4.2. Tibiofemoral joint model embedment in the musculoskeletal pipeline

A considerable part of the material presented in this section has been based on:

Richard, V., Lamberto, G., Lu, T.-W., Cappozzo, A., Dumas, R., (2016). "Knee Kinematics Estimation Using Multi-Body Optimisation Embedding a Knee Joint Stiffness Matrix: A Feasibility Study." *PLoS One,* 11, e0157010. doi:10.1371/journal.pone.0157010

Written permission was obtained from all the co-authors.

Author's contribution for this section (4.2) was related to the intense collaboration with Vincent Richard when designing mathematical constrains for knee model development. In addition, author's thesis also worked at manuscript preparation.

4.2.1. Introduction

The MBO procedure (Section 2.4) traditionally implies an underlying kinematic model of each joint. Each joint model can be characterised by different types of constraints (Section 2.2.1.1.1). The accuracy of the estimated joint kinematics is still under debate (Andersen et al., 2009; Clément et al., 2014; Li et al., 2012; Stagni et al., 2009), and it depends on how biofidelic the joint constraints are.

Two ways of improvement are therefore possible. On the one hand, the construction of subject-specific joint constraints has been already investigated (Clément et al., 2014; Scheys et al., 2011) with promising results. However, the use of Magnetic Resonance Imaging (MRI), bi-planar fluoroscopy or bi-planar radiography is cumbersome. Therefore customised rather than personalised joint constraints have been also obtained by multi-body optimisation methods that include the identification of the model geometrical parameters (Andersen et al., 2010; Reinbolt et al., 2005). On the other hand, the introduction of "soft" constraints through a penalty-based method have been proposed (Gasparutto et al., 2015) to allow considering knee deformable ligaments and better adapt the joint constraints to task and inter-subject differences. It is interesting to notice that the used of "soft" constraints has been proposed not only for the lower limb (deformable ligaments) but also for the upper limb (Bolsterlee et al., 2014; Charbonnier et al., 2014) with the objective of balancing between joint restraints and bone pose tracking. Such "soft" constraints may provide better results than "hard" constraints, like spherical joints, hinge joints or parallel mechanisms.

Making an analogous use of "soft" constraints is possible introducing into the MBO another potential tool for modelling the osteoarticular structures: the joint stiffness matrix. Various notions of stiffness have been used in the literature, and a vocabulary was proposed to discriminate the different spring-like systems according

to the physical nature of the system and the method of measurement (Latash and Zatsiorsky, 1993). In this chapter, stiffness is defined as the characteristic of a 6DoFs elastic system, for which elastic forces provide resistance to the external force, measured at equilibrium without energy dissipation. This part of the thesis aims to characterise the knee joint restraints by their elastic energy derived from the 6DoFs stiffness matrix. Minimising the deformation energy may provide a satisfactory kinematics estimate, whose accuracy should at least be equivalent to the usual models (i.e., spherical joints, hinge joints and parallel mechanisms).

The performance of the stiffness matrix method was compare with other more traditional methods for MBO on stair-ascent data using *in vivo* stereophotogrammetric input measurement of skin marker trajectories while bone poses measured using bi-planar fluoroscopy served as a "gold standard".

4.2.2. Material and methods

4.2.2.1. Multi-body optimisation

The generic MBO method has been formally introduced in Chapter 2. When focusing on the knee joint, further details need to be introduced, which will be presented in this section. Adding these specifics to the general problem may result in some repetitions of concepts previously expressed, reiterated in this section in the attempt of increasing the clarity of the description.

MBO is a constrained minimisation of the sum of squared distances between experimental and model-derived skin-marker positions. Motor constraints ($\mathbf{\Phi}^m$) are used to represent these distances (Duprey et al., 2010). Specific nomenclature and symbols used in this section (4.2.) are presented in Table 4.6 and Table 4.7, respectively. The MBO was applied to the two segments of thigh and shank. The design variables of the optimisation are the natural coordinates (de Jalon et al., 1994; Dumas and Chèze, 2007), $\mathbf{Q}_i$, consisting, for each body segment i, of two position vectors (proximal (P_i) and distal (D_i) endpoints of the segment) and two unitary direction vectors ($\mathbf{u}_i$ perpendicular to the frontal plane of the segment and $\mathbf{w}_i$ aligned with the mean functional axis of extension/flexion of the distal joint) defining the

position and orientation of both segments: $\mathbf{Q}_i = \left[\mathbf{u}_i\ \mathbf{r}_{P_i}\ \mathbf{r}_{D_i}\ \mathbf{w}_i\right]^T$. These natural coordinates are presented in the global (inertial) coordinate system referred to as ICS (Figure 4.5). Each segment, defined by 12 parameters representing the 6DoFs, is characterised by the rigid body constraints, $\mathbf{\Phi}^r$ (Dumas and Chèze, 2007).

Nomenclature

ICS	Inertial coordinate system
JCS	Joint coordinate system
EF	Extension/Flexion
AA	Adduction/Abduction
IER	Internal/External rotation
LM	Lateral/Medial displacement
AP	Anterior/Posterior displacement
PD	Proximal/Distal displacement
N	No joint model
S	Spherical model
P	Parallel mechanism
M	Elastic joint model

Table 4.6 – Nomenclature specification for the current section.

Symbols

i	Body segment (i=3: shank; i=4: thigh)
$\boldsymbol{D_i}$	Generalised coordinates of segment i
$\boldsymbol{B_i}$	Constant transformation matrix
P_i	Proximal endpoint of segment i
D_i	Distal endpoint of segment i
$\boldsymbol{u_i}$	Unitary direction vector of segment *i*
$\boldsymbol{r}_{P_i}$	Coordinates of the proximal endpoint of segment *i*
$\boldsymbol{r}_{D_i}$	Coordinates of the distal endpoint of segment *i*
$\boldsymbol{w_i}$	Unitary direction vector of segment *i*
$\boldsymbol{\Phi^m}$	Motor constraints
$\boldsymbol{\Phi^k}$	Kinematic constraints
$\boldsymbol{\Phi^r}$	Rigid-body constraints
f	Objective function
S	Stuffiness matrix
U	Actual joint angles and displacements
U_0	Neutral joint angles and displacements
F	Actual forces and moments
F_0	Neutral fates and moments
θ_1	Extension/flexion angle(degree)
θ_2	Adduction/abduction angle (degree)
θ_3	Internal/external rotation angle (degree)
d_1	Lateral/medial displacement (mm)
d_2	Anterior/posterior displacement (mm)
d_3	Proximal/distal displacement (mm)
$\boldsymbol{e}_1$	First vector of knee joint coordinate system
$\boldsymbol{e}_2$	Second vector of knee joint coordinate system
$\boldsymbol{e}_3$	Third vector of knee joint coordinate system

Table 4.7 – Symbols included in the current section.

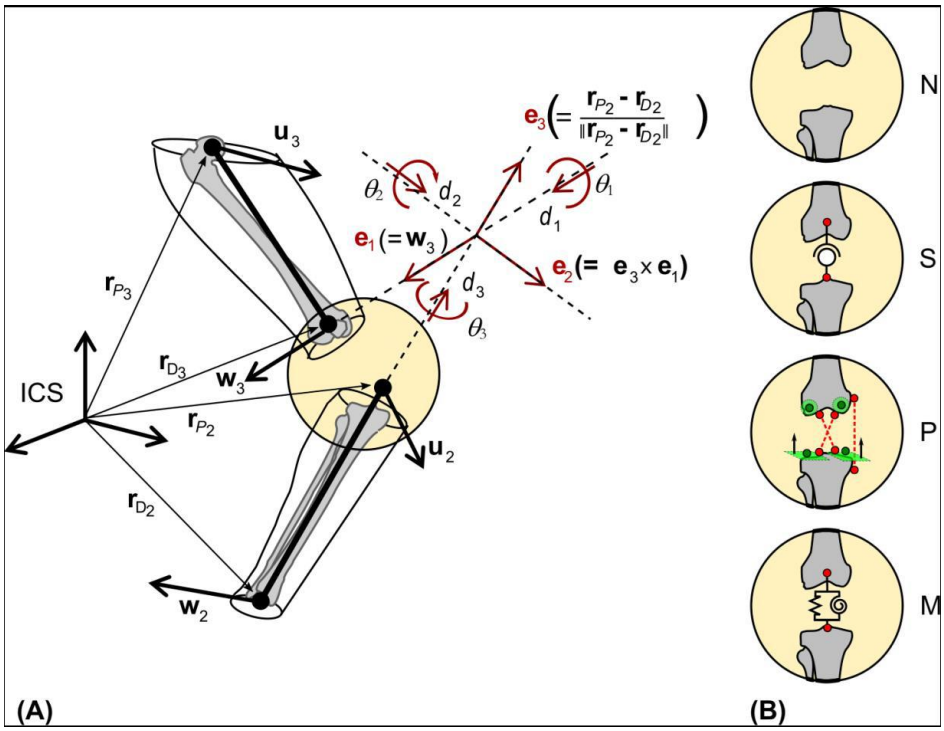

Figure 4.5 – Model specifications. (A) Generalised coordinates, Q_i, for thigh ($i=3$) and shank ($i=2$) and knee joint coordinate system. (B) Representation of the four different knee joint models, from top to bottom: no joint model (N), spherical model (S), parallel mechanism (P), and stiffness matrix (M). Obtained from Richard et al., (2016).

Kinematic constraints ($\mathbf{\Phi}^k$) can also be defined in different ways for the knee joint. The first knee joint model considers no constraint at the knee (N). This represents a special case of MBO, namely single-body optimisation (SBO) for thigh and shank, comparable to a classic least squares bone pose estimation (Soderkvist and Wedin, 1993). The MBO is defined by:

$$\min_{\mathbf{Q}} f = \frac{1}{2}\left[\mathbf{\Phi}^m\right]^T \mathbf{\Phi}^m \quad \text{subject to } \mathbf{\Phi}^r = \mathbf{0} \tag{4.5}$$

The second knee joint model is defined as a spherical joint (S) (Lu and O'Connor, 1999), and the third as a parallel mechanism (P) (Duprey et al., 2010). For these cases, the MBO is:

$$\min_{\mathbf{Q}} f = \frac{1}{2}\left[\mathbf{\Phi}^m\right]^T \mathbf{\Phi}^m \quad \text{subject to } \begin{cases} \mathbf{\Phi}^k = \mathbf{0} \\ \mathbf{\Phi}^r = \mathbf{0} \end{cases} \tag{4.6}$$

The fourth knee joint model presented in here is based on the stiffness matrix (M). Accordingly to this innovative model, the MBO is changed to add a deformation energy term:

$$\min_{\mathbf{Q}} f = \frac{1}{2}\left(\left[\mathbf{\Phi}^m\right]^T \mathbf{\Phi}^m + w\left[\mathbf{U}-\mathbf{U_0}\right]^T \mathbf{S}\left[\mathbf{U}-\mathbf{U_0}\right]\right) \quad \text{subject to } \mathbf{\Phi}^r = \mathbf{0} \tag{4.7}$$

where $\mathbf{U}$-$\mathbf{U_0}$ is the difference between current and neutral joint angles and displacements, $\mathbf{S}$ is the stiffness matrix, and w is a weighting factor.

In this study, the decision to impose the same order of magnitude on both terms of the objective function resulted in arbitrarily weighting the deformation energy term by a factor w set to 10^{-8}. The actual joint angles and displacements, $\mathbf{U} = [\theta_1\ \theta_2\ \theta_3\ d_1\ d_2\ d_3]^T$, are computed from the natural coordinates $\mathbf{Q}$ (Dumas et al., 2012) and correspond respectively to extension/flexion (EF), adduction/abduction (AA), and internal/external rotation (IER) angles and lateral/medial (LM), anterior/posterior (AP), and proximal/distal (PD) displacements. The objective is to conform to the joint coordinate system (JCS) definition ($\mathbf{e_1}$, $\mathbf{e_2}$, $\mathbf{e_3}$) (Wu et al., 2002). To achieve consistency, the same axis definitions were used for MBO, stiffness matrix determination, and processing of validation data (Figure 4.5).

Knee joint movements (relative motion between tibia and femur segment coordinate system - SCSs) were expressed following the recommendations of the ISB (Wu et al., 2002), which resulted in a direct relation between the natural coordinates, $\mathbf{Q}_i$, and the SCS axes:

$$\mathbf{R}_0^i = \left[\mathbf{X}_i \quad \mathbf{Y}_i \quad \mathbf{Z}_i\right] = \left[\mathbf{u}_i \quad \mathbf{r}_{P_i} \quad \mathbf{r}_{D_i} \quad \mathbf{w}_i\right]\left[\mathbf{B}_i\right]^{-1} \tag{4.8}$$

with $\mathbf{B}_i$ a constant transformation matrix (Dumas and Chèze, 2007).

In particular, knee JCS was built by alignment of tibia and femur SCS axis in static position acquired during the calibration phase. The so-called aligned JCS was constructed as follows:

$$\mathbf{R}_4^3 = \left[\mathbf{R}_0^4\right]^{-1}\left[\mathbf{R}_0^3\mathbf{A}^3\right] \tag{4.9}$$

where $\mathbf{R}_4^3$ is the rotation matrix defining the attitude of the tibia SCS with respect to the femur SCS, $\mathbf{R}_0^3$ is the rotation matrix defining the attitude of the tibia SCS with respect to the ICS (directly related to the natural coordinates Q2) and $\mathbf{R}_0^4$ is the rotation matrix defining the attitude of the femur SCS with respect to the ICS (directly related to the natural coordinates Q3). The alignment of both SCSs in static position is obtained by the matrix $\mathbf{A}^3$ consisting of the coordinates of the X, Y and Z axes of the tibia SCS in static position expressed in the femur SCS (Hagemeister et al., 2011).

4.2.2.2. Knee stiffness matrix

The stiffness matrix includes the relation between the joint passive forces and moments **F** and the joint angles and displacements. The stiffness matrix follows the general equation $\mathbf{F}-\mathbf{F_0}=\mathbf{S}\left(\mathbf{U}-\mathbf{U_0}\right)$. As detailed above (4.1.2.2.), both loads and the imposed displacements were measured in the JCS ($\mathbf{e_1}$, $\mathbf{e_2}$, $\mathbf{e_3}$).

The present method relies on a single and constant stiffness matrix, **S**, of the more extensive cadaveric experiments performed (Section 4.1.3.). The symmetrical stiffness matrix, obtained by inverting the computed compliance matrix of the intact specimen at 45° EF angle (Table 4.4), is given by:

$$\mathbf{S}=\begin{bmatrix} 869.5 & 2733 & 154.2 & 55.88 & -22.45 & 81.57 \\ & 8819 & 331.4 & 174.8 & -73.83 & 250.5 \\ & & 129.7 & 10.36 & -1.453 & 18.48 \\ & & & 3.895 & -1.620 & 5.330 \\ & \textit{Sym} & & & 1.246 & -1.864 \\ & & & & & 8.063 \end{bmatrix}\times 10^2 \qquad 4.10$$

The neutral position obtained experimentally is a position with minimum loads and does not imply null joint angles and displacements. The neutral joint angles and displacements were $\mathbf{U_0}=\left[46.59\ -4.79\ 11.68\ -1.64\ 3.21\ 4.80\right]^T$. The units for joint angles and displacements are degrees (°) and mm. However, in order not to penalise EF in Equation 4.7, the neutral value was replaced by the actual joint angle,

θ_1. **S** was therefore reduced to the first five columns and lines of the matrix, taking no account of the coefficients relative to EF angle.

4.2.2.3. Validation data and procedure

Participants in the *in vivo* stair climbing experiments provided informed written consent to participate in the study and ethical approval was granted by the Institutional Human Research Ethics Committee (National Taiwan University, Institute of Biomedical Engineering, Taipei, Taiwan). Stair-ascent data were collected on two healthy male subjects. The age, height and mass of subjects S1 and S2 were 21 and 20 years, 176 and 164 cm and 84 and 59 kg, respectively. The trajectories of 10 skin markers on the right thigh (4 markers at mid-thigh and 2 on the medial and lateral epicondyles) and shank (1 marker each at the head of the fibula, tibial tuberosity and medial and lateral malleoli) were recorded using a 7-camera stereophotogrammetry system (Vicon, Oxford Metrics, UK), operated at 60 samples per second. Simultaneously, bone pose was recorded with bi-planar fluoroscopy. The frequency of acquisition of the fluoroscopes (with a 1020x932 image resolution) was 30 samples per second. Stereophotogrammetric and fluoroscopic data was acquired under the same experimental conditions (same protocol, laboratory, marker set, fluoroscopy registration method, movement) as in Tsai et al. (Tsai et al., 2011). The performance of the registration method using bi-planar fluoroscopy has been shown to be highly accurate: 0.24 ± 0.77 mm for in-plane translations, 0.41 ± 3.06 mm for out-of-plane translations and 0.59 ± 1.13° for all rotations (Tsai et al., 2011).

MBO was performed using skin markers, while reference kinematics was computed from bi-planar fluoroscopy. Calibration of the reference position of the skin markers with respect to the femur and tibia was performed in a static position maintained by the subject at the beginning of the measurement session. The tibia and femur SCSs were considered to be coincident in the static position, as explained in the section *Multi-body optimisation*. The coordinate systems based on 3D bone geometry were defined in the same way as on the cadaver knee (Figure 4.1B).

4.2.2.4. Sensitivity

A sensitivity analysis addresses the variability of coefficients that characterise the proposed stiffness matrix using statistical distributions, and extends this variability to the tibiofemoral kinematics estimation using the MBO method proposed here. Since the stiffness matrix applied to two different subjects was computed from experimental measurements involving a single cadaveric knee at 45° of flexion, there are several potential sources of variability. For instance, the influence of loading conditions needs to be evaluated: the compliance matrix considered a single loading condition (almost unloaded condition), while the stair-climbing movement performed by the subjects involved varying knee loading conditions. The stiffness matrix contains a total of 25 coefficients, but only 15 parameters (5 diagonal terms and 10 extra-diagonal terms) were considered, since the stiffness matrix is symmetric. The sensitivity analysis consisted of perturbing the above-mentioned 15 coefficients using a Gaussian statistical distribution. The means of the distributions for the coefficients were assumed to be the stiffness matrix coefficients determined at 45° of flexion. A Latin hypercube sampling (LHS) method was used (El Habachi et al., 2015) to generate a set of 1.6e6 samples of perturbed coefficients. We tested for positive definiteness of the generated stiffness matrix in order to discard non-complying matrices. Finally, a run of 511 MBOs was performed, in keeping with the number of runs in previous sensitivity studies using LHS (Martelli et al., 2015; Valente et al., 2014). The influence on the model-derived tibiofemoral kinematics was analysed. Joint angles and displacements estimated through MBO for the perturbed samples of stiffness matrix were represented by the mean of the kinematics estimations over the 511 runs. Two corridors of 1 and 1.96 sd respectively around the mean value illustrate how the perturbation extends to the kinematics. For consistency of the weighting factor *w* used for the deformation energy term in the MBO, each of the perturbed stiffness matrices was scaled with respect to the initial stiffness matrix defined at 45° of flexion using the ratio of traces. The formulation of the problem becomes:

$$\min_{\mathbf{Q}} f = \frac{1}{2}\left(\left[\mathbf{\Phi}^m\right]^T \mathbf{\Phi}^m + \left[w \cdot tr\left(\mathbf{S}\right)\right]\left[\mathbf{U}-\mathbf{U_0}\right]^T \left[\mathbf{S}^*/tr\left(\mathbf{S}^*\right)\right]\left[\mathbf{U}-\mathbf{U_0}\right]\right) \quad \text{4.11}$$

$$\text{subject to } \mathbf{\Phi}^r = \mathbf{0}$$

where **S** is the initial stiffness matrix determined at 45° of flexion and **S*** is a perturbed stiffness matrix, and *tr* stands for the trace of the matrix.

4.2.3. Results

4.2.3.1. Comparative study

Model-derived kinematics for each knee joint model (N, S, P, and M), compared to reference kinematics for both subjects are shown in Figure 4.6.

It should be noted that a generally satisfactory estimation of kinematics with model M is obtained around 45° of flexion, closest to the stiffness matrix conditions (see the vertical orange line of Figure 4.6, where 45° of flexion occurs once at about 35% of the Stair-ascent Cycle).

4.2.3.2. Sensitivity

The elastic joint model-derived kinematics embedding the initial stiffness matrix (M), as well as the mean ($\bar{\mathbf{M}}^*$) and corridors of 1 ($\bar{\mathbf{M}}^* \pm \mathrm{sd}$) and 1.96 ($\bar{\mathbf{M}}^* \pm 1.96\,\mathrm{sd}$) standard deviation of the elastic joint model-derived kinematics embedding the perturbed stiffness matrix, were computed for both subjects (Figure 4.6). The corridors were narrow for joint angles, with a maximum sd of 1.4° for FE and IER in subject S2, particularly for AA (0.7° for S1 and 0.9° for subject S2). Larger corridor amplitudes were observed for displacements, with a maximum sd for AP of 4.2mm in both subjects S1 and S2. A significant difference was observed in patterns and values between the angles and displacements obtained with the initial stiffness matrix M (cyan in Figure 4.6) and the mean over the 511 runs on joint angles and displacements obtained with the perturbed stiffness matrices $\bar{\mathbf{M}}^*$ (dark blue in Fig 2). Curves for model M were generally within the corridor $\bar{\mathbf{M}}^* \pm 1.96\,\mathrm{sd}$, except for LM and PD in subject S2.

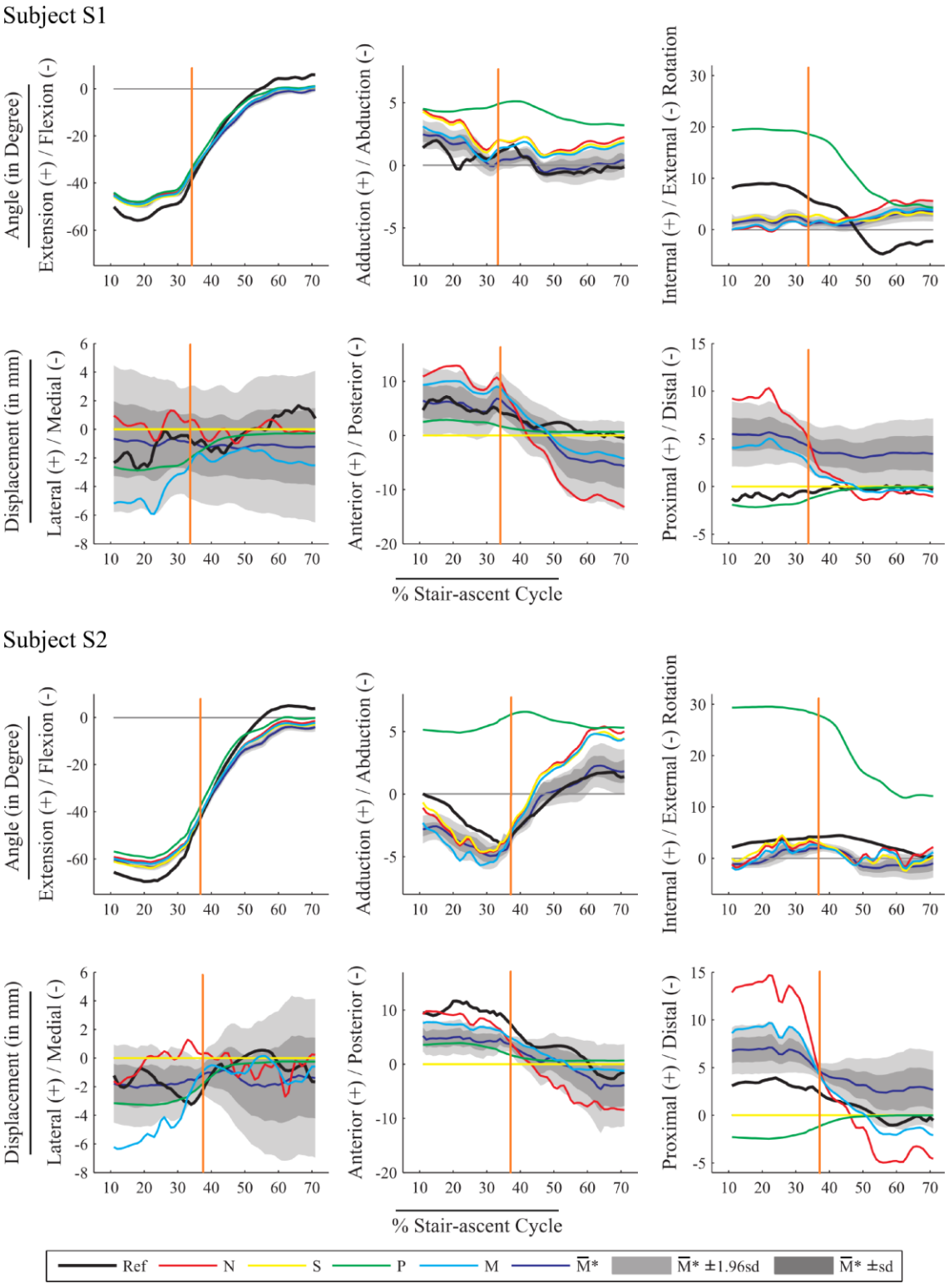

Figure 4.6 - Knee joint angles and displacements, $U = [\theta 1\ \theta 2\ \theta 3\ d1\ d2\ d3]^T$ for both subjects. Model-derived kinematics estimated with the four different knee joint models: no joint model (N, red), spherical model (S, yellow), parallel mechanism (P, green), and stiffness matrix (M, cyan) plotted against fluoroscopy-based kinematics (Ref, black). Sensitivity analysis results are represented by the mean of the kinematics estimation over the 511 runs of MBO embedding perturbed stiffness matrices (dark blue), with corridor representing the variation in the estimation for one standard deviation (light grey) and 1.96

standard deviation (dark grey) around the mean value. The vertical orange line represents the flexion angle in which the stiffness matrix was calibrated ex vivo. Adapted from Richard et al., (2016).

4.2.4. Discussion

Reported results showed that the elastic joint can be considered an alternative to other joint models used in the assessment of knee joint kinematics, although none of the methods tested actually provides an accurate 3D kinematics estimation. Whatever the knee model adopted, good accuracy is shown only for a limited number of joint angles and displacements.

Results showed that accurate knee kinematics can only be obtained by introducing joint constraints and performing multi-body optimisation. Overall, the method with model N leads to poor agreements compared to the reference, with the exception of EF and LM. Kinematics estimation obtained from MBO with model N (i.e., SBO) reflects most of the STA, since there are no constraints to compensate for it. The introduction of "soft" constraints based on the joint stiffness matrix proved to represent a promising trade-off. The results for model M indicate that more physiological joint models are relevant. Overall, better agreement with the reference is obtained with model M (and with model S) than with model N (additional analysis and details on Richard et al., 2016). This confirms that minimising deformation energy represents at least an equally accurate alternative to the classic kinematic constraints (N and S) for estimating knee joint angles such as EF and IER. The model based on the stiffness matrix also seems to estimate displacements efficiently (in particular for AP and PD) compared to model P. The advantage of characterising the knee joint by a stiffness matrix is the ability to define coupling between DoFs (i.e., extra-diagonal terms) and to consider "soft" constraints. The drawback lies in introducing a penalty-based method where the choice of weight factor w is critical. Here, in order to minimise errors on both skin marker trajectories and deformation energy, we chose to consider a similar contribution to the objective function for both terms. It would be possible to consider "softer" or "harder" constraints by adjusting the weighting factor.

This study is limited by the small number of subjects it considers. Moreover, the MBO method was applied to only two segments. However, as in other validation studies, reference kinematics data were available for thigh and shank only (Andersen et al., 2010; Gasparutto et al., 2015). Further, the stiffness matrix was derived from a single cadaveric specimen. Such *in vivo* validation data and *ex vivo* modelling data are obviously difficult to obtain. Yet while the inter-subject variability is not representative with only two subjects, it confirms the feasibility of the method. Previous validation studies of MBO against fluoroscopy or pin data have been performed on two (Stagni et al., 2009) to ten (Clement et al., 2015; Li et al., 2012) subjects. Previous knee joint models, such as parallel mechanisms, have also been developed using data gathered from one cadaveric knee (Gasparutto et al., 2015).

Moreover, the use of a constant stiffness matrix was chosen to focus attention on the feasibility of such joint modelling. This choice is supported by the results of a sensitivity analysis (Figure 4.6), showing that varying the stiffness matrix coefficients does not significantly affect the performance of the method. Nonetheless, the consequence of using a single stiffness matrix obtained at 45° of flexion is a good estimation of kinematics at this specific knee position.

Future implementation, based on the use of bilinear stiffness matrix (i.e. a matrix including different stiffness coefficients for opposite joint movement and especially for proximal/distal displacement) or angle-dependent stiffness (similarly to previously proposed angle-dependent ligament length variation (Bergamini et al., 2011)), may lead to more accurate estimation of the knee joint kinematics. In addition, using a ligament-deficient stiffness matrix (Section 4.1.3.) to apply MBO to data from pathological subjects could be another solution.

To conclude, improvement of the MBO accuracy and further personalisation can be achieved with a more physiological representation of the knee joint within models. In that regard, this study opened the way to an alternative to the use of deterministic constraints in the multi-body method. The more physiological constraints implied by a penalty-based method (referred to as “soft” constraints) are a first progress toward making models more subject-specific. Further development in this sense will be presented in the following Chapters.

References

Al Nazer, R., Rantalainen, T., Heinonen, a, Sievänen, H., Mikkola, a, 2008. Flexible multibody simulation approach in the analysis of tibial strain during walking. J. Biomech. 41, 1036–43.

Amankwah, K., Triolo, R.J., Kirsch, R., 2004. Effects of spinal cord injury on lower--limb passive joint moments revealed through a nonlinear viscoelastic model. J. Rehabil. Res. Dev. 41, 15–32.

Andersen, M., Damsgaard, M., Rasmussen, J., 2011. Force-dependent kinematics: a new analysis method for non-conforming joints. In: 13th International Symposium on Computer Simulation in Biomechanics. pp. 1–2.

Andersen, M., Rasmussen, J., 2011. Total knee replacement musculoskeletal model using a novel simulation method for non-conforming joints. In: Proceedings of the International Society of Biomechanicsof the International Society of Biomechanics. pp. 1–2.

Andersen, M.S., Benoit, D.L., Damsgaard, M., Ramsey, D.K., Rasmussen, J., 2010. Do kinematic models reduce the effects of soft tissue artefacts in skin marker-based motion analysis? An in vivo study of knee kinematics. J. Biomech. 43, 268–73.

Andersen, M.S., Damsgaard, M., Rasmussen, J., 2009. Kinematic analysis of over-determinate biomechanical systems. Comput. Methods Biomech. Biomed. Engin. 12, 371–384.

Anderson, F.C., Pandy, M.G., 2001. Dynamic Optimization of Human Walking. J. Biomech. Eng. 123, 381–390.

Arnold, E.M., Ward, S.R., Lieber, R.L., Delp, S.L., 2010. A model of the lower limb for analysis of human movement. Ann. Biomed. Eng. 38, 269–79.

Baldwin, M. a, Clary, C.W., Fitzpatrick, C.K., Deacy, J.S., Maletsky, L.P., Rullkoetter, P.J., 2012. Dynamic finite element knee simulation for evaluation of knee replacement mechanics. J. Biomech. 45, 474–83.

Bendjaballah, M.Z., Shirazi-Adl, a., Zukor, D.J., 1998. Biomechanical response of the passive human knee joint under anterior-posterior forces. Clin. Biomech. (Bristol, Avon) 13, 625–633.

Bergamini, E., Pillet, H., Hausselle, J., Thoreux, P., Guerard, S., Camomilla, V., Cappozzo, a, Skalli, W., 2011. Tibio-femoral joint constraints for bone pose estimation during movement using multi-body optimization. Gait Posture 33, 706–11.

Beynnon, B., Yu, J., Huston, D., Fleming, B., Johnson, R., Haugh, L., Pope, M.H., 1996. A sagittal plane model of the knee and cruciate ligaments with application of a sensitivity analysis. J. Biomech. Eng. 118, 227–39.

Bolsterlee, B., Veeger, H.E.J., van der Helm, F.C.T., 2014. Modelling clavicular and scapular kinematics: from measurement to simulation. Med. Biol. Eng. Comput. 52, 283–91.

Charbonnier, C., Chagué, S., Kolo, F.C., Chow, J.C.K., Lädermann, a, 2014. A patient-specific measurement technique to model shoulder joint kinematics. Orthop. Traumatol. Surg. Res. 100, 715–9.

Christophy, M., Curtin, M., Faruk Senan, N.A., Lotz, J.C., O'Reilly, O.M., 2013. On the modeling of the intervertebral joint in multibody models for the spine. Multibody Syst. Dyn. 30, 413–432.

Christophy, M., Faruk Senan, N.A., Lotz, J.C., O'Reilly, O.M., 2012. A Musculoskeletal model for the lumbar spine. Biomech. Model. Mechanobiol. 11, 19–34.

Clement, J., Dumas, R., Hageimester, N., De Guise, J. a., 2015. Soft tissue artefacts compensation in knee kinematics by multi-body optimization: performance of subject-specific knee joint models. J. Biomech. 48, 3796–3802.

Clément, J., Hagemeister, N., Dumas, R., Kanhonou, M., de Guise, J.A., 2014. Influence of biomechanical multi-joint models used in global optimisation to estimate healthy and osteoarthritis knee kinematics. Comput. Methods Biomech. Biomed. Engin. 17, 76–77.

de Jalon, J.G., Cuadrado, J., Avello, A., Jimenez, J.M., 1994. Kinematic and Dynamic Simulation of Rigid and Flexible Systems with Fully Cartesian Coordinates. In: Seabra Pereira, M.O., Ambrósio, J.C. (Eds.), Computer-Aided Analysis of Rigid and Flexible Mechanical Systems SE - 9, NATO ASI Series. Springer Netherlands, pp. 285–323.

Di Gregorio, R., Parenti-Castelli, V., 2003. A Spatial Mechanism With Higher Pairs for Modelling the Human Knee Joint. J. Biomech. Eng. 125, 232–7.

Donahue, T.L.H., Hull, M.L., Rashid, M.M., Jacobs, C.R., 2002. A finite element model of the human knee joint for the study of tibio-femoral contact. J. Biomech. Eng.

Dumas, R., Chèze, L., 2007. 3D inverse dynamics in non-orthonormal segment coordinate system. Med. Biol. Eng. Comput. 45, 315–22.

Dumas, R., Robert, T., Pomero, V., Cheze, L., 2012. Joint and segment coordinate systems revisited. Comput. Methods Biomech. Biomed. Engin. 15, 183–185.

Duprey, S., Cheze, L., Dumas, R., 2010. Influence of joint constraints on lower limb kinematics estimation from skin markers using global optimization. J. Biomech. 43, 2858–2862.

Eagar, P., Hull, M.L., Howell, S.M., 2001. A method for quantifying the anterior load-displacement behavior of the human knee in both the low and high stiffness regions. J. Biomech. 34, 1655–60.

El Habachi, A., Moissenet, F., Duprey, S., Cheze, L., Dumas, R., 2015. Global sensitivity analysis of the joint kinematics during gait to the parameters of a lower limb multi-body model. Med. Biol. Eng. Comput. 655–667.

Fernandez, J.W., Pandy, M.G., 2006. Integrating modelling and experiments to assess dynamic musculoskeletal function in humans. Exp. Physiol. 91, 371–82.

Fox, R.J., Harner, C.D., Sakane, M., Carlin, G.J., Woo, S.L., 1998. Determination of the in situ forces in the human posterior cruciate ligament using robotic

technology. A cadaveric study. Am. J. Sports Med. 26, 395–401.

Fujie, H., Livesay, G., Fujita, M., Woo, S., 1996. Forces and moments in six-DOF at the human knee joint: mathematical description for control. J. Biomech. 29, 1577–1585.

Fujie, H., Mabuchi, K., Woo, S., 1993. The use of robotics technology to study human joint kinematics: a new methodology. J. Biomech. Eng. 115, 211–7.

Fujie, H., Sekito, T., Orita, A., 2004. A novel robotic system for joint biomechanical tests: application to the human knee joint. J. Biomech. Eng. 126, 54–61.

Gardner-Morse, M.G., Stokes, I. a. F., 2004. Structural behavior of human lumbar spinal motion segments. J. Biomech. 37, 205–212.

Gasparutto, X., Sancisi, N., Jacquelin, E., Parenti-Castelli, V., Dumas, R., 2015. Validation of a multi-body optimization with knee kinematic models including ligament constraints. J. Biomech. 48, 1141–1146.

Grood, E., 1988. Limits of movement in the human knee. Effect of sectioning the posterior cruciate ligament and posterolateral structures. J Bone Jt. Surg Am 88–97.

Guess, T.M., Thiagarajan, G., Kia, M., Mishra, M., 2010. A subject specific multibody model of the knee with menisci. Med. Eng. Phys. 32, 505–15.

Hagemeister, N., Senk, M., Dumas, R., Chèze, L., 2011. Effect of axis alignment on in vivo shoulder kinematics. Comput. Methods Biomech. Biomed. Engin. 14, 755–61.

Halloran, J.P., Petrella, A.J., Rullkoetter, P.J., 2005. Explicit finite element modeling of total knee replacement mechanics. J. Biomech. 38, 323–31.

Haut, R.C., Powlison, A.C., 1990. The effects of test environment and cyclic stretching on the failure properties of human patellar tendons. J. Orthop. Res. 8, 532–540.

Hsieh, H.-J., Hu, C.-C., Lu, T.-W., Kuo, M.-Y., Kuo, C.-C., Hsu, H.-C., n.d. Evaluation of Three Force-Position Hybrid Control Methods for a Robot-Based Biological Joint Testing System. Submitt. to Biomed. Eng. Online.

Hsieh, H.J., Hu, C.C., Lu, T.W., Kuo, M.Y., Hsu, H.C., 2016. Evaluation of three force-position hybrid control methods for a robot-based biological joint testing system. Biomed. Eng. Online 15, 62–91.

Hu, C.-C., Lu, T.-W., Chen, S.-C., 2013. Influence of model complexity and problem formulation on the forces in the knee calculated using optimization methods. Biomed. Eng. Online 12, 20.

Kanamori, A., Woo, S.L., Ma, C.B., Zeminski, J., Rudy, T.W., Li, G., Livesay, G. a, 2000. The forces in the anterior cruciate ligament and knee kinematics during a simulated pivot shift test: A human cadaveric study using robotic technology. Arthroscopy 16, 633–9.

Kazemi, M., Dabiri, Y., Li, L.P., 2013. Recent advances in computational mechanics of the human knee joint. Comput. Math. Methods Med. 2013, 718423.

Kim, K., Kim, Y.H., Lee, S., 2012. General computational model for human musculoskeletal system of spine. J. Appl. Math. 2012, 1–8.

Koell, P., Cheze, L., Dumas, R., 2010. Prediction of internal spine configuration from external measurements using a multi-body model of the spine. Comput. Methods Biomech. Biomed. Engin. 13, 79–80.

Lamberto, G., Richard, V., Dumas, R., Valentini, P.P., Pennestrì, E., Lu, T.W., Camomilla, V., Cappozzo, A., 2016. Modeling the human tibio-femoral joint using ex vivo determined compliance matrices. J. Biomech. Eng. 138, In press.

Latash, M.L., Zatsiorsky, V.M., 1993. Joint stiffness: Myth or reality? Hum. Mov. Sci. 12, 653–692.

Li, G., Gil, J., Kanamori, a, Woo, S.L., 1999. A validated three-dimensional computational model of a human knee joint. J. Biomech. Eng.

Li, K., Zheng, L., Tashman, S., Zhang, X., 2012. The inaccuracy of surface-measured model-derived tibiofemoral kinematics. J. Biomech. 45, 2719–23.

Loch, D. a, Luo, Z.P., Lewis, J.L., Stewart, N.J., 1992. A theoretical model of the knee and ACL: theory and experimental verification. J. Biomech. 25, 81–90.

Lu, T.-W., O'Connor, J.J., 1999. Bone position estimation from skin marker co-ordinates using global optimisation with joint constraints. J. Biomech. 32, 129–134.

Marin, F., Hoang, N., Aufaure, P., Ho Ba Tho, M.C., 2010. In vivo intersegmental motion of the cervical spine using an inverse kinematics procedure. Clin. Biomech. 25, 389–396.

Markolf KL, Mensch, J., Amstutz, H., 1976. Stiffness and laxity of the knee -the contributions of the supporting structures. J. Bone Joint Surg. Am. 58, 583–94.

Marouane, H., Shirazi-Adl, A., Adouni, M., 2015. Knee joint passive stiffness and moment in sagittal and frontal planes markedly increase with compression. Comput. Methods Biomech. Biomed. Engin. 18, 339–350.

Martelli, S., Valente, G., Viceconti, M., Taddei, F., 2015. Sensitivity of a subject-specific musculoskeletal model to the uncertainties on the joint axes location. Comput. Methods Biomech. Biomed. Engin. 18, 1555–1563.

Moissenet, F., Chèze, L., Dumas, R., 2014. A 3D lower limb musculoskeletal model for simultaneous estimation of musculo-tendon, joint contact, ligament and bone forces during gait. J. Biomech. 47, 50–8.

Mokhtarzadeh, H., Perraton, L., Fok, L., Muñoz, M.A., Clark, R., Pivonka, P., Bryant, A.L., 2014. A comparison of optimisation methods and knee joint degrees of freedom on muscle force predictions during single-leg hop landings. J. Biomech. 47, 2863–2868.

Most, E., Axe, J., Rubash, H., Li, G., 2004. Sensitivity of the knee joint kinematics calculation to selection of flexion axes. J. Biomech. 37, 1743–8.

Noyes, F.R., Grood, E.S., 1976. The strength of the anterior cruciate ligament in humans and Rhesus monkeys. J. Bone Joint Surg. Am. 58, 1074–82.

Ottoboni A, Parenti-Castelli V, Sancisi N, Belvedere C, L.A., 2010. Articular surface approximation in equivalent spatial parallel mechanism models of the human knee joint: an experiment-based assessment. In: Proc Inst Mech Eng H.

Peña, E., Calvo, B., Martínez, M. a, Doblaré, M., 2006. A three-dimensional finite

element analysis of the combined behavior of ligaments and menisci in the healthy human knee joint. J. Biomech. 39, 1686–701.

Pennestrì, E., Cheli, F., 2006. Cinematica e dinamica dei sistemi multibody (in italian), vol.1. Casa Editrice Ambrosiana, Milano, Italy.

Petit, Y., Aubin, C.E., Labelle, H., 2004. Patient-specific mechanical properties of a flexible multi-body model of the scoliotic spine. Med. Biol. Eng. Comput. 42, 55–60.

Reinbolt, J. a., Schutte, J.F., Fregly, B.J., Koh, B. Il, Haftka, R.T., George, A.D., Mitchell, K.H., 2005. Determination of patient-specific multi-joint kinematic models through two-level optimization. J. Biomech. 38, 621–626.

Ribeiro, A., Rasmussen, J., Flores, P., Silva, L.F., 2012. Modeling of the condyle elements within a biomechanical knee model. Multibody Syst. Dyn. 28, 181–197.

Richard, V., Lamberto, G., Lu, T.-W., Cappozzo, A., Dumas, R., 2016. Knee Kinematics Estimation Using Multi-Body Optimisation Embedding a Knee Joint Stiffness Matrix: A Feasibility Study. PLoS One 11, e0157010.

Sancisi, N., Parenti-Castelli, V., 2011. A sequentially-defined stiffness model of the knee. Mech. Mach. Theory 46, 1920–1928.

Scheys, L., Desloovere, K., Spaepen, A., Suetens, P., Jonkers, I., 2011. Calculating gait kinematics using MR-based kinematic models. Gait Posture 33, 158–64.

Shelburne, K.B., Torry, M.R., Pandy, M.G., 2005. Muscle, Ligament, and Joint-Contact Forces at the Knee during Walking. Med. Sci. Sport. Exerc. 37, 1948–1956.

Soderkvist, I., Wedin, P., 1993. Determining the Movement of the Skeleton using Well-Confgured Markers. J. Biomech. 26, 1473–1477.

Stagni, R., Fantozzi, S., Cappello, A., 2009. Double calibration vs. global optimisation: performance and effectiveness for clinical application. Gait Posture 29, 119–22.

Stokes, I. a, Gardner-Morse, M., Churchill, D., Laible, J.P., 2002. Measurement of a spinal motion segment stiffness matrix. J. Biomech. 35, 517–21.

Tsai, T.Y., Lu, T.W., Kuo, M.Y., Lin, C.C., 2011. Effects of soft tissue artifacts on the calculated kinematics and kinetics of the knee during stair-ascent. J. Biomech. 44, 1182–1188.

Valente, G., Pitto, L., Testi, D., Seth, A., Delp, S.L., Stagni, R., Viceconti, M., Taddei, F., 2014. Are Subject-Specific Musculoskeletal Models Robust to the Uncertainties in Parameter Identification? PLoS One 9, e112625.

Viidik, A., Sandqvist, L., Mägi, M., 1965. Influence of Postmortal Storage on Tensile Strength Characteristics and Histology of Rabbit Ligaments. Acta Orthop. Scand. 36, 3–38.

Woo, S., Orlando, C., Camp, J., Akeson, W., 1986. Effects of postmortem storage by freezing on ligament tensile behavior. J. Biomech.

Wu, G., Siegler, S., Allard, P., Kirtley, C., Leardini, A., Rosenbaum, D., Whittle, M., D'Lima, D.D., Cristofolini, L., Witte, H., Schmid, O., Stokes, I., 2002. ISB

recommendation on definitions of joint coordinate system of various joints for the reporting of human joint motion--part I: ankle, hip, and spine. J. Biomech. 35, 543–548.

Yamaguchi, G.T., Zajac, F.E., 1989. A planar model of the knee joint to characterize the knee extensor mechanism. J. Biomech. 22, 1–10.

Yang, N.H., Canavan, P.K., Nayeb-Hashemi, H., Najafi, B., Vaziri, A., 2010. Protocol for constructing subject-specific biomechanical models of knee joint. Comput. Methods Biomech. Biomed. Engin. 13, 589–603.

Zantop, T., Herbort, M., Raschke, M.J., Fu, F.H., Petersen, W., 2007. The role of the anteromedial and posterolateral bundles of the anterior cruciate ligament in anterior tibial translation and internal rotation. Am. J. Sports Med. 35, 223–7.

CHAPTER 5

A force-based approach to personalised tibiofemoral modelling

This chapter presents a method for personalising the tibiofemoral model presented in Chapter 4 using few easily detectable measures and data from clinical tests. This idea is presented in here on two *ex vivo* knee specimens, with the experimental work carried out at Flinders University (Adelaide, South Australia, Australia) as a proof of concept of the potential to transfer this idea to an *in vivo* scenario.

Author's contribution for this chapter was related to the design of the experimental protocol and the execution of the experiments in person. The experiments took place in Australia due an ongoing collaboration between Dr. Claudia Mazzà and Dr. Saulo Martelli, established in the recent years. Author's involvement was also in results post-processing, model development and analysis in MATLAB.

5.1. Introduction

The development of subject specific biomechanical models of the knee joint as computational tools is growing fast to support a number of applications, including clinical pre- and intra-operative assessment of joint replacement and ligament reconstruction. Personalised models can be generated using subject's specific anatomy of bones and/or soft tissues from medical images as well as using measured kinematics or forces.

Subject specific force data have been typically used in knee modelling aiming to either optimise model parameters or validate model predictions. Examples from the first category include recent papers, where *ex vivo* measurements of the laxity of intact knees were used to calibrate the ligament parameters (i.e. reference strain and

stiffness) for two finite element personalised models of the natural (Harris et al., 2016) and artificial joints (Ewing et al., 2016). Similarly, Guess et al., (2010) and (2011) used cadaveric force data and mathematical optimisation to improve the mechanical modelling of menisci and cartilage, respectively. The use of knee forces to validate model predictions is normally based on data from cadaveric specimens, as in the study of Kiapour et al., (2014). *In vivo* data have also been exploited to this purpose, as per the Grand Challenge Competition to Predict *in vivo* Knee Loads (Fregly et al., 2012). Finally, some studies used force datasets to tune model parameters as well as to validate model results. This is the case, for instance, of the recent *ex vivo* works of Kia et al., (2016) and of Mootanah et al., (2014), who first optimised ligament modelling and then validated the model predictions in terms of ligament forces and joint kinematics, and in terms of contact pressure distribution, respectively.

All the above force-based models strongly depend on a reliable and accurate representation of the anatomical structures, typically derived from medical images with expensive and time-consuming processes. Once their geometries are available, the mechanical behaviour of the various anatomical structures is determined using generic literature and/or *ad-hoc* experiments. This approach can lead to very accurate results (Kia et al., 2016; Kiapour et al., 2014), but has limited clinical applicability in a fast paced scenario where information are needed promptly to drive surgical intervention (Signorelli et al., 2016).

The forces transmitted by the interaction of passive structures (i.e. cartilage, menisci, ligaments), which play a crucial role in stabilising the joint and guiding the motion, can be quantified *in vivo* using knee laxity measurement instruments such as KT-1000 (Figure 5.1) or KT-2000 (Kupper et al., 2007; Shultz et al., 2007). These instruments have been proven to be reliable in clinics to diagnose ACL tear (Lin et al., 2011) and as such appear as good candidates to be used for the personalisation of a model that does not include the recording of the subject's anatomy. Recently Lorenz et al., (2015) attempted to measure the *in vivo* knee laxity using commercial robotic arm-based robots (Figure 5.2), finding reliable results from the internal rotation tests. Rotational laxity was also measured *in vivo* using a different instrument before and after the anterior cruciate ligament reconstruction following

the ligament rupture (Moewis et al., 2016). If a generic model providing a full characterisation of the knee mechanical behaviour in terms of coupling between loads and displacements was available, then the above instruments could be used for an *in vivo* low-cost personalisation of this model which would allow for improved surgical planning. With this long-term goal in mind, this study aims to develop a method to estimate personalised passive forces at the knee joint that does not rely on a subject's anatomy. The definition and validation of the model will be based on *ex vivo* measurements of the six DoFs force-displacement relationships. These will be represented in terms of a discrete set of compliance matrices as obtained both for the intact knee and after the sequential cut of three of the major ligaments, which can be updated for each subject with experimentally measured force data.

Figure 5.1 – Usage of the KT 1000 to measure the anterior knee laxity. Adapted from https://www.thekneedoc.co.uk/kt1000-knee-laxity-testing-device/. Full video available at: https://youtube.com/watch?v=QbhLPwmbgoY%26rel%3D0.

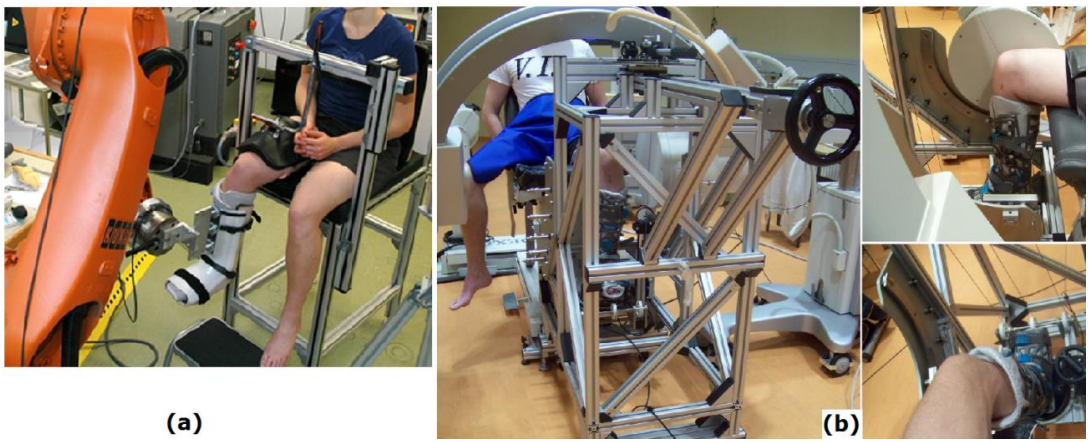

Figure 5.2 – *In vivo* measurements of knee laxity. (a) Robot-aided measurement in anterior translation and internal rotation as obtained from Lorenz et al., (2015). (b) Knee Rotometer used to assess the rotational laxity given an applied moment of 2.5 Nm. Obtained from Moewis et al., (2016).

5.2. Material and methods

5.2.1. Specimen preparation

Two fresh-frozen human right knee specimens, from a commercial source (Science Care, Phoenix, Ariz.) and stored in a walk-in freezer at -20°C, obtained by two males donors (SP1: age 60 years, mass 91 Kg, Stature 1.83 m; SP2: age 88 years, mass 91 Kg, Stature: 1.78 m) were used in this study. The effects of age on ligament mechanics have been studied, seeming to show that older donors' ACL-bones complexes have lower stiffness and smaller force at failures than younger donors (Noyes and Grood, 1976). However, difficulties exist in distinguishing age from other effects such as activity levels or diseases progression (Woo et al., 1986). Before testing, ethical approval was granted from the Deputy Chair of the Social and Behavioural Research Ethics Committee (SBREC) at Flinders University (SA - project no. 6832). Analysis of MRI scans (Dyck et al., 2012) confirmed the integrity of ligaments, cartilage and menisci. After 24 hours thawing at room temperature, the tibia, fibula and femur of each specimen were cut at mid shaft and all the soft tissue were dissected, except for those 15 cm above and 15 cm below the joint centre line.

5.2.2. Robotic system, alignment device, specimen fixation and control

The hexapod robot used for the tests was a Gough-Stewart platform-based manipulator with ultra-high stiffness and accuracy developed for biomechanical testing (Ding et al., 2015). This robot is capable of controlling in six DoFs either in position-control mode, force-control mode or hybrid-control mode. Specialised linear encoders allow a robot accuracy of 0.02 mm and 0.02° in position and angular rotation, respectively. A 6-DoFs load cell (SI-7200-1400, ATI Industrial Automation, Apex, NC) with a resolution of 3 N for forces and 0.2 Nm for moments was mounted between the top moving platform (end-effector) and the specimen (Figure 5.3).

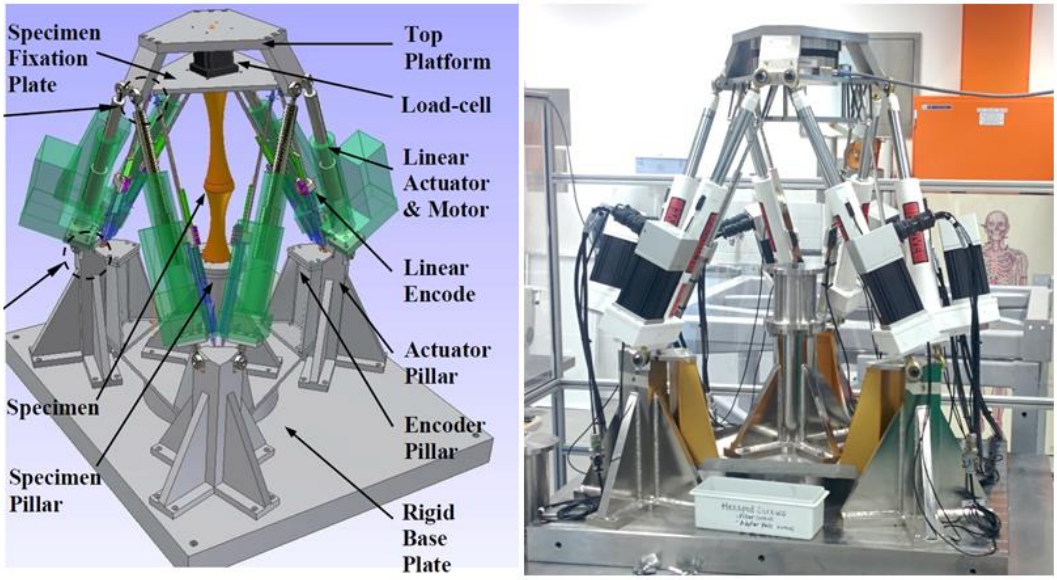

Figure 5.3 – Schematic representation (left) and physical realisation of the robot used in this study.

Before permanent fixation of the specimens to the robot, a knee alignment device was used to directly transfer a chosen experimental set up from the stainless steel lab surface into the robot where the space is limited. This alignment device enabled (1) the correct vertical distance from the fixation plate at the bottom to the end-effector of the robot to maximise the range of motion of the robot, (2) identification of the joint centre (midpoint between the medial and the lateral femoral epicondyles) and calculate the x-y- and z- axis offset for the control, (3) placing the tibia plateau

horizontal, keep the knee motion in the sagittal plane (where flexion/extension occur) as straight as possible and making the femoral transepicondylar axis (axis passing through the medial and the lateral femoral epicondyles) orthogonal to the sagittal plane. The alignment device included also a lower tooling mechanism used to set the desired angle of flexion to perform tests at different flexion-extension angles while keeping the end-effector horizontal. The tibia of each specimen was cemented in an aluminium cup using polymethylmethacrylate (PMMA) to be connected to the robot end-effector. The fibula was rigidly secured to the tibia with a cortical screw to preserve its anatomical position over testing. The femur was fixed to the lower tooling mechanism by fastening a transfix pin passing through a hole drilled in the bone as well as by the use of four cortical screws.

The described set up resulted in having the tibial axes always aligned to the end-effector axes, once the specimen was mounted into the robot. The end-effector was controlled in a local coordinate system during testing. Also, each specimen offset was set in the robot workstation to ensure controlling at the joint centre. These three factors, together with the assumption of coincident tibial and femoral coordinate system at full extension, ensured the positional and force outputs of the experiments were expressed in tibiofemoral joint anatomical coordinate systems (Grood and Suntay, 1983). This defines the anatomical rotations as flexion-extension (F-E), adduction-abduction (A-A), internal-external (I-E) and the anatomical translations as medial-lateral (M-L), anterior-posterior (A-P) and proximal-distal (P-D).

5.2.3. Experimental testing

The robotic system adopted in this study had never been used for knee testing before. The development of an ad-doc testing protocol for the knee joint, including the definition of the methodologies for specimen fixation, robot control as well as post-processing of the experiments, has hence been the first objective tackled in this part of the project.

The experiments included investigations at five F-E angles: 0°, 15°, 30°, 60° and 90° as in other studies (Gabriel et al., 2004; Kanamori et al., 2000; Mommersteeg et al., 1997; Robinson et al., 2006). The first three angles were achieved by manually

mounting the femur as its longitudinal axis formed an angle of 15° with the vertical line in the lower base tooling. For the last two angles, the femur was tilted at 75°. In both circumstances (Figure 5.4), once the specimen was rigidly connected to the system, the robot was driven under hybrid control to reach the first F-E angle to be tested (0° or 60°). This was achieved by slowly incrementing the F-E angle coordinate while minimising all the forces and moments. The same hybrid control was used to switch from one F-E angle to another during the experiments.

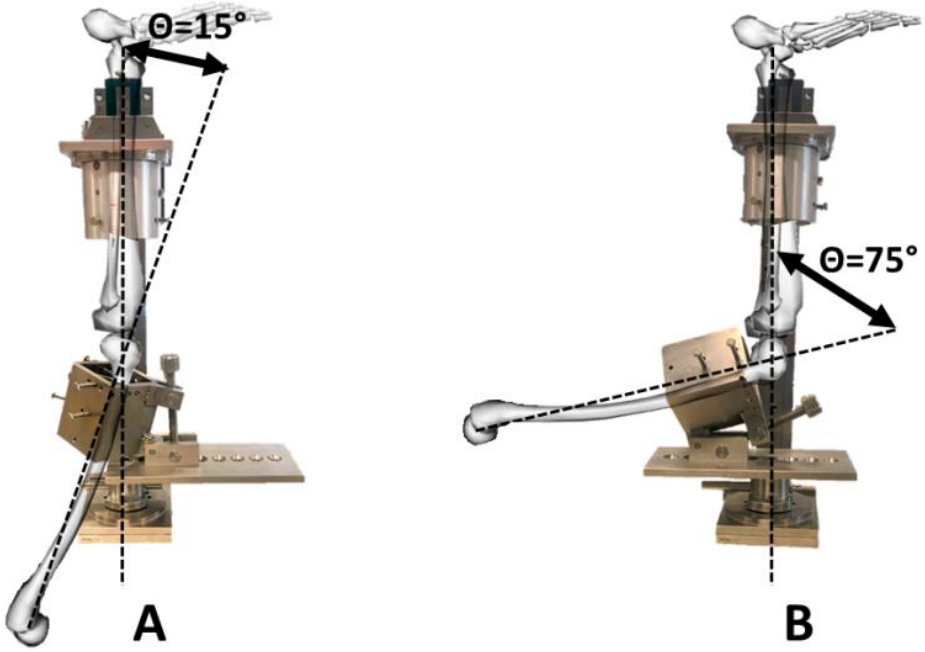

Figure 5.4 - Lower tooling configurations for the two testing configurations: knee flexed at 15° (A) and 75° (B).

A series of position control and force control tests were performed at each F-E angle. The position control tests included five single DoF controlled experiments in both positive and negative directions. Starting from each constrained F-E angle, a positive\negative incremental of linear\angular displacement was applied. The direction of the control was reversed when one of the following conditions occurred:

1. *Ultimate slope*: this condition was put in place 2 s after the start of each test and used to monitor the incremental slope of the controlled force-displacement curve in the previous second of testing. When the observed slope differed from linear more than 20%, the condition was met. The speed of testing was 0.33 mm/s (or 0.33°/sec) for all the tests except for the P-D translations, which were run at a reduced speed of 0.10 mm/s.

2. *Ultimate pose*: this condition was triggered when a controlled linear/angular displacement reached the absolute limits. These limits were set as ± 10 mm, ± 5 mm, 10° for M-L and A-P, P-D, and A-A and I-E, respectively.
3. *Ultimate load*: this condition was met when the measured load in the controlled linear/angular displacement reached the limit of 200 N and 20 Nm for forces and moments, respectively. These limits were reduced after the sequential ligament cuts (first cut: 180 N/18 Nm, second cut: 144 N/14 Nm, third cut: 115 N / 11 Nm).

The force control tests were implemented at each investigated F-E angle by simulating the combination of loads coming from two clinical tests that are normally carried out *in vivo* in orthopaedics: the Lachman (Fujie et al., 1996) and Pivot-Shift tests (Kanamori et al., 2000). The Lachman test was executed by applying an incremental force of ± 100 N in the A-P direction, whereas the Pivot-Shift test was performed by combining two moments both of ± 10 Nm and ± 10 Nm about the A-A and the I-E axes. Both tests were not executed after the third ligament cut to prevent soft tissue damage.

The described experimental protocol was applied for each intact specimen and then repeated three times after the sequential cut of three major knee ligaments. In the literature different cutting sequences have been explored (Robinson et al., 2006), each related to a specific output of the experiment (i.e. range of motion of the I-E rotation). Considering the wider scope of this study, it was decided to choose a sequence starting with the anterior cruciate ligament (ACL), which is the ligament with the highest incidence of partial/rupture among the knee injuries (Gage et al., 2012). Also, since the final testing would have been performed with only one major ligament on the specimen, it was decided to leave the medial collateral ligament (MCL) as the last intact ligament, which has strong deep and superficial bundles more resistant to rotations when compared to the posterior cruciate ligament (PCL) and the lateral collateral ligament (LCL). Thus, the following cutting sequence was adopted: ACL first, then PCL and lastly LCL. The ligament resection was performed by an experienced surgeon while keeping the specimen in the metal supports for a repeatable fixation on the robot over testing. A small straight longitudinal incision was performed through the skin and relevant soft tissues on the medial side of the

patella. The latter is brought to one side and the knee capsule was open in order to expose the cruciate ligaments. After each ligament cut, the incision was then quickly sutured back. The lateral collateral ligament was transected by another small skin incision on the lateral side.

At the end of testing, each specimen was dissected down completely and checked for integrity of the reaming structures by an orthopaedic surgeon, who helped during the experiments.

5.2.4. Post-processing of the experimental data

5.2.4.1. Pipeline for data pre-processing

Due to the impossibility to control for the experiments output in real time, the acquired raw data underwent a systematic process of verification and pre-processing in order to be used as a reliable input of to the next steps. This process is referred in the current thesis as the *pipeline for data pre-processing* and it is summarised in Figure 5.5. This part of the work has been developed in collaboration with two undergraduate students, Mr. David Agban (INSIGNEO summer placement program) and Miss Nurul Jannah Mohd Shaffie (SURE program).

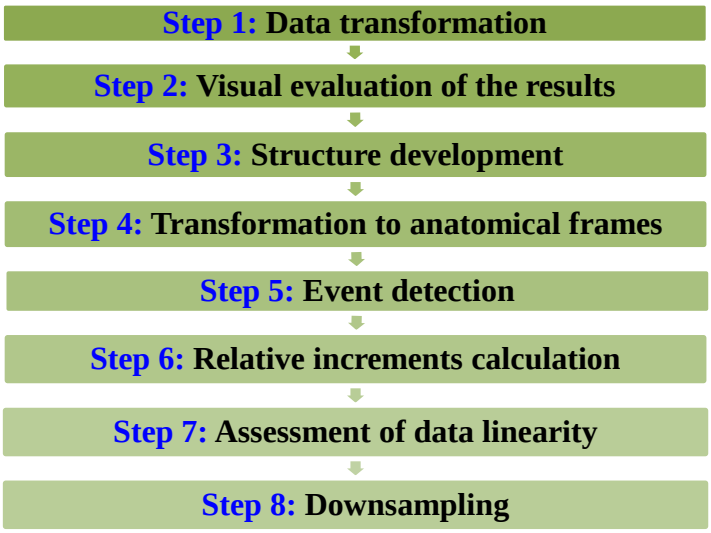

Figure 5.5 – Pipeline for data pre-processing.

Step 1 of the pipeline allowed transformation of robot raw data into Cartesian coordinate data. This step has been performed using a LabVIEW (National Instruments, Austin, TX) code which takes as an input the joint centre offset with respect to the moving platform, the six leg lengths of the hexapod robot as measured during the experiments and the forces and moment recorded by the load cell in a local coordinate system. Outputs of the calculation are the linear and angular displacements as well as forces and moments at the joint centre in a local coordinate system rigid with the moving platform.

Step 2 dealt with the plotting and visual evaluation of the outcome of each experiment. The position control tests were executed in a single DoF control starting from a selected neutral position and imposing increments while recording forces and moments in six DoFs. As an effect, analysing the graphs, a ramp should be visible in the controlled linear (or angular) displacement for the specific test done. This process ideally should cause an increase to the corresponding force (or moment) on the output graph. An example of correct test is shown in Figure 5.6.

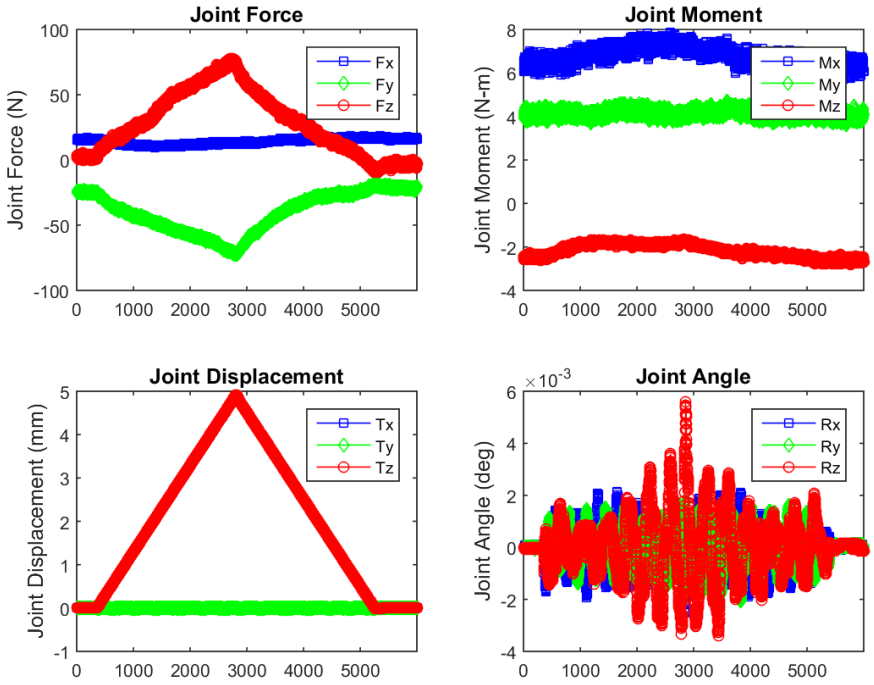

Figure 5.6 – Example of correct visual evaluation of a performed position control test.

The load control tests were performed by applying an increasing load while recording linear and angular displacements. A correct test execution should show an

increase for both the applied load and the corresponding axis/axes of the displacement (example in Figure 5.7).

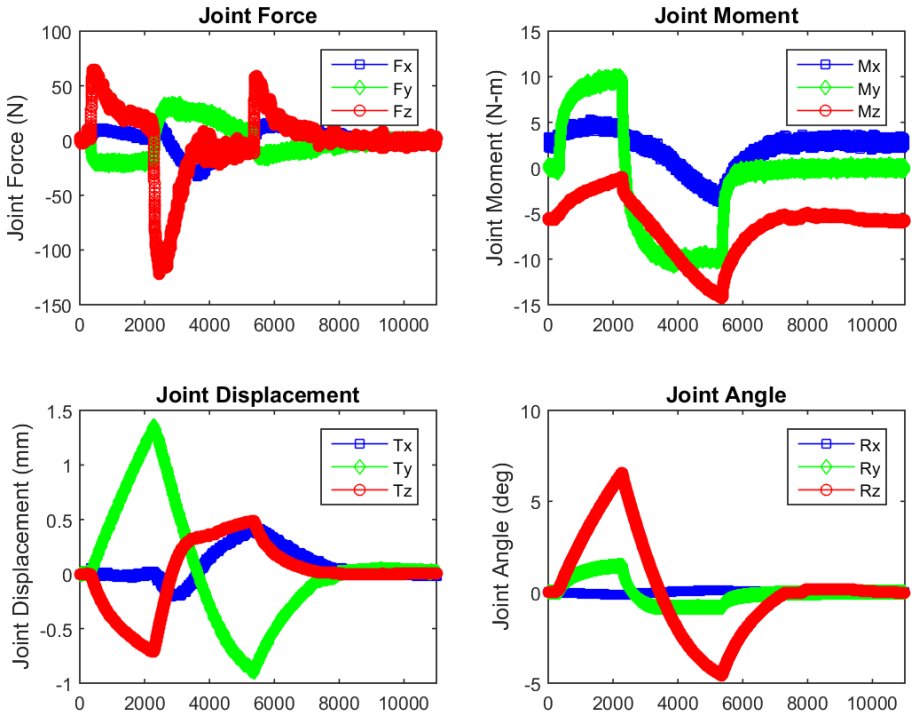

Figure 5.7 – Correct example of combined load control about Y and Z axes.

As summarised in Table 5.1, some of the experiments in specific directions did not produce satisfactory results due to experimental errors not detectable in real time. For example, a common wrong position control test shows a ramp in a different direction to one stated in the name of the test. These cases were therefore not included in the following steps. However, we ensured that at least one position control test (no matter if positive or negative) for each direction was included in the overall dataset of each specimen, flexion angle and condition.

INTACT					
	FLEXION ANGLE				
test ID	0 DEG	15 DEG	30 DEG	60 DEG	90 DEG
loadcontrol RzRy	Y	Y	Y	X	N
loadcontrol Ty	Y	N	Y	Y	Y
nRy	Y	Y	Y	Y	N
nRz	Y	Y	Y	Y	Y
nTx	Y	Y	Y	Y	Y
nTy	Y	Y	Y	Y	Y
nTz	Y	Y	Y	Y	Y
pRy	Y	Y	Y	N	Y
pRz	Y	Y	N	Y	Y
pTx	Y	Y	Y	Y	Y
pTy	Y	Y	Y	Y	Y
pTz	Y	Y	Y	Y	Y

X	*Missing data*
Y	*Correct result*
N	*Incorrect result*

Table 5.1 - Example of results evaluation in post processing for a specific specimen and configuration.

Step 3 was the development of an organised structure due to the considerable size of the whole dataset. The data was organised and stored in structural arrays (MATLAB ©), grouping specimens, joint conditions, configurations and types of performed tests (Figure 5.8). In this way, the loading of the organised data allowed for a precise and computationally efficient subsequent post-processing phase.

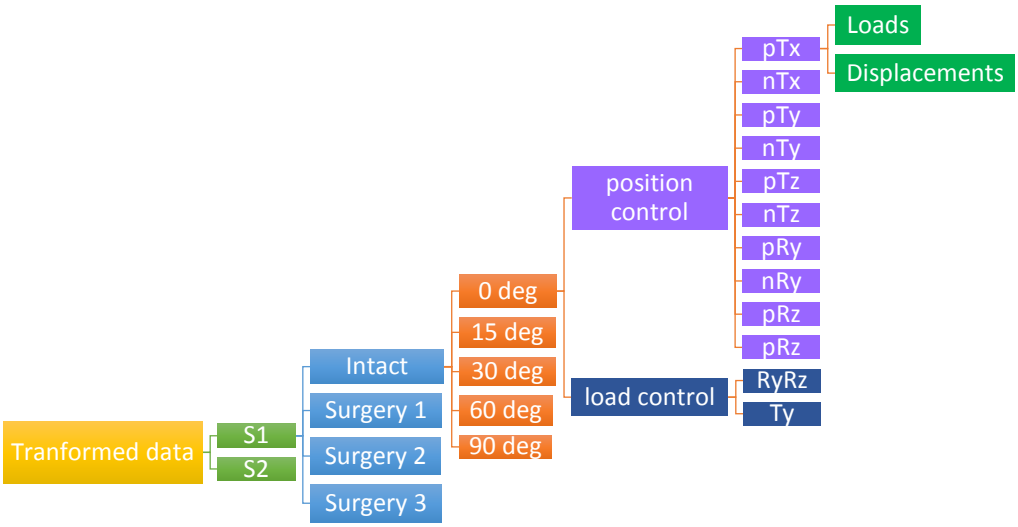

Figure 5.8 – Structure development of the experimental results. Surgery 1: ACL cut, surgery 2: ACL+PCL cut, Surgery 3: ACL+PCL+LCL cut.

Step 4 entailed the coordinate transformation from local Cartesian coordinate system of the robot to the knee anatomical axes. The transformation differed for each flexion extension angle configuration: experiments conducted at 0º, 15º and 30º of

flexion required a 180º rotation around the Y-axis, whereas for 60º and 90º a rotation of 180 º around the X-axis was performed.

Step 5 allowed detection of two main events in the recorded load and displacement curves. The two events are the beginning of ramp increment (threshold value) and the peak of the graph (peak index) in the controlled direction. The threshold value event was detected by measuring a difference higher than 0.02 mm between two adjacent frames along/about the controlled linear/angular displacement. The peak index event was identified as the frame corresponding to the absolute value of the maximum along/about the controlled linear/angular displacement. Once detected, only data from threshold value to peak index will be saved for the current pipeline, while the rest is not taken into account. Figure 5.9 shows an example of the cropped data of interest during event detection phase.

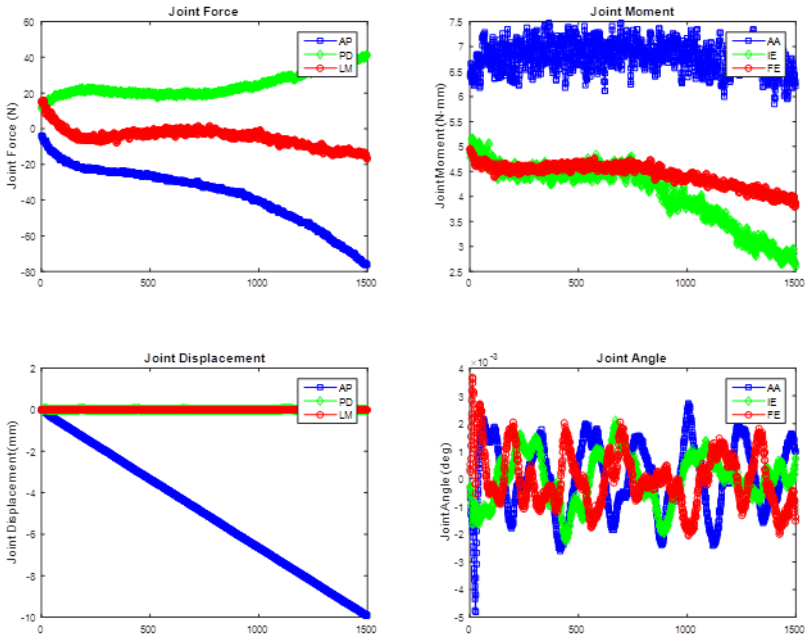

Figure 5.9 – An example of single DoF test in negative AP direction, after isolating the data of interest during event detection phase.

Step 6 aims to calculate the relative increments of displacements and loads for each dataset. To achieve this, the six DoF vector of displacement corresponding to the threshold value frame (described in step 5) was subtracted to all the frames of each experiment. The same was done for the loads to achieve the incremental loads.

Step 7 was about the assessment of the linearity of the different tests performed. The degree of linearity of the outcome was determined by the coefficient of determination (R^2), which was computed in the force-displacement diagram of the controlled direction. The closer the R^2 value to one, the better linearity of the result is achieved. In this experiment, the R^2 was ensured to have a value higher than 0.9 in the controlled direction of the position control tests. Figure 5.10 shows an example of this check for a test in the negative AP direction. Further analysis on the effects of data linearity on model validation will be shown in a subsequent analysis (see Figure 5.24).

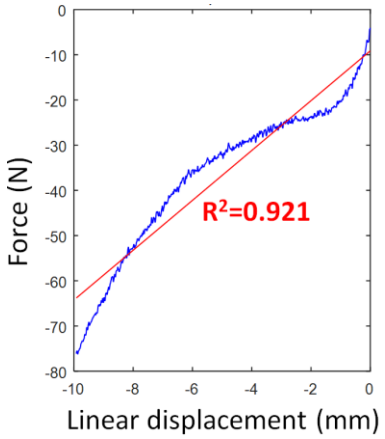

Figure 5.10 – Example of the assessment of data linearity performed.

Step 8 was introduced to reduce the number of samples in each input data series, deemed unnecessary due to the smoothness and regularity of the recorded signal. A cubic spine interpolation was hence applied to both displacements and loads. This method was selected for being characterised by smoother curves and smaller errors when compared to some other interpolating polynomials such as Lagrange polynomial and Newton polynomial. After some preliminary analysis, twenty-five samples for each single DoF test were deemed to be appropriate to capture the data trend under investigations (examples in Figure 5.11 and Figure 5.12). The data were processed from the beginning of the incremental test until when the maximum absolute value was reached in the controlled direction.

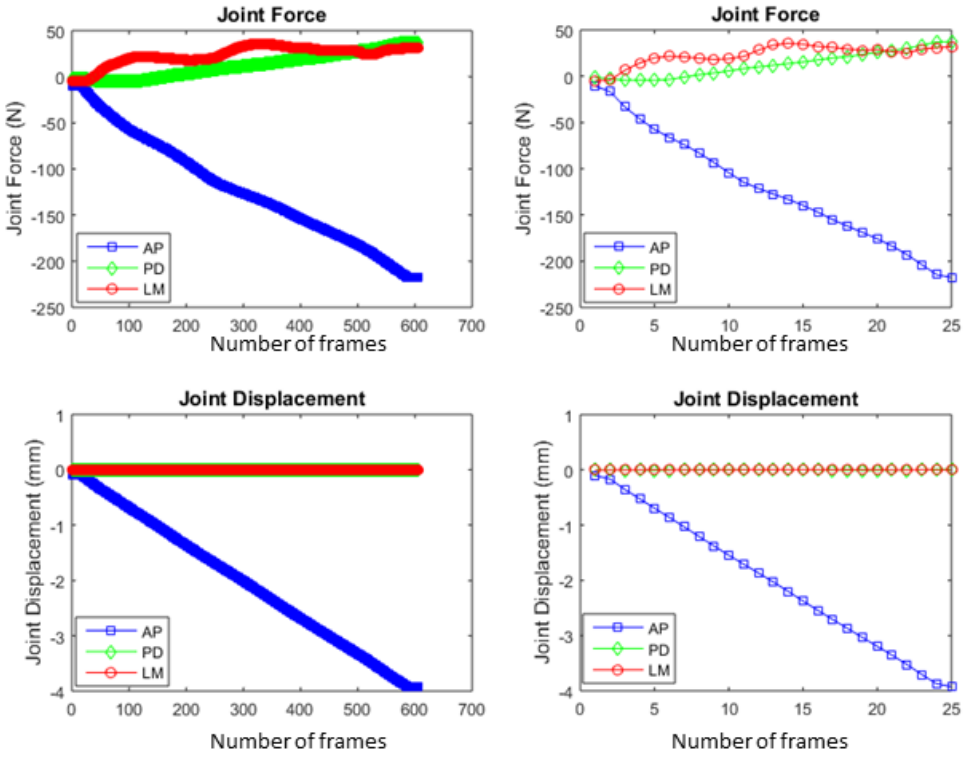

Figure 5.11 – Example of downsampling an AP test in the negative direction for forces and linear displacements. On left panels the original tests and on the right panels the tests with the reduced number of frames.

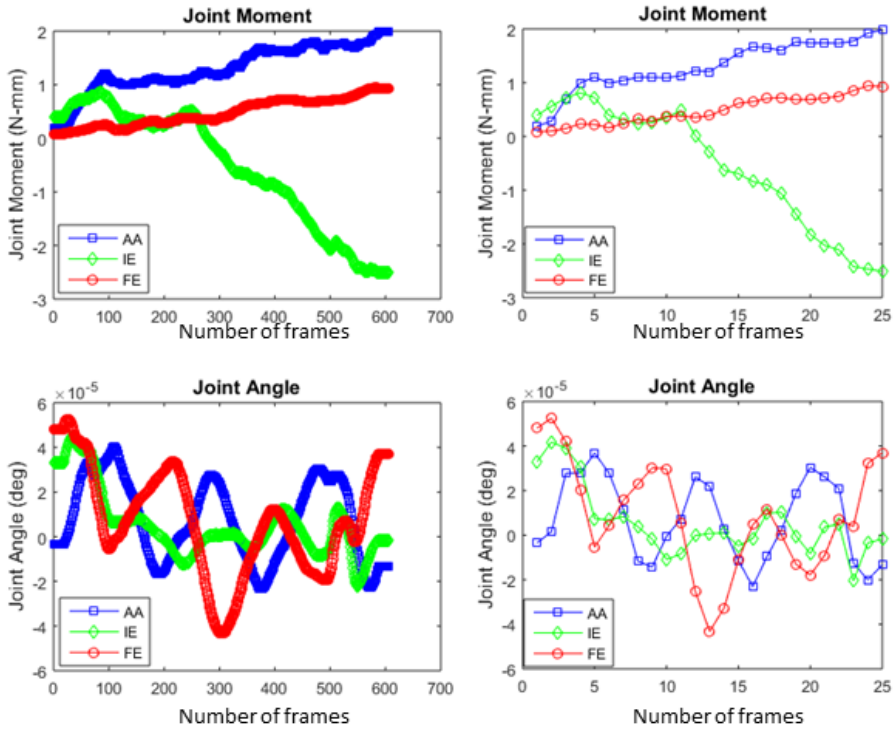

Figure 5.12 - Example of downsampling an AP test in the negative direction for moments and angular displacements. On left panels the original tests and on the right panels the tests with the reduced number of frames.

5.2.4.1.1. Compliance matrix calculation

The overall idea used to calculate the compliance matrices of the knee was based on the method described in Chapter 4.1, but the mathematical description of the problem and its implementation have been partially revised to overcome two main identified limitations identified in (Chapter 4 - Section 4.1.3): a) the limited amount of data of each single DoF test included in the matrix calibration; b) the fact that the non-homogeneity of the compliance matrix was not taken into account in the calculation process.

As previously explained, the compliance matrix $[C]$ relates the linear/angular displacements with the forces and moments. This matrix is symmetric when the load–displacement behaviour is assumed as linear in local configurations. In addition, the approach is designed for problems in which the joint linear and/or angular displacements can be considered small when compared to the overall dimension of the bones involved in the movement.

5.2.4.1.2. Generation of the compliance matrix from the measured data

At every observation, the force displacement relationship using $[C] = \{c_{ij}\}$

$$\begin{pmatrix} t_x \\ t_y \\ t_z \\ \theta_x \\ \theta_y \\ \theta_z \end{pmatrix} = \begin{bmatrix} c_{11} & c_{12} & c_{13} & c_{14} & c_{15} & c_{16} \\ & c_{22} & c_{23} & c_{24} & c_{25} & c_{26} \\ & & c_{33} & c_{34} & c_{35} & c_{36} \\ & & & c_{44} & c_{45} & c_{46} \\ & Symmetric & & & c_{55} & c_{56} \\ & & & & & c_{66} \end{bmatrix} \cdot \begin{pmatrix} F_x \\ F_y \\ F_z \\ M_x \\ M_y \\ M_z \end{pmatrix} \quad 5.1$$

can be expressed in a compact form as:

$$\begin{Bmatrix} t_{3X1} \\ \theta_{3X1} \end{Bmatrix} = \begin{vmatrix} T_{3X3} & C_{3X3} \\ C_{3X3}^T & R_{3X3} \end{vmatrix} \cdot \begin{Bmatrix} F_{3X1} \\ M_{3X1} \end{Bmatrix} \quad 5.2$$

Where:

T_{3X3}: Translational compliance submatrix (mm/N);

C_{3X3}: Coupling compliance submatrix (1/N);

R_{3X3}: Rotational compliance submatrix (1/Nmm).

In order to calculate the compliance matrix given the data coming from position control tests, an optimisation problem needs to be solved. Within this framework, a Cholesky decomposition of the compliance matrix was implemented to ensure its symmetry (for conservation energy principles) and positive definition (to be used as a stiffness matrix). The optimisation problem was numerically solved using the *fmincon* function in MATLAB (The Mathworks, USA).

Two matrices were built by concatenating by rows the above data, as recorded during the five positive and five negative position control tests described in section 5.2.3. :

$$[\Delta X] = [X - X_0] = [X_{ML}^+ \, X_{AP}^+ \, X_{PD}^+ \, X_{AA}^+ \, X_{IE}^+ \, X_{ML}^- \, X_{AP}^- \, X_{PD}^- \, X_{AA}^- \, X_{IE}^-] \quad 5.3$$

$$[\Delta F] = [F - F_0] = [F_{ML}^+ \, F_{AP}^+ \, F_{PD}^+ \, F_{AA}^+ \, F_{IE}^+ \, F_{ML}^- \, F_{AP}^- \, F_{PD}^- \, F_{AA}^- \, F_{IE}^-] \quad 5.4$$

where X_0 and F_0 represent the generalised displacement and force vectors, respectively, at the beginning of each position control test. $X_i^{+/-}\ for\ i = ML, AP, PD, AA\ and\ IE$, is built concatenating the three linear and angular displacements in the joint coordinate system, respectively. $F_i^{+/-}$ is built by concatenating the three forces and the three moments.

5.2.4.1.3. Choice of the objective function

The objective function was initially chosen as:

$$\mathrm{J(C)}_1 = \|[LL^T] \cdot [\Delta F] - [\Delta X]\|_2 \qquad 5.5$$

subject to the constraint of L being a real lower triangular matrix with strictly positive diagonal terms, which ensured each compliance matrix,$[C] = [LL^T]$, to be symmetric and positive defined.

Considering a random imposed compliance matrix $\mathrm{C}_{imposed}$ (6x6, symmetric and positive defined) and an input loads matrix generated using a randomly chosen experimental testing dataset $\mathrm{F}_{\mathrm{exp}\_testing}$ (6xN, N: data size of 250 samples), the corresponding matrix of linear/angular displacements can be calculated as: $\mathrm{X}_{true} = \mathrm{C}_{imposed} \cdot \mathrm{F}_{\mathrm{exp}\_testing}$. Using X_{true} and $\mathrm{F}_{\mathrm{exp}\_testing}$ as an input, a new compliance matrix can be estimated through optimisation ($\mathrm{C}_{\mathrm{estimated}}$).

An example of the results obtained using $\mathrm{J(C)}_1$ is given by the following matrices, calculated for one randomly chosen dataset:

$$C_{estimated} = \begin{matrix} 13.92 & 1.77 & 2.81 & 1.71 & 1.23 & 1.44 \\ 1.77 & 6.28 & 0.46 & 1.31 & 0.84 & 0.99 \\ 2.81 & 0.46 & 1.70 & 1.59 & 0.78 & 1.20 \\ 1.71 & 1.31 & 1.59 & 6.34 & 1.53 & 0.41 \\ 1.23 & 0.84 & 0.78 & 1.53 & 1.39 & 1.08 \\ 1.44 & 0.99 & 1.20 & 0.41 & 1.08 & 1.59 \end{matrix}$$

$$C_{imposed} = \begin{matrix} 13.91 & 1.77 & 2.81 & 1.71 & 1.23 & 1.44 \\ 1.77 & 6.28 & 0.46 & 1.31 & 0.84 & 0.99 \\ 2.81 & 0.46 & 1.70 & 1.59 & 0.78 & 1.20 \\ 1.71 & 1.31 & 1.59 & 71.60 & 1.51 & 0.54 \\ 1.23 & 0.84 & 0.78 & 1.51 & 2.70 & 0.84 \\ 1.44 & 0.99 & 1.20 & 0.54 & 0.84 & 2.07 \end{matrix}$$

The red boxes highlight differences in the values that can be attributed merely to non-homogeneity of the units of measurements of the relevant quantities. This can be better observed by looking at the expanded version of eq. 5.5:

$$J(C)_1 = \left\| \begin{bmatrix} c_{11} & c_{12} & c_{13} & c_{14} & c_{15} & c_{16} \\ & c_{22} & c_{23} & c_{24} & c_{25} & c_{26} \\ & & c_{33} & c_{34} & c_{35} & c_{36} \\ & & & c_{44} & c_{45} & c_{46} \\ & Symmetric & & & c_{55} & c_{56} \\ & & & & & c_{66} \end{bmatrix} \cdot \begin{pmatrix} F_{1x} & F_{2x} & \cdots & F_{nx} \\ F_{1y} & F_{2y} & \cdots & F_{ny} \\ F_{1z} & F_{2z} & \cdots & F_{nz} \\ M_{1x} & M_{2x} & \cdots & M_{nx} \\ M_{1y} & M_{2y} & \cdots & M_{ny} \\ M_{1z} & M_{2z} & \cdots & M_{nz} \end{pmatrix} - \begin{pmatrix} t_{1x} & t_{2x} & \cdots & t_{nx} \\ t_{1y} & t_{2y} & \cdots & t_{ny} \\ t_{1z} & t_{2z} & \cdots & t_{nz} \\ \theta_{1x} & \theta_{2x} & \cdots & \theta_{nx} \\ \theta_{1y} & \theta_{2y} & \cdots & \theta_{ny} \\ \theta_{1z} & \theta_{2z} & \cdots & \theta_{nz} \end{pmatrix} \right\| \quad 5.6$$

where the index n represents the data size of input loads and displacements used to estimate the terms of the compliance matrix (C). The 1st, 2nd and 3rd rows include lengths expressed in mm, whereas the 4th, 5th and 6th rows include angles expressed in radians. The differences in the above highlighted values of C are due to the fact that when minimising the objective function $J(C)_1$, all the rows are assumed to have the same importance and units are not accounted for.

To overcome this problem, an alternative objective function $J(C)_2$ was hence tested, which was subjected to the same constrains used for $J(C)_1$ but included also a normalisation weighting factor *w*, expressed in mm:

$$J(C)_2 = \|[LL^T][\Delta F] - [\Delta X]\|_{mm} + w \cdot \|[LL^T][\Delta F] - [\Delta X]\|_{rad} \quad 5.7$$

5.2.4.1.4. Choice of the optimal weight factor

An initial data analysis was performed, aimed at finding the optimal weight ($w_{optimal}$) factor by mathematically balancing the two different norms in the Equation 5.7. This idea, proposed for a different application by Gopalakrishnan et al., (2014), is shown in Figure 5.13. The weight factor is making iteratively vary until equivalence between the norm in mm and the norm in rad multiplied by the weight factor is found. This ensures to equally account for the different units of measurements in the optimisation function.

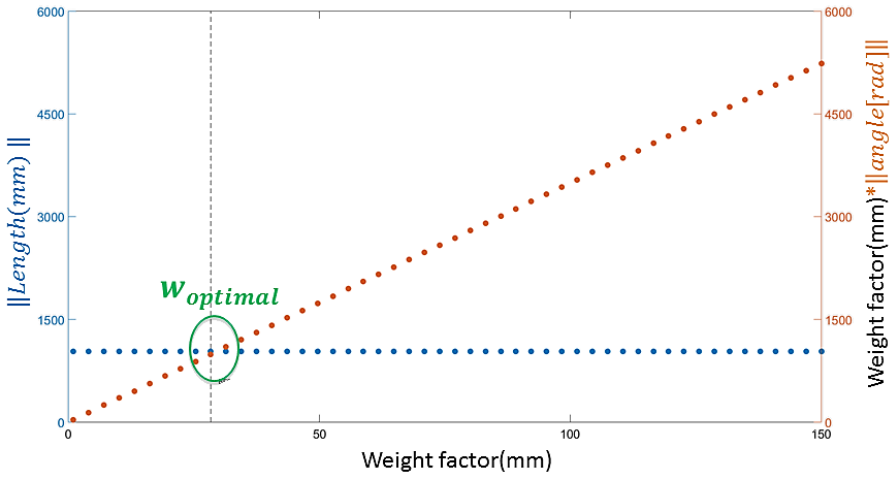

Figure 5.13 – Example of optimal weight factor determination for $J(C)_2$.

When the compliance matrix is estimated using $J(C)_2$ and $w_{optimal}$, the results obtained for the same data used in the example in section 5.2.4.1.3 were:

$$C_{estimated} = \begin{matrix} 13.915 & 1.765 & 2.813 & 1.714 & 1.234 & 1.436 \\ 1.765 & 6.284 & 0.458 & 1.308 & 0.838 & 0.994 \\ 2.813 & 0.458 & 1.698 & 1.590 & 0.776 & 1.196 \\ 1.714 & 1.308 & 1.590 & 6.342 & 1.530 & 0.413 \\ 1.234 & 0.838 & 0.776 & 1.530 & 1.390 & 1.083 \\ 1.436 & 0.994 & 1.196 & 0.413 & 1.083 & 1.590 \end{matrix}$$

$$C_{imposed} = \begin{matrix} 13.915 & 1.765 & 2.813 & 1.714 & 1.234 & 1.436 \\ 1.765 & 6.284 & 0.458 & 1.308 & 0.838 & 0.994 \\ 2.813 & 0.458 & 1.698 & 1.590 & 0.776 & 1.196 \\ 1.714 & 1.308 & 1.590 & 6.347 & 1.529 & 0.413 \\ 1.234 & 0.838 & 0.776 & 1.529 & 1.390 & 1.083 \\ 1.436 & 0.994 & 1.196 & 0.413 & 1.083 & 1.590 \end{matrix}$$

This example clearly shows how the different blocks are now better estimated.

A further analysis was then performed to generalise these results also to other matrices. The order of magnitude of the compliance matrix used as an initial guess for this analysis was chosen according to the results reported in Chapter 4.1. Fifty different $C_{imposed}$ compliance matrices were created by randomly varying the matrix elements, and fifty corresponding $C_{estimated}$ matrices were obtained using data from five of the twenty available datasets to build the $F_{exp\_testing}$.

The following index was used to quantify the error associated to the corresponding optimisations:

$$Delta\ Norm = \frac{Norm(C_{estimated} - C_{imposed})}{Norm(C_{imposed})} * 100 \qquad 5.8$$

The average of the $Delta\ Norm$ for the 50 matrices resulted to be equal to 147% for $J(C)_1$, whereas the same value decreased dramatically to only 8% for $J(C)_2$.

When using the above described optimal approach, however, a different weight factor needs to be calculated each time the input data changes. This means that, even for the same specimen tested, the optimal weight factor can vary (Figure 5.14), impacting on results comparison and interpretation.

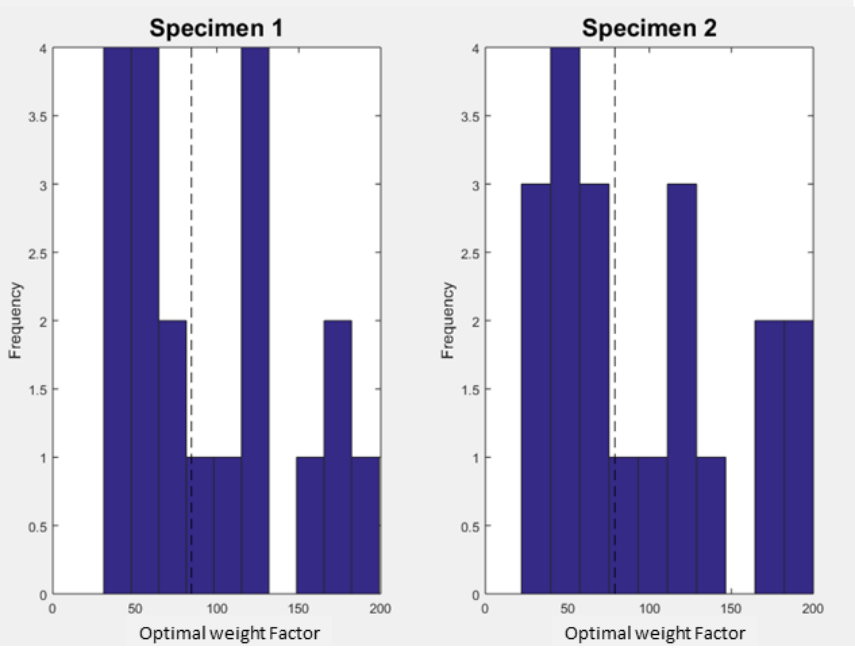

Figure 5.14 – This figure displays the distribution of the optimal weight factor separated for the two specimens tested. The vertical dashed lines represent the median value of the optimal weight factor for the two specimens.

For this reason, a second different criterion has been adopted for the choice of *w*, attempting to choose the same value for each specimen, based on an anatomical feature that: a) could be easily detected by manual palpation on *in vivo* subjects and b) is in the same range of magnitude of the median values of the optimal weight factors. $w_{anatomical}$ was hence chosen as the inter-epicondylar femoral distance. Its value for each specimen was determined from the segmented medical images (obtained using ITK-SNAP open source software - http://www.itksnap.org/, Figure 5.15). The loss of accuracy due to this choice is addressed in the following sections.

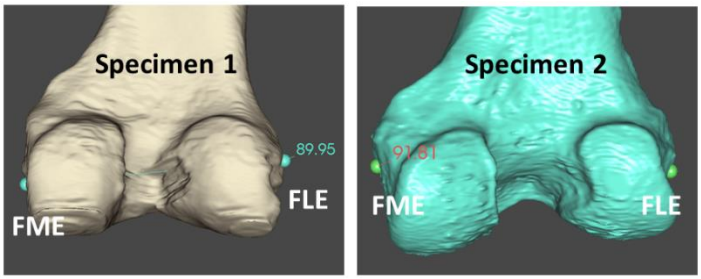

Figure 5.15 – Inter-epicondylar distance of the femur for the two specimens. Distances are expressed in mm. FME and FLE are medial and lateral epicondyles, respectively.

Running $J(C)_2$ with w optimal, 20 compliance matrices per specimen have hence been calculated using data from five flexion angles (0°, 15°, 30°, 60° and 90°) and

four specimen conditions (intact specimen, ACL cut, ACL+PCL cut, ACL+PCL+MCL cut).

5.2.5. Cross-validation

Since the aim of this chapter is to use the force control tests to understand if it is possible to personalise the compliance matrices calculated from the position control tests, the latter cannot be used for the validation. A validation approach different from the one presented in Chapter 4 was hence implemented based on the leave-k-out cross-validation (with k=5: four data subgroups were used for model training and the fifth for validation) to evaluate the accuracy of each compliance matrix in the prediction of the linear/angular displacements. Each compliance matrix calculated from the training subgroup was multiplied to each column of the measured force and moments from the validation group. This provided the predicted linear/angular displacements, to be compared with the measured linear/angular displacements.

Translation and rotation errors were quantified for each matrix in all the above phases, using the root mean square difference between predicted and measured displacements, normalised by the range of the measured data in each axial coordinate (NRMSE). Mean and standard deviation of the NRMSE were calculated for each specimen. The agreement between measured and predicted values was also assessed using the slope (a1), intercept (a0), and regression coefficient (r) obtained from a linear regression analysis.

The cross-validation results are shown in the figures below. An average NRMSE (Figure 5.16) lower than 10% was found for both specimens and for both translations (SP1: 9.6%; SP2: 8.4%) and rotations (SP1: 6.1%; SP2: 6.7%). The linear regression analysis (Figure 5.17) showed a strong correlation for both translations and rotations. Overall, rotations were better predicted than translations, with a higher regression coefficient (0.84 vs 0.62) and slope (0.77 vs 0.66), and a lower intercept value (-0.0001 vs -0.0184).

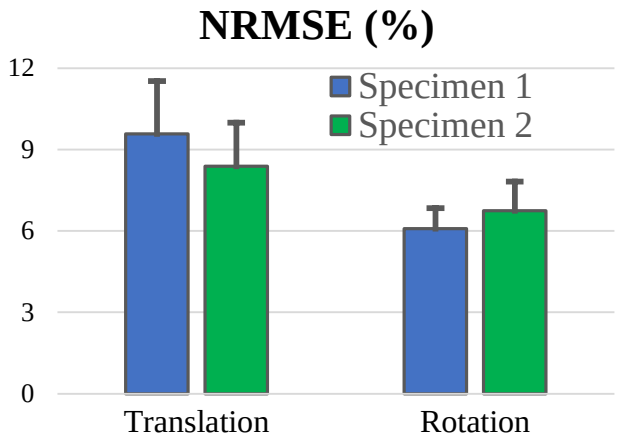

Figure 5.16 – Results of the normalised error per specimen related to the cross-validation performed.

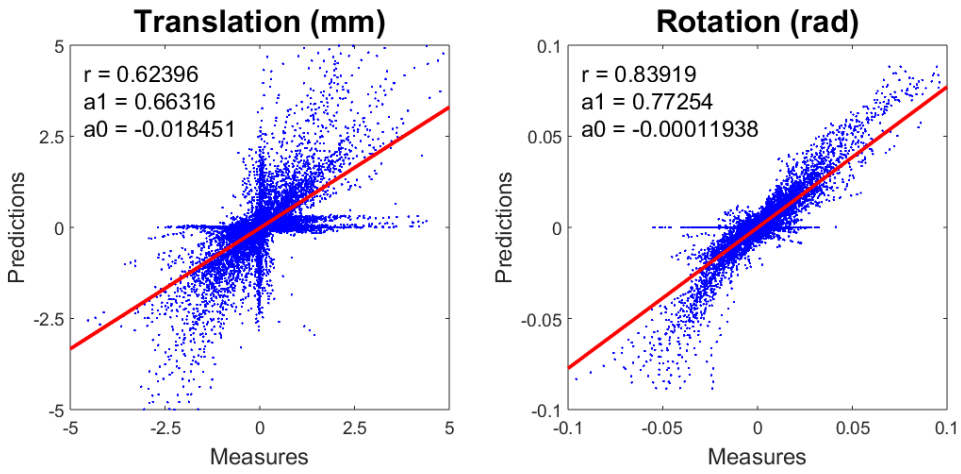

Figure 5.17 – Linear regression analysis results, reporting slope (a1), intercept (a0), and regression coefficient (r).

It is worth noticing that Figure 5.17 shows the cross-validation results of the whole dataset, whereas it would be interesting to analyse some specific configurations to understand the error distribution. For example, Figure 5.18 and Figure 5.19 show two specific cases, where the correlation was found very strong and very weak, respectively. One possible explanation making the correlation worse for the translation could lie in the range of input data. In fact, the dataset in Figure 5.19 is characterized by displacements higher than 6 mm, whereas Figure 5.18 contains data reaching up to 2 mm.

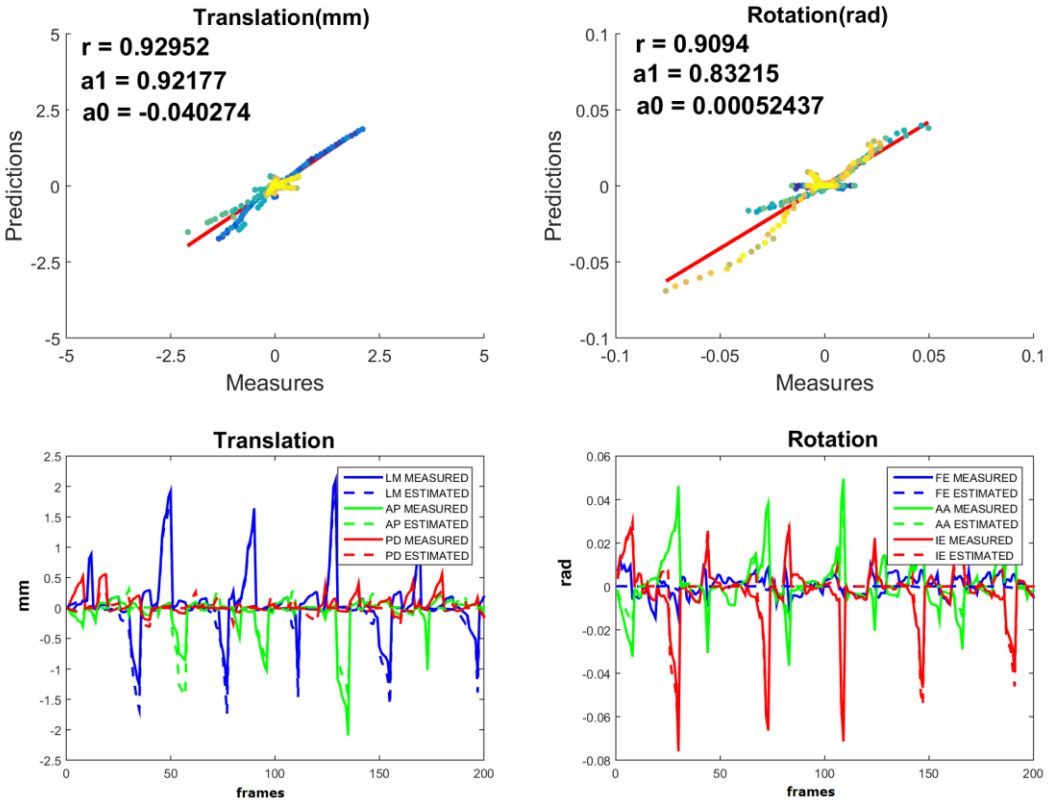

Figure 5.18 – Cross-validation (top panels) on a single compliance matrix case: S1, intact conditions, 30° of flexion. The bottom panes show the performance of the validation subset, where continue line represents the three components of the measured values and dashed line is the corresponding estimated value.

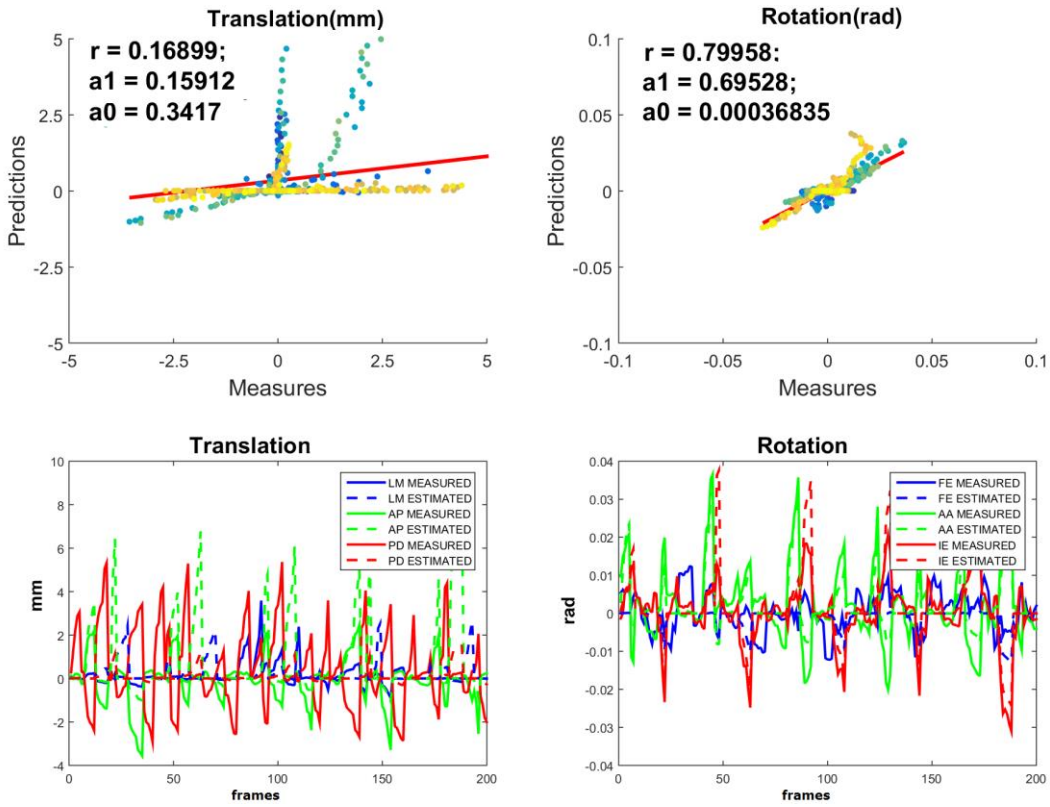

Figure 5.19 - Cross-validation (top panels) on a single compliance matrix case: S1, ACL&PCL cut, 90° of flexion. The bottom panes show the performance of the validation subset, where continue line represents the three components of the measured values and dashed line is the corresponding estimated value.

The effects of possible non-linearities from each position control test were also accounted for in this validation phase. As shown in Chapter 2 (Figure 2.3), every ligament exhibits non-linear regions (region 1, region 3 and region 4) during a tensile test experiment. Although the experiments presented in this chapter are conducted on the knee specimen as a whole and not on single ligaments, these non-linearities might influence the calculated compliance matrices and the related validation results. For this reason, all the multiple cross-validations were performed by attempting to exclude the regions where the non-linearities were expected (i.e. beginning and the end of each position control test). Figure 5.20 shows how different ranges of percentages of 5-95%, 10-90%, 15-85%, 20-80%, 25-75% and 30-70% for the position control tests were considered.

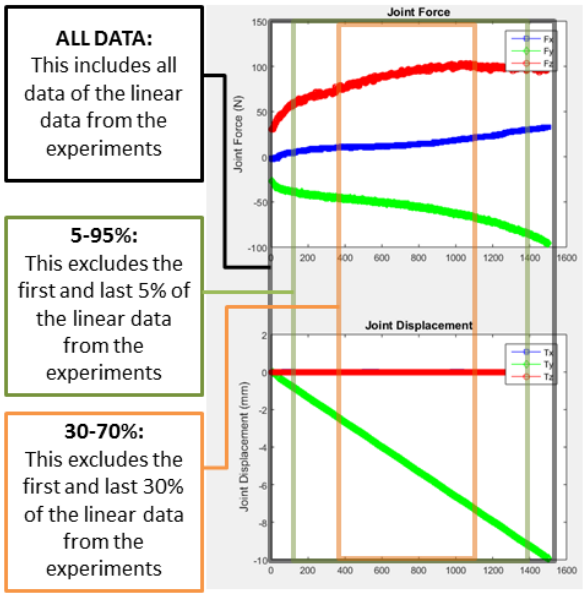

Figure 5.20 – Example to clarify how the different percentages were selected based on position control tests applying a negative ramp along the Y direction.

The results obtained by performing for each case a new cross-correlation analysis can be observed in Figure 5.21 and Figure 5.22. Similar average values of NRMSE were found in the different cases. The same stands for the regression analysis, where the regression coefficients range from to 0.60 to 0.62 and from 0.81 to 0.82 for translations and rotations, respectively.

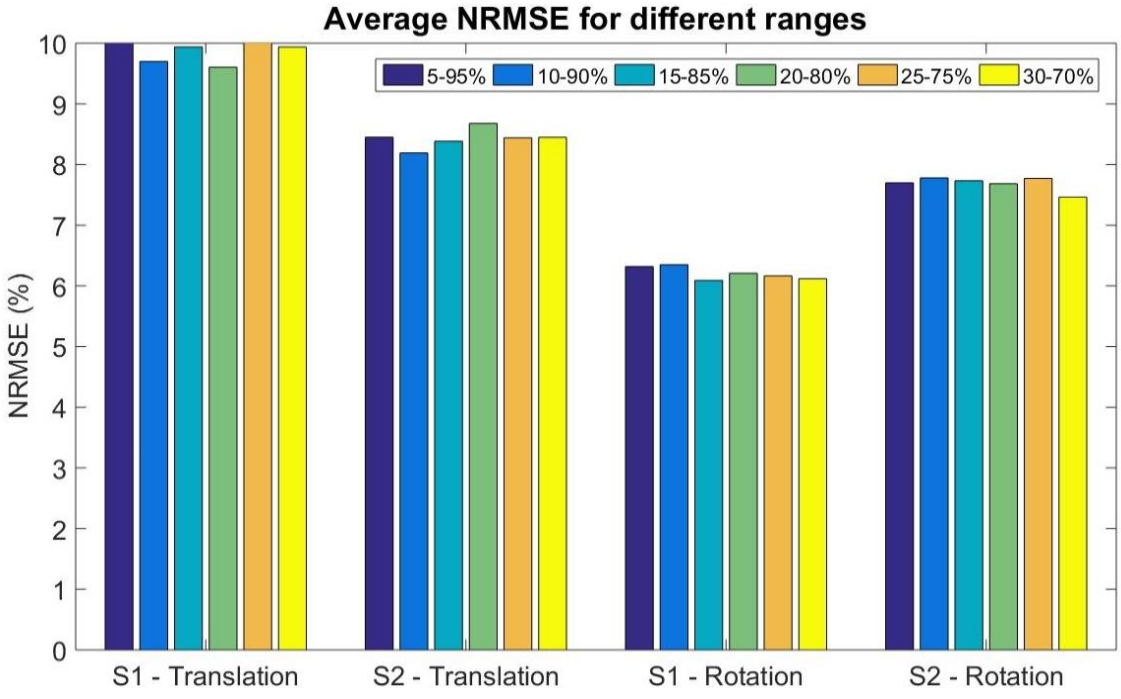

Figure 5.21 – Different values of NRMSE, averaged per specimen and coordinate.

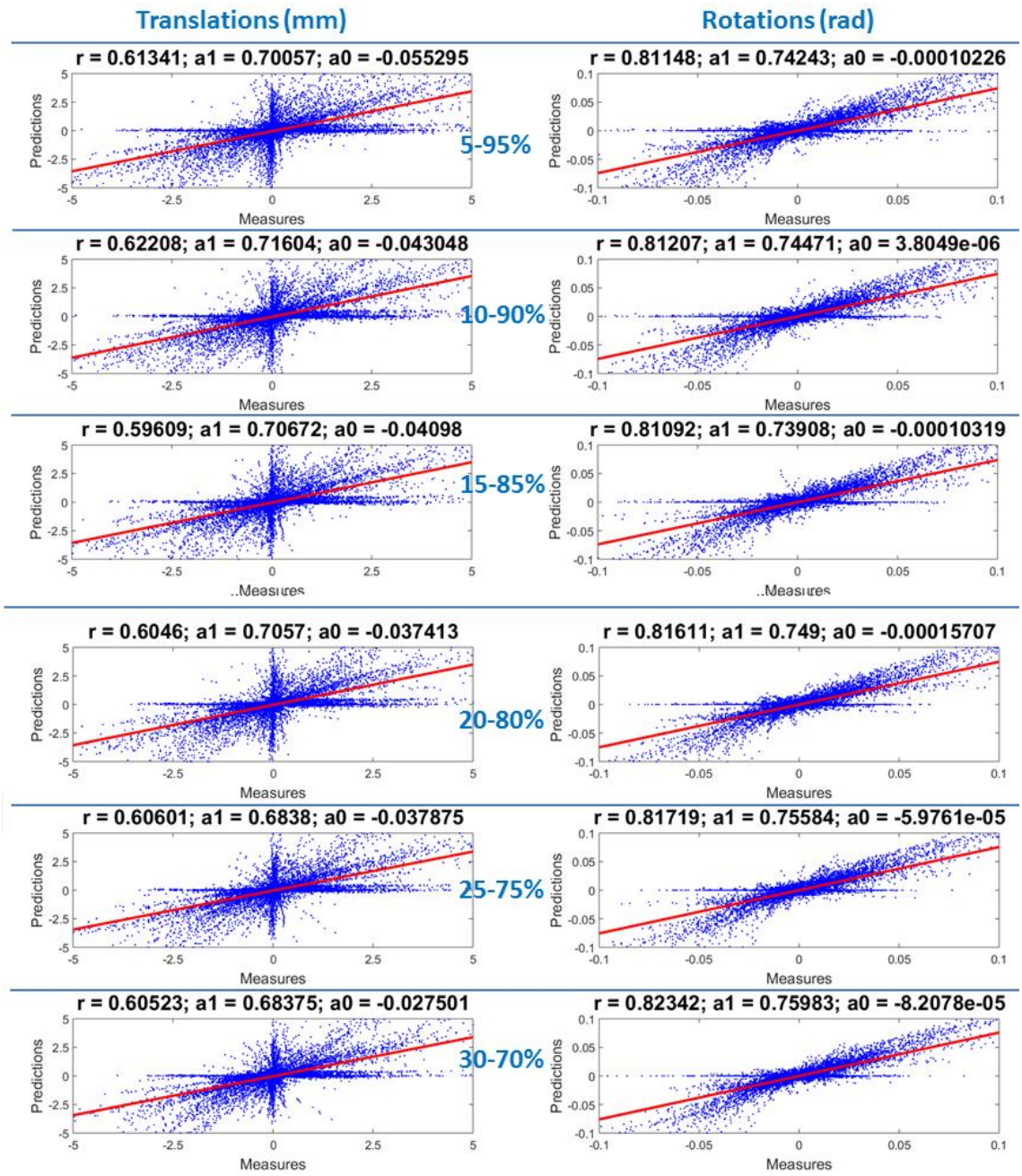

Figure 5.22 – Linear regression analysis performed by excluding different ranges of each of the position control test.

As discussed previously, to quantify the loss in accuracy due to the choice of $w_{anatomical}$ rather than $w_{optimal}$ when using $J(C)_2$, the leave-k-out cross-validation was performed also on the data obtained using $w_{optimal}$. The NRMSE (Figure 5.23 and Figure 5.24) for each of the compliance matrices were overall comparable with, as expected, values slightly better for the optimal weight factor optimisation, both for translations (average NRMSE 9.3% VS 9.6% in S1- 8.3% VS 8.4% in S2) and for rotations (average NRMSE both 6.1% in S1- 6.7 VS 6.8 in S2). According to

these findings, the choice of $w_{anatomical}$ was maintained in all the following analyses.

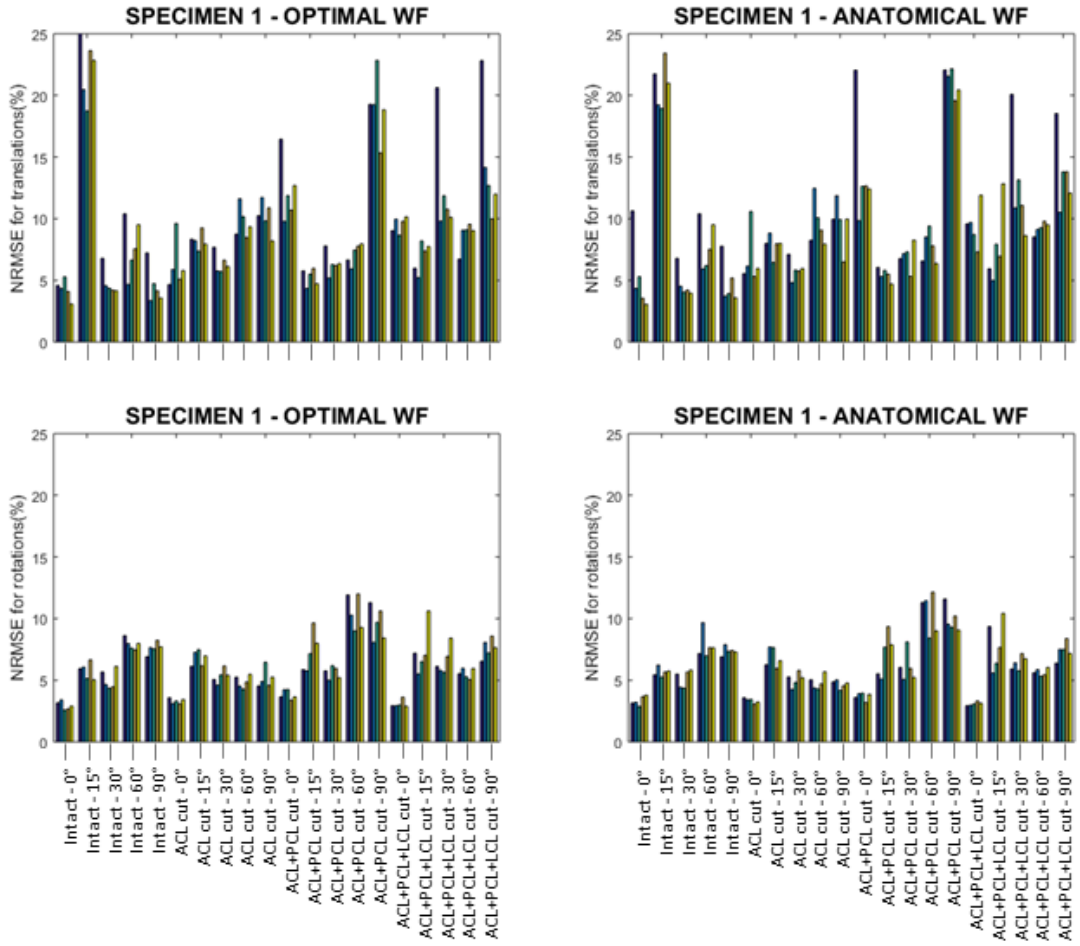

Figure 5.23 – Cross-validation results of specimen 1 for the two optimisation function used.

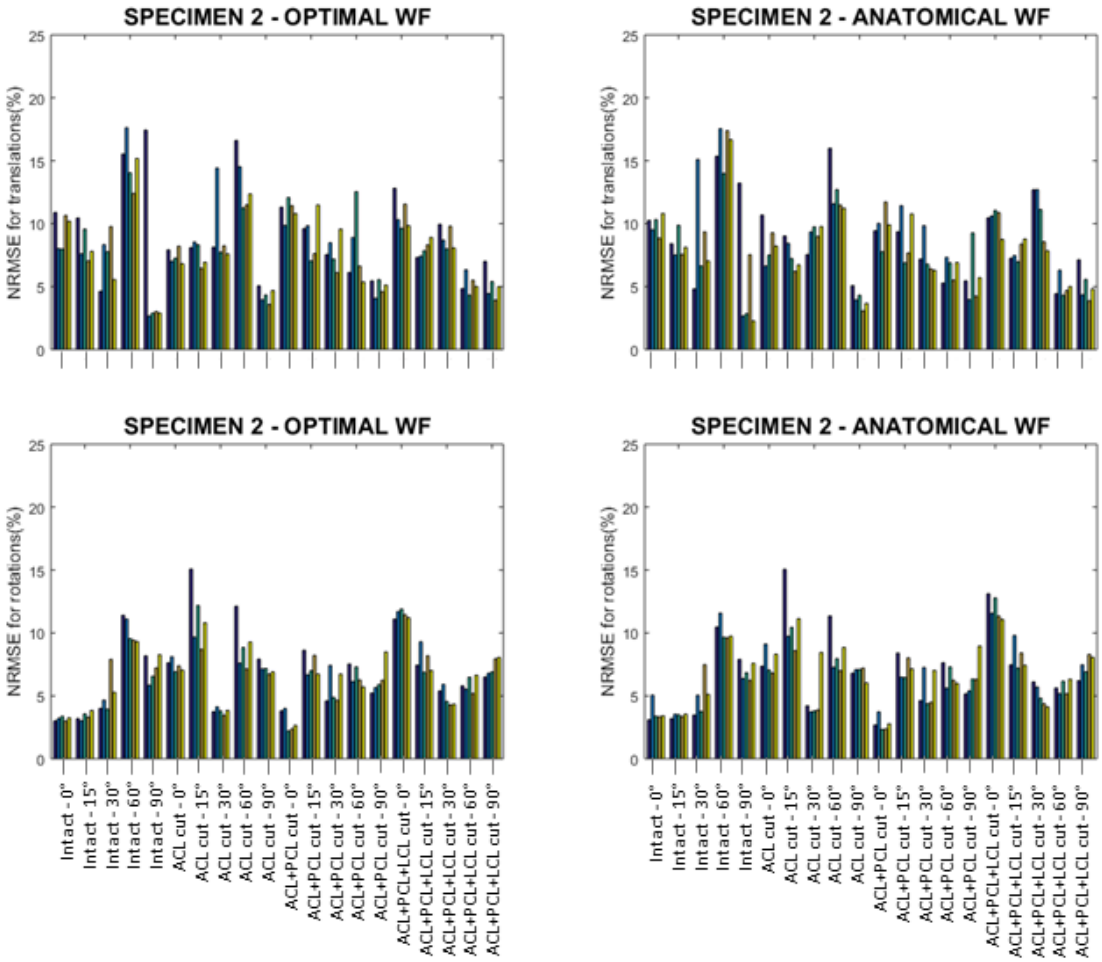

Figure 5.24 - Cross-validation results of specimen 2 for the two optimisation function used.

5.2.6. Model Personalisation

For the purpose of personalisation, only data from the force control tests were used. Conversely from the previous analyses, the experiments investigated here included the data coming from the simulation of the clinical tests (Lachman and pivot-shift tests), for which an additional set of compliance matrices was calculated ($C_{clinical\ tests}$). It is worth noticing for these new matrices that, whereas each dataset of position control tests covered all the DoFs of the knee, the clinical tests only provided information limited to specific directions. The matrices from the first scenario ($C_{6\ DoF}$) would hence be more representative of the overall knee mechanical properties when compared with $C_{clinical\ tests}$. This makes the comparison between the two scenarios difficult, with no a-priori knowledge about what terms,

components or features the attention should be focused on. The analysis described in the following section aims also to clarify this matter.

As a first assessment, the $C_{clinical\ tests}$ and the corresponding $C_{6\ DoF}$ matrices were compared term by term. In addition to this, a second level of comparison between $C_{clinical\ tests}$ and $C_{6\ DoF}$ was performed by decomposing each matrix and analysing the difference in specific components of the decomposition, allowing identification of matrix similarities that go beyond a simple term-by-term equivalence and to identify the elements most suitable to personalisation.

A method recently proposed by Chen et al., (2015) has been identified for the second comparison. This method, able to handle the non-homogeneity in terms of units of measurements of the compliance matrix (Angeles, 2010), is named Principal Axes Decomposition (Figure 5.23). It aims to maximally decouple the translational and rotational components of the compliance matrix, assuming small displacements and a symmetric and positive-defined matrix. This decomposition has some peculiar features such as uniqueness, coordinate-invariance, ability to handle rank-deficiency, and physical realisation. The latter, in particular, is very interesting for the scope of this study because it permits going from a compact mathematical form (matrix) to a physical mechanical equivalent system of rigid bodies connected by two orthogonal sets of torsional and screw springs (Figure 5.26).

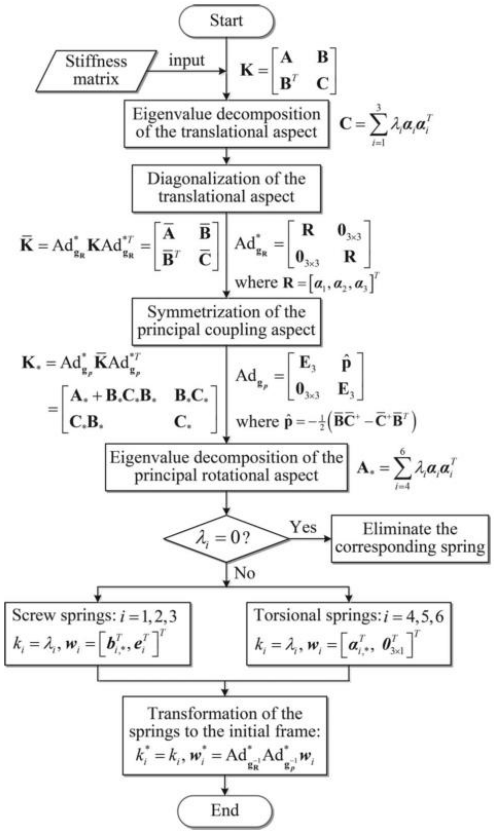

Figure 5.25 - Flowchart of the principal axes decomposition for a spatial stiffness matrix. Obtained from Chen et al., (2015). ©2015 IEEE.

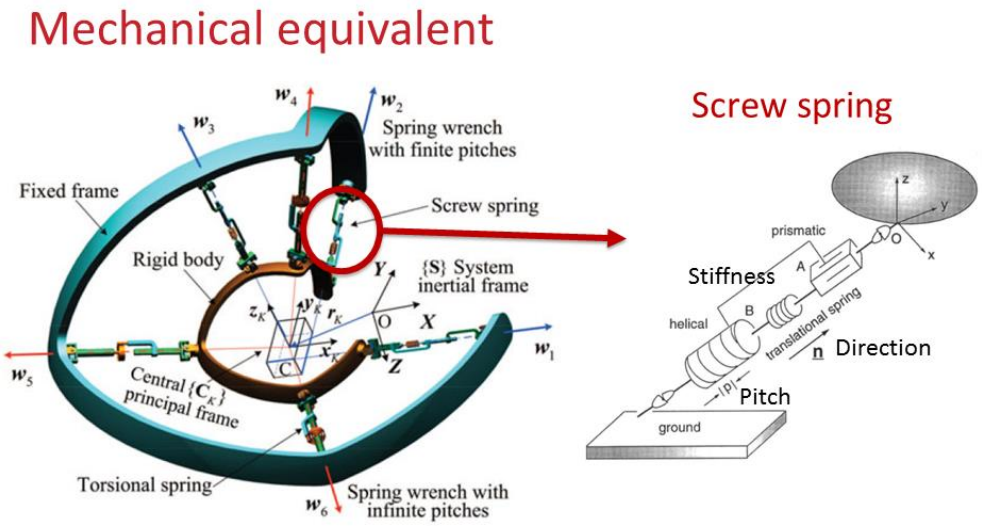

Figure 5.26 – On the left, schematic representation of the mechanical equivalent of any compliance (or stiffness) matrix coming from the principal axis decomposition. Adapted from Chen et al., (2015) ©2015 IEEE. On the right, more details about the screw spring mechanism composed by the combination of a prismatic and a helical joints, coupled by a linear spring. Adapted from Huang and Schimmels, (1998) with ASME permission.

Assuming the $C_{6\,DoF}$ as a reference value, a Bland-Altman analysis was used to compare $C_{clinical\ tests}$ and $C_{6\,DoF}$. The 50th percentile of the difference between the two matrices (bias) was calculated for the translational, rotational and coupling sub-blocks in the first comparison as well as the range 60th - 40th percentiles of differences. Limits of agreement were set to 2.5th and 97.5th percentiles, providing an interval within which 95% of differences between $C_{clinical\ tests}$ and $C_{6\,DoF}$ are expected to lie. For the second comparison, the Bland-Altman analysis was performed separately for the different elements of the decomposition: compliance coefficients and directions of the screw and of the torsional springs, and positions and pitches of the screw springs. Both for the first and second comparisons, the analysis was divided in to the cases in which data was available from both clinical tests, only from Lachman test, and only from Pivot-shift. This was done to investigate potential differences in terms of personalisation among the cases under analysis.

5.3. Results

The Bland-Altman analysis showed overall good agreement between the compliance matrices calculated with clinical tests and with position control data. For the term-by-term comparison (Figure 5.27), the data coming from the Lachman tests proved to be more reliable in terms of personalisation when compared with the Pivot-shift test. Indeed, the 60th - 40th range was lower for all the three sub-blocks of the compliance matrix (0.0037 mm/N VS 0.0176 mm/N for translations, 0.0014 1/N VS 0.0025 1/N for rotations, and 0.0001 N/mm VS 0.0002 N/mm for couplings). When looking at datasets containing both clinical tests (panels on the left of Figure 5.27), the results showed very few differences in the Bland-Altman plot outside the limits of agreements, with low bias values. The 60th - 40th ranges were between datasets of Lachman and Pivot-shift only for the translations (0.0047 mm/N), higher than the two datasets for rotations (0.0035 1/N), and equal to Lachman and lower than Pivot-shift for couplings (0.0001 N/mm).

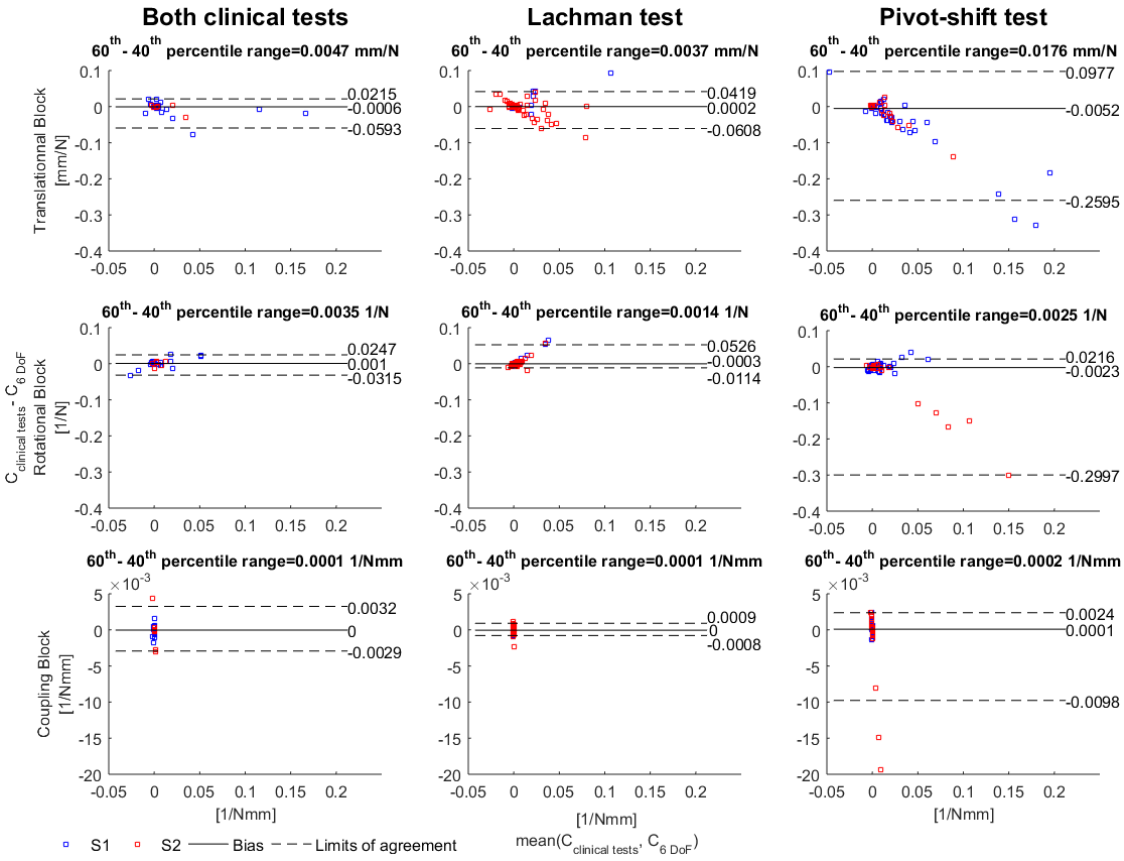

Figure 5.27 – Bland-Altman analysis for the first comparison.

A similar trend was found for the comparison based on the matrix decomposition (Figure 5.28), with Lachman test performing better than Pivot-shift in terms of personalisation. The Lachman 60^{th} - 40^{th} percentile range was always lower than the same range calculated for the Pivot-shift tests (up to 0.004 1/N VS 0.0218 1/N for the compliance coefficients of the torsional springs). Interestingly, the datasets containing both clinical tests (panels on the left of Figure 5.28) were characterised by an improved agreement of specific components of the matrix decomposition. For example, both tests 60^{th} - 40^{th} percentile ranges were lower with respect to the datasets containing only Lachman or Pivot-shift for compliance coefficients of screw springs, for positions of the screw spring sets, and for pitches of the screw springs.

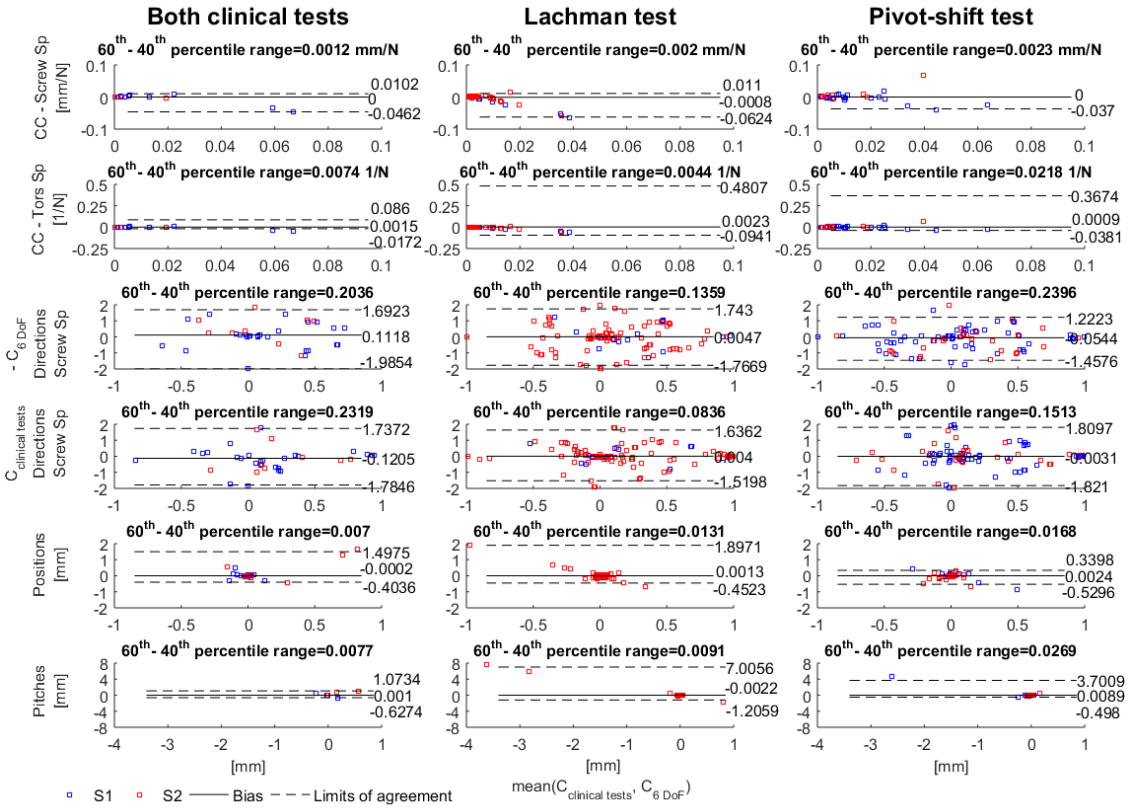

Figure 5.28 – Bland-Altman analysis for the second comparison. For the panel at the top right, an upper limit of agreement of 0.56 mm/N was found. CC: Compliance coefficients; Screw Sp: Screw spring; Tors Sp: Torsional spring.

5.4. Discussion

This chapter investigated the development, validation and personalisation of a force-based model of the knee joint that does not rely on detailed subject anatomy. The obtained results showed the feasibility of this approach on an *ex vivo* dataset. The application of the described procedure on a larger number of specimens, however, is required to robustly transfer this idea to an *in vivo* scenario.

The methodology developed to characterise a mechanical model of the knee joint originated from a previous study (described in Chapter 4.1), which has been extensively revised through multiple verification steps with the aim of increasing its reliability and robustness. A new *ex vivo* testing methodology has also been developed and verified. This testing protocol could be also adapted to perform different knee joint experiments on the hexapod robot, characterised by a limited space and range of motion. In addition, a step-by-step verified processing pipeline

has been established to efficiently go from the robot raw data to calculated compliance matrices describing the force-displacement behaviour of the joint.

The validation of the model, performed using the position control tests, showed low errors for both specimens in terms of translation and rotation (average NRMSEs below 10%). Better correlation was found for rotation (r=0.84) compared with translation (r=0.62) during a regression analysis. The lower value for the translation experiments was due to some values on the axes of the plot (left panel of Figure 5.17), indicating that for some cases, non-negligible measured translations are estimated as close to zero or vice versa. As a verification step, an evaluation of the effects of residual non-linearities on the cross-validation results was performed. This demonstrated that the behaviour of the model does not change when excluding some of the expected sources on non-linearities in the input data. As a consequence, the values on the axis making the correlation worse for translations are perhaps due to the implemented optimisation. Bearing in mind the low NRMSEs found, further studies can investigate alternative optimisation techniques to be implemented and tested.

Results concerning the personalisation of the compliance-matrices model using clinical tests were promising according to both implemented comparison approaches. For the term-by-term comparison of the different blocks of the compliance matrices, the dataset including only the Lachman test was the one that performed better (Blant-Altman analysis in Figure 5.27). When examining the results of the comparison based on the matrix decomposition (Figure 5.28), some elements of the decomposed matrices containing both clinical tests performed better than datasets containing only Lachman or Pivot-shift, respectively. This suggests that, if a generic knee model based on compliance matrices would be available, specific elements of the matrices could be personalised using the results of clinical tests and using a principal axes decomposition like the one here introduced.

The results presented in this study are of course affected by a number of limitations. First, real time monitoring of the results was not possible during experiment execution. This resulted in multiple tests either in position or in force control to be excluded from the pipeline for data pre-processing. Although having the full dataset

available would have probably strengthened the results of the analysis, the choice was to have less but more reliable input data to build the matrices. Second, only two specimens were tested at this stage. This is the minimum number to show a proof of concept as presented in the aim of this chapter. However, more specimens need to be tested to achieve more robust conclusions for the current procedure. Lastly, the robotic testing on cadaveric specimens represents an ideal scenario that will be the basis to face the more challenging and less-controllable collection of clinical tests data *in vivo*.

In conclusion, despite the highlighted limitations, the work described in this chapter clearly highlight the possibility to develop a force-based knee model not relying on detailed anatomy and personalised with clinical test data. It has also been shown that the matrix decomposition is a suitable method to discriminate, on the basis of available clinical test data, which of the model elements should be personalised to potentially improve its accuracy. In the future, a generic model of the knee built using more specimens might be used as a starting reference to build a population matrix that could then be made subject-specific by updating some of its elements using this decomposition approach. Ideally, the advances of stiffness measurement technologies *in vivo* will allow obtaining the *in vivo* clinical data needed to drive the *ex vivo* based matrix update.

References

Angeles, J., 2010. On the Nature of the Cartesian Stiffness Matrix. Ing. mecánica, Tecnol. y Desarro. 3, 163–170.

Chen, G., Wang, G., Lin, Z., Lai, X., 2015. The Principal Axes Decomposition of Spatial Stiffness Matrices. IEEE Trans. Robot. 31, 1561–1564. doi:10.1109/TRO.2015.2496825

Ding, B., Cazzolato, B.S., Stanley, R.M., Grainger, S., Costi, J.J., 2015. Stiffness Analysis and Control of a Stewart Platform-Based Manipulator With Decoupled Sensor – Actuator Locations for Ultrahigh Accuracy Positioning Under Large External Loads. J. Dyn. Syst. Meas. Control 136, 1–12. doi:10.1115/1.4027945

Dyck, P., Smet, E., Veryser, J., Lambrecht, V., Gielen, J.L., Vanhoenacker, F.M., Dossche, L., Parizel, P.M., 2012. Partial tear of the anterior cruciate ligament of the knee: injury patterns on MR imaging. Knee Surgery, Sport. Traumatol. Arthrosc. 20, 256–261. doi:10.1007/s00167-011-1617-7

Ewing, J.A., Kaufman, M.K., Hutter, E.E., Granger, J.F., Beal, M.D., Piazza, S.J., Siston, R.A., 2016. Estimating patient-specific soft-tissue properties in a TKA knee. J. Orthop. Res. 34, 435–443. doi:10.1002/jor.23032

Fregly, B.J., Besier, T.F., Lloyd, D.G., Delp, S.L., Banks, S. a, Pandy, M.G., D'Lima, D.D., 2012. Grand challenge competition to predict in vivo knee loads. J. Orthop. Res. 30, 503–13. doi:10.1002/jor.22023

Fujie, H., Livesay, G., Fujita, M., Woo, S., 1996. Forces and moments in six-DOF at the human knee joint: mathematical description for control. J. Biomech. 29, 1577–1585.

Gabriel, M.T., Wong, E.K., Woo, S.L.-Y., Yagi, M., Debski, R.E., 2004. Distribution of in situ forces in the anterior cruciate ligament in response to rotatory loads. J. Orthop. Res. 22, 85–9. doi:10.1016/S0736-0266(03)00133-5

Gage, B.E., McIlvain, N.M., Collins, C.L., Fields, S.K., Comstock, R.D., 2012. Epidemiology of 6.6 million knee injuries presenting to United States emergency departments from 1999 through 2008. Acad. Emerg. Med. 19, 378–85. doi:10.1111/j.1553-2712.2012.01315.x

Gopalakrishnan, A., Modenese, L., Phillips, A.T.M., 2014. A novel computational framework for deducing muscle synergies from experimental joint moments. Front. Comput. Neurosci. 8, 153. doi:10.3389/fncom.2014.00153

Grood, E.S., Suntay, W.J., 1983. A joint coor dinate system for the clinical description of the three-dimensional motions: application to the knee. J. Biomech. Eng. 105, 136–144.

Guess, T.M., Liu, H., Bhashyam, S., Thiagarajan, G., 2011. A multibody knee model with discrete cartilage prediction of tibio-femoral contact mechanics. Comput. Methods Biomech. Biomed. Engin. 16, 256–70. doi:10.1080/10255842.2011.617004

Guess, T.M., Thiagarajan, G., Kia, M., Mishra, M., 2010. A subject specific multibody model of the knee with menisci. Med. Eng. Phys. 32, 505–15. doi:10.1016/j.medengphy.2010.02.020

Harris, M.D., Cyr, A.J., Ali, A.A., Fitzpatrick, C.K., Rullkoetter, P.J., Maletsky, L.P., Shelburne, K.B., 2016. A Combined Experimental and Computational Approach to Subject-Specific Analysis of Knee Joint Laxity. J. Biomech. Eng. 138, 1–8. doi:10.1115/1.4033882

Huang, S., Schimmels, J.M., 1998. Achieving an Arbitrary Spatial Stiffness with Springs Connected in Parallel. J. Mech. Des. 120, 520–526.

Kanamori, A., Woo, S.L., Ma, C.B., Zeminski, J., Rudy, T.W., Li, G., Livesay, G. a, 2000. The forces in the anterior cruciate ligament and knee kinematics during a simulated pivot shift test: A human cadaveric study using robotic technology. Arthroscopy 16, 633–9. doi:10.1053/jars.2000.7682

Kia, M., Schafer, K., Lipman, J., Cross, M., Mayman, D., Pearle, A., Wickiewicz, T., Imhauser, C., 2016. A Multibody Knee Model Corroborates Subject-Specific Experimental Measurements of Low Ligament Forces and Kinematic Coupling During Passive Flexion. J. Biomech. Eng. 138, 51010. doi:10.1115/1.4032850

Kiapour, A., Kiapour, A.M., Kaul, V., Quatman, C.E., Wordeman, S.C., Hewett, T.E., Demetropoulos, C.K., Goel, V.K., 2014. Finite element model of the knee for investigation of injury mechanisms: development and validation. J. Biomech. Eng. 136, 11002. doi:10.1115/1.4025692

Kupper, J.C., Loitz-Ramage, B., Corr, D.T., Hart, D.A., Ronsky, J.L., 2007. Measuring knee joint laxity: A review of applicable models and the need for new approaches to minimize variability. Clin. Biomech. 22, 1–13. doi:10.1016/j.clinbiomech.2006.08.003

Lin, H.-C., Chang, C.-M., Hsu, H.-C., Lai, W.-H., Lu, T.-W., 2011. A new diagnostic approach using regional analysis of anterior knee laxity in patients with anterior cruciate ligament deficiency. Knee Surg. Sports Traumatol. Arthrosc. 19, 760–7. doi:10.1007/s00167-010-1354-3

Lorenz, A., Krickl, V., Ipach, I., Arlt, E.-M., Wülker, N., Leichtle, U.G., 2015. Practicability for robot-aided measurement of knee stability in-vivo. BMC Musculoskelet. Disord. 16, 373. doi:10.1186/s12891-015-0826-5

Moewis, P., Duda, G.N., Jung, T., Heller, M.O., Boeth, H., Kaptein, B., Taylor, W.R., 2016. The restoration of passive rotational tibio-femoral laxity after anterior cruciate ligament reconstruction. PLoS One 11, 1–14. doi:10.1371/journal.pone.0159600

Mommersteeg, T.J., Huiskes, R., Blankevoort, L., Kooloos, J.G., Kauer, J.M., 1997. An inverse dynamics modeling approach to determine the restraining function of human knee ligament bundles. J. Biomech. 30, 139–46.

Mootanah, R., Imhauser, C.W., Reisse, F., Carpanen, D., Walker, R.W., Koff, M.F., Lenhoff, M.W., Rozbruch, S.R., Fragomen, A.T., Dewan, Z., Kirane, Y.M., Cheah, K., Dowell, J.K., Hillstrom, H.J., 2014. Development and validation of a computational model of the knee joint for the evaluation of surgical treatments for osteoarthritis. Comput. Methods Biomech. Biomed. Engin. 17,

1502–17. doi:10.1080/10255842.2014.899588

Noyes, F.R., Grood, E.S., 1976. The strength of the anterior cruciate ligament in humans and Rhesus monkeys. J. Bone Joint Surg. Am. 58, 1074–82. doi:10.2106/JBJS.M.00187

Robinson, J.R., Bull, A.M.J., Thomas, R.R.D., Amis, A. a, 2006. The role of the medial collateral ligament and posteromedial capsule in controlling knee laxity. Am. J. Sports Med. 34, 1815–1823. doi:10.1177/0363546506289433

Shultz, S.J., Shimokochi, Y., Nguyen, A.-D., Schmitz, R.J., Beynnon, B.D., Perrin, D.H., 2007. Measurement of varus-valgus and internal-external rotational knee laxities in vivo--Part II: relationship with anterior-posterior and general joint laxity in males and females. J. Orthop. Res. 25, 989–96. doi:10.1002/jor.20398

Signorelli, C., Bonanzinga, T., Grassi, A., Lopomo, N., Zaffagnini, S., Marcacci, M., 2016. Predictive mathematical modeling of knee static laxity after ACL reconstruction: in vivo analysis. Comput. Methods Biomech. Biomed. Engin. 5842, 1–8. doi:10.1080/10255842.2016.1176152

Woo, S.L., Orlando, C. a, Gomez, M. a, Frank, C.B., Akeson, W.H., 1986. Tensile properties of the medial collateral ligament as a function of age. J. Orthop. Res. 4, 133–41. doi:10.1002/jor.1100040201

CHAPTER 6

Conclusions

6.1. Summary

This thesis aimed to develop an innovative approach to musculoskeletal modelling, with specific reference to the mechanical modelling of the tibiofemoral joint. This aim has been tackled by means of different steps, all aimed at clarifying and maximising the level of confidence needed for a meaningful use of MSMs within a clinical setting. The implemented steps and the corresponding outputs included a sensitivity analysis, an *ex vivo* and *in vivo* validation, and a novel procedure for model personalisation.

The sensitivity analysis has been performed to quantify how the main experimental error affecting the input data, i.e. the STA, affects the output pipeline of traditional MSMs combined with traditional MBO. The predictions at the hip and knee were generally less precise than those at the ankle. This information is extremely useful since it provides a unique reference framework for MSMs users concerning the limits of significance of the investigated output. This will allow the design of studies in line with the strengths and limitations of the available framework, allowing meaningful conclusions to be drawn on the population under analysis.

An innovative knee modelling approach has then been developed and validated using an *ex vivo* approach. A methodology to calibrate the proposed type of mechanical model of the knee based on a discrete set of compliance matrices was described. For validation purposes, the Lachman test was executed through a robotic system on a cadaveric knee joint. This resulted in accurate predictions in close proximity to the neutral pose, but the error increased non-linearly when significant deviations from the neutral pose occurred. The method proposed might open the way to a new generation of MSMs, embedding the load-dependent behaviour of each joint in a more biofidelic way. The newly developed knee model has been included in the

MSM pipeline to estimate joint angles using MBO through a penalty-based method. Results were validated using *in vivo* data in order to test the performance of the alternative joint definitions ("soft" constraints) against other traditional joint models ("hard" constrains) with true measurements available from a gold standard to quantify the accuracy. The results were promising for the implemented "soft" constraint, showing the need for adaptation for MSMs in defining more biofidelic joint models.

The development of a methodology for model personalisation has been the final focus of the current thesis. Results from an additional *ex vivo* testing campaign showed that it is possible to personalise the knee model based on a discrete set of compliance matrices. For this, force-displacement data from clinical tests was used, which did not require detailed subject anatomy usually acquired from medical images. This approach to personalisation has been evaluated using two different comparisons: a term-by-term matrix comparison and an assessment based on the Principal Axes Decomposition method. The described comparisons were evaluated in relation with the number and type of clinical tests available, providing an indication of differences for the analysed cases.

In conclusion, this thesis represents an important step toward a more confident use of MSMs in light of potential clinical applications. Indeed, the weakness of some aspects of traditional MSMs has been identified and a promising alternative in joint definition has been proposed, implemented and validated. Despite the fact that further developments are of course necessary, the feasibility of the novel compliance-based elastic joint model was proven and could also be applied to different articulations. Lastly, a new approach for model personalisation was developed, which in the future will only require force data recorded *in vivo* from instrumented knee laxity measuring tools.

6.2. Novelty of the work

This thesis showed novelty in several aspects of the work done.

For the sensitivity analysis, previous studies have proved that the MSM estimates were significantly affected by the STA in the input measurements (El Habachi et al., 2015; Myers et al., 2015). For the first time, however, this study implemented a realistic STA distribution, which was compared with independent literature (Akbarshahi et al., 2010; Cappozzo et al., 1996; Hara et al., 2014; Maslen and Ackland, 1994; Stagni et al., 2005; Tsai et al., 2009; Wrbaskić and Dowling, 2007), and whose effect on different publicly-available traditional MSMs was tested.

For the knee model development, the compliance (or stiffness) matrix, initially proposed by Loch et al., (1992) to describe the mechanics of the knee joint, was calculated for the first time in different conditions and configurations. The methodology, originally proposed by Stokes et al., (2002) for the spine, was adapted and described in detail to include data coming from robotic testing of a knee specimen as an input. For model implementation in MSM pipelines, despite a "soft" constraints approach has been proposed recently (Gasparutto et al., 2015), the work of the current thesis introduced the idea of an elastic joint model for the knee for the first time, based on the minimisation of the deformation energy.

For model personalisation, the idea of developing mechanical models of the knee personalised with subject specific force data has been proposed already in the last decade (Ewing et al., 2016; Guess et al., 2011, 2010; Harris et al., 2016; Kia et al., 2016; Mootanah et al., 2014). This thesis presents the novel contribution to expand this approach further by developing a personalised model not relying on detailed subject's anatomy. This new approach in conjunction with the accompanying methodology has been tested *ex vivo* but has the potential to be translated *in vivo* by the execution of laxity or clinical tests (Lorenz et al., 2015; Moewis et al., 2016). These tests can be seen as the link between the *ex vivo* and *in vivo* scenario.

6.3. *Future work*

A number of limitations, which have been listed in each chapter, affect the work of this thesis. Some of them will be the basis to undertake further research not conducted in this thesis. In particular, future studies could focus on one or more of the following aspects.

The STA design described in Chapter 3 might be used to identify suitable weight sets to be used within the inverse kinematics tools. This can be done by minimising the kinematics errors with respect to the baseline kinematics implemented. At the same time, alternative MBO approaches can be developed, embedding, for instance, a STA compensation as recently proposed (Clement et al., 2015; Richard et al., 2012). This could be possible by using the models and data made available from the publication associated to this part of the thesis (https://dx.doi.org/10.15131/shef.data.3502652). In addition, using similar statistical approaches of marker trajectories containing the STA might allow the development of a benchmark dataset for systematic testing of new and existing MBO functions.

The MBO algorithm presented in Chapter 4, including only one matrix for the computation, can be expanded, aiming to improve the accuracy of the estimated joint kinematics in different ways. An example could be to propose an angle-dependent approach, switching different matrices according to the different knee flexion extension angle predicted *in vivo*. This will allow better representation of the mechanical behaviour of the joint as measured *ex vivo* in different configurations (0°, 15°, 30°, 45°, 60°, 75° and 90°). A challenge related to this approach lies in the difficulties in defining ranges for which each matrix is valid as well as ensuring a smooth transition from one matrix to the next.

Once the knee model personalisation from clinical tests (Chapter 5) is extended to more specimens, it would be fascinating to implement the new approach within the MBO. This will produce subject specific joint kinematics based on force measurements. The assessment of accuracy and sensitivity of this new approach will be the following step. The accuracy can be tested in the same way as presented in the second part of Chapter 4. For the sensitivity, an intriguing approach could be to use

the same dataset containing a statistical distribution of STA (Chapter 3) and evaluate whether using the new approach will reduce knee kinematics variations or not.

Open challenges for clinical usability of MSMs include decreasing the costs of ACL surgery and rehabilitation by providing information about the most effective procedure for each patient, supporting the development of more effective surgical procedures, and establishing a standardised protocol of intervention. In this direction, future research lines are required to improve three main aspects, which happen to be closely linked, resulting in mutual benefits from one to the other. The first aspect is related to the input measurement technology, enabling the development of accurate, fast, and global bone tracking devices, less invasive than the ones currently available. The second refers to the joint models in MSMs. The traditional, simplified joint definition for the lower limb needs to be improved to account for force information in parallel with the personalisation advancements coming from medical images. This is necessary to simulate more complex and unconventional motions, which characterises the patient in a clinical setting. Lastly, the MBO is a flexible and versatile method, which is mostly used by imposing strict rules to estimate joint kinematics (i.e. “hard” constraints). The last aspect might limit the flexibility of the method in taking into account individual features such as those characterising pathological subjects. The use of soft constraints in MBO as introduced by this thesis has the potential to overcome this limitation in the future.

References

Akbarshahi, M., Schache, A.G., Fernandez, J.W., Baker, R., Banks, S., Pandy, M.G., 2010. Non-invasive assessment of soft-tissue artifact and its effect on knee joint kinematics during functional activity. J. Biomech. 43, 1292–301. doi:10.1016/j.jbiomech.2010.01.002

Cappozzo, A., Catani, F., Leardini, A., Benedetti, M.G., Della Croce, U., 1996. Position and orientation in space of bones during movement: Experimental artefacts. Clin. Biomech. 11, 90–100. doi:10.1016/0268-0033(95)00046-1

Clement, J., Dumas, R., Hageimester, N., De Guise, J. a., 2015. Soft tissue artefacts compensation in knee kinematics by multi-body optimization: performance of subject-specific knee joint models. J. Biomech. 48, 3796–3802. doi:10.1016/j.jbiomech.2015.09.040

El Habachi, A., Moissenet, F., Duprey, S., Cheze, L., Dumas, R., 2015. Global sensitivity analysis of the joint kinematics during gait to the parameters of a lower limb multi-body model. Med. Biol. Eng. Comput. 655–667. doi:10.1007/s11517-015-1269-8

Ewing, J.A., Kaufman, M.K., Hutter, E.E., Granger, J.F., Beal, M.D., Piazza, S.J., Siston, R.A., 2016. Estimating patient-specific soft-tissue properties in a TKA knee. J. Orthop. Res. 34, 435–443. doi:10.1002/jor.23032

Gasparutto, X., Sancisi, N., Jacquelin, E., Parenti-Castelli, V., Dumas, R., 2015. Validation of a multi-body optimization with knee kinematic models including ligament constraints. J. Biomech. 48, 1141–1146. doi:10.1016/j.jbiomech.2015.01.010

Guess, T.M., Liu, H., Bhashyam, S., Thiagarajan, G., 2011. A multibody knee model with discrete cartilage prediction of tibio-femoral contact mechanics. Comput. Methods Biomech. Biomed. Engin. 16, 256–70. doi:10.1080/10255842.2011.617004

Guess, T.M., Thiagarajan, G., Kia, M., Mishra, M., 2010. A subject specific multibody model of the knee with menisci. Med. Eng. Phys. 32, 505–15. doi:10.1016/j.medengphy.2010.02.020

Hara, R., Sangeux, M., Baker, R., McGinley, J., 2014. Quantification of pelvic soft tissue artifact in multiple static positions. Gait Posture 39, 712–717. doi:10.1016/j.gaitpost.2013.10.001

Harris, M.D., Cyr, A.J., Ali, A.A., Fitzpatrick, C.K., Rullkoetter, P.J., Maletsky, L.P., Shelburne, K.B., 2016. A Combined Experimental and Computational Approach to Subject-Specific Analysis of Knee Joint Laxity. J. Biomech. Eng. 138, 1–8. doi:10.1115/1.4033882

Kia, M., Schafer, K., Lipman, J., Cross, M., Mayman, D., Pearle, A., Wickiewicz, T., Imhauser, C., 2016. A Multibody Knee Model Corroborates Subject-Specific Experimental Measurements of Low Ligament Forces and Kinematic Coupling During Passive Flexion. J. Biomech. Eng. 138, 51010. doi:10.1115/1.4032850

Loch, D. a, Luo, Z.P., Lewis, J.L., Stewart, N.J., 1992. A theoretical model of the knee and ACL: theory and experimental verification. J. Biomech. 25, 81–90.

Lorenz, A., Krickl, V., Ipach, I., Arlt, E.-M., Wülker, N., Leichtle, U.G., 2015. Practicability for robot-aided measurement of knee stability in-vivo. BMC Musculoskelet. Disord. 16, 373. doi:10.1186/s12891-015-0826-5

Maslen, B. a., Ackland, T.R., 1994. Radiographic study of skin displacement errors in the foot and ankle during standing. Clin. Biomech. 9, 291–296. doi:10.1016/0268-0033(94)90041-8

Moewis, P., Duda, G.N., Jung, T., Heller, M.O., Boeth, H., Kaptein, B., Taylor, W.R., 2016. The restoration of passive rotational tibio-femoral laxity after anterior cruciate ligament reconstruction. PLoS One 11, 1–14. doi:10.1371/journal.pone.0159600

Mootanah, R., Imhauser, C.W., Reisse, F., Carpanen, D., Walker, R.W., Koff, M.F., Lenhoff, M.W., Rozbruch, S.R., Fragomen, A.T., Dewan, Z., Kirane, Y.M., Cheah, K., Dowell, J.K., Hillstrom, H.J., 2014. Development and validation of a computational model of the knee joint for the evaluation of surgical treatments for osteoarthritis. Comput. Methods Biomech. Biomed. Engin. 17, 1502–17. doi:10.1080/10255842.2014.899588

Myers, C. a., Shelburne, K.B., Laz, P.J., Davidson, B.S., 2015. A Probabilistic Approach to Quantify the Impact of Uncertainty Propagation in Musculoskeletal Simulations. Ann. Biomed. Eng. In Review, 1098–1111. doi:10.1007/s10439-014-1181-7

Richard, V., Camomilla, V., Cheze, L., Cappozzo, a., Dumas, R., 2012. Feasibility of incorporating a soft tissue artefact model in multi-body optimisation. Comput. Methods Biomech. Biomed. Engin. 15, 194–196. doi:10.1080/10255842.2012.713667

Stagni, R., Fantozzi, S., Cappello, A., Leardini, A., 2005. Quantification of soft tissue artefact in motion analysis by combining 3D fluoroscopy and stereophotogrammetry: A study on two subjects. Clin. Biomech. 20, 320–329. doi:10.1016/j.clinbiomech.2004.11.012

Stokes, I. a, Gardner-Morse, M., Churchill, D., Laible, J.P., 2002. Measurement of a spinal motion segment stiffness matrix. J. Biomech. 35, 517–21.

Tsai, T.-Y., Lu, T.-W., Kuo, M.-Y., Hsu, H.-C., 2009. Quantification of Three-Dimensional Movement of Skin Markers Relative To the Underlying Bones During Functional Activities. Biomed. Eng. Appl. Basis Commun. 21, 223–232. doi:10.4015/S1016237209001283

Wrbaskić, N., Dowling, J.J., 2007. An investigation into the deformable characteristics of the human foot using fluoroscopic imaging. Clin. Biomech. (Bristol, Avon) 22, 230–8. doi:10.1016/j.clinbiomech.2006.09.006